AD $Ac37481$

AMMRC CTR 76-41

ELECTROSLAG REMELTING

December 1976

Interim Technical Report by

D. R. Poirier, S. Kou, R. Furlong, and M.C. Flemings
Massachusetts Institute of Technology
Cambridge, Massachusetts 02139

Prepared for

ARMY MATERIALS AND MECHANICS RESEARCH CENTER
Watertown, Massachusetts 02172

AMMRC

ELECTROSLAG REMELTING

Interim Technical Report by

D. R. Poirier, S. Kou, R. Furlong, and M. C. Flemings

Massachusetts Institute of Technology
Cambridge, Massachusetts   02139

Prepared for

ARMY MATERIALS AND MECHANICS RESEARCH CENTER
Watertown, Massachusetts   02172

FOREWORD

This report was prepared by the Department of Materials Science and Engineering, Massachusetts Institute of Technology. The report is entitled, "Electroslag Remelting". The contract was administered under the technical supervision of R. H. Frost and F. C. Quigley of the Army Materials and Mechanics Research Center, Watertown, Massachusetts.

TABLE OF CONTENTS

ABSTRACT

This interim report describes research conducted at the Massachusetts Institute of Technology on macrosegregation in ingots produced by the electroslag remelting (ESR) process. The work has been on producing small experimental ingots in the laboratory, determining the severity of segregation in those ingots, and comparing the segregation with calculations using macrosegregation theory.

Two different types of experimental apparatus are described herein. The first, employed for Al-4%Cu, is a small scale ESR unit which consists of a DC power source, a water cooled mold, consumable electrodes, and slag layer as in conventional ESR processing. The second type of apparatus is one which simulates the solidification of an ESR ingot but does not employ slag. The unit, used for Sn-15%Pb, comprises a source of melt droplets, a cooled mold, and a heat source to simulate the heat input of the ESR process.

Results of macrosegregation in a series of five Al-4%Cu experimental ingots show that severe-localized segregates, as sometimes found in large commercial ingots, cannot be produced using this alloy cast in the small-scale ESR molds (7.6 cm in diameter). Surface to center compositional variations are produced enabling a comparison with calculations using macrosegregation theory.

In order to study a wider range of segregation problems encountered in ESR ingots, recent efforts are directed toward solidifying Pb-15%Sn alloy in the simulated ESR apparatus. Initial results obtained

are very encouraging. Severe macrosegregation is produced in this apparatus. In an ingot (8.2 cm diameter), the composition varies from about 26%Pb in the center to a minimum of 6%Pb slightly beyond midradius. Additionally, there are "freckles" at approximately midradius and an abnormally high fraction of eutectic constituent (similar to "V-segregates") in the center.

The analytical work is based upon an analysis of the slow creeping flow of liquid between dendrite arms. The flow is driven by (1) gravity induced convection, and (2) solidification shrinkage. Agreement between calculations of macrosegregation and the macrosegregation in the experimental ingots is excellent considering the large number of variables involved. The theory correctly predicts the presence of "freckles" found in the Sn-15%Pb ingot.

I. OVERVIEW OF RESEARCH CONDUCTED AND RESULTS OBTAINED

A. Background

The Casting and Solidification Research Group at the
Massachusetts Institute of Technology has studied solidification of steel
under Army sponsorship for about sixteen years.[1-12] Recent, and
current work is on the processing variables which affect the
solidification structure in ESR ingots. A recent report described work
on AISI 304 steel made in specially designed experimental ESR molds.
The effects of power input, current density, slag depth, and electrode
diameter on electrode melting rate, temperature gradient in the liquid,
and isotherm velocities were studied and related to microstructure. One
innovation resulting from that work is that by electrode and slag cooling
the investigators were able to achieve increased ratios of thermal
gradient to solidification rate (G/R). The resulting dendritic
structures were much finer than those observed in exothermic molds at
comparable distances from the bottom chill.[12]

Work reported herein is on the heat and fluid flow variables which
influence macrosegregation in ESR ingots. Some types of
macrosegregation, including "freckles" and surface to center variations
in composition, result from causes that can be described quantitatively.
The M.I.T. solidification research group has carried out numerous
analytical and experimental studies on macrosegregation.[13-19] This
interim report describes work which applies the principles of

macrosegregation theory to the solidification of ESR ingots. A computer

analysis is developed for the special geometry and heat flow conditions

found in experimental ingots, and results of the analysis are compared

with the experimental work on model alloys, Al-4%Cu and Sn-15%Pb.

B. Experimental Work

Two different types of experimental apparatus were employed in

this work. The first is a small ESR unit comprised of a DC power source,

a water cooled mold, a consumable electrode and a slag layer as in

conventional ESR, Figure 1. This unit was used for experimental work on

Al-4% copper alloy.

The second apparatus employed is one which simulates solidification

behavior of the ESR process but does so without a consumable electrode or

slag. This unit comprises a source of molten metal droplets, a cooled

mold, and a heat source to simulate ESR heat input, Figure 2. This unit

was used for experimental work on a Sn-15%Pb alloy.

In both of the apparati, liquidus and solidus shape and movement

could be varied significantly and could be made to closely simulate the

behavior of actual ESR ingots. For example, Figures 3 and 4 show the

shapes of isotherms during solidification of ingots (one of Al-4% Cu and

one of Sn-15% Pb). In both of these ingots, significant segregation was

found. Figure 5 shows the segregation in the Al-Cu ingot and Figure 6

the segregation in the Sn-15% Pb ingot. The segregation in the Sn-15% Pb

ingot was significantly severe that gross segregates, commonly called

"freckles", formed, as shown in Figure 7.

C. <u>Analytical Work</u>

An underlying concept of this work is that macrosegregation, such as that shown in Figures 5 - 7, can be understood and quantitatively analyzed using theories developed at M.I.T. over the last decade.[13-19] The cause of the segregation is believed to be the slow creeping flow of liquid between dendrite arms; that flow is driven primarily by (1) gravity induced convection, and (2) solidification shrinkage.

Basic mathematics describing this flow was developed earlier and is summarized herein. In this work, the basic equations are applied to the ESR process and a computer analysis developed to solve for the fluid flow and resulting segregation behavior in ESR ingots. As examples of the computer output, Figures 8 and 9 show the calculated interdendritic fluid flow in the two ingots referred to earlier. With flow curves such as those of Figures 8 and 9, calculations of macrosegregation are readily made. Figure 10a compares the experimental results of the Al-4%Cu ingot with theory, and Figure 10b compares the results of the Sn-15%Pb with theory. Agreement is excellent considering the large number of variables in the complex segregation process. Detailed discussion is given in the report of this comparison between experiment and theory, as well as of the choice of the adjustable parameter, the "permeability", of the mushy zone.

In addition to the comparison of theory with experiment described above, it should be noted that the macrosegregation theory predicts when "freckles" such as those shown in Figure 7 appear, and this theory correctly predicts the presence of the freckles in that ingot.
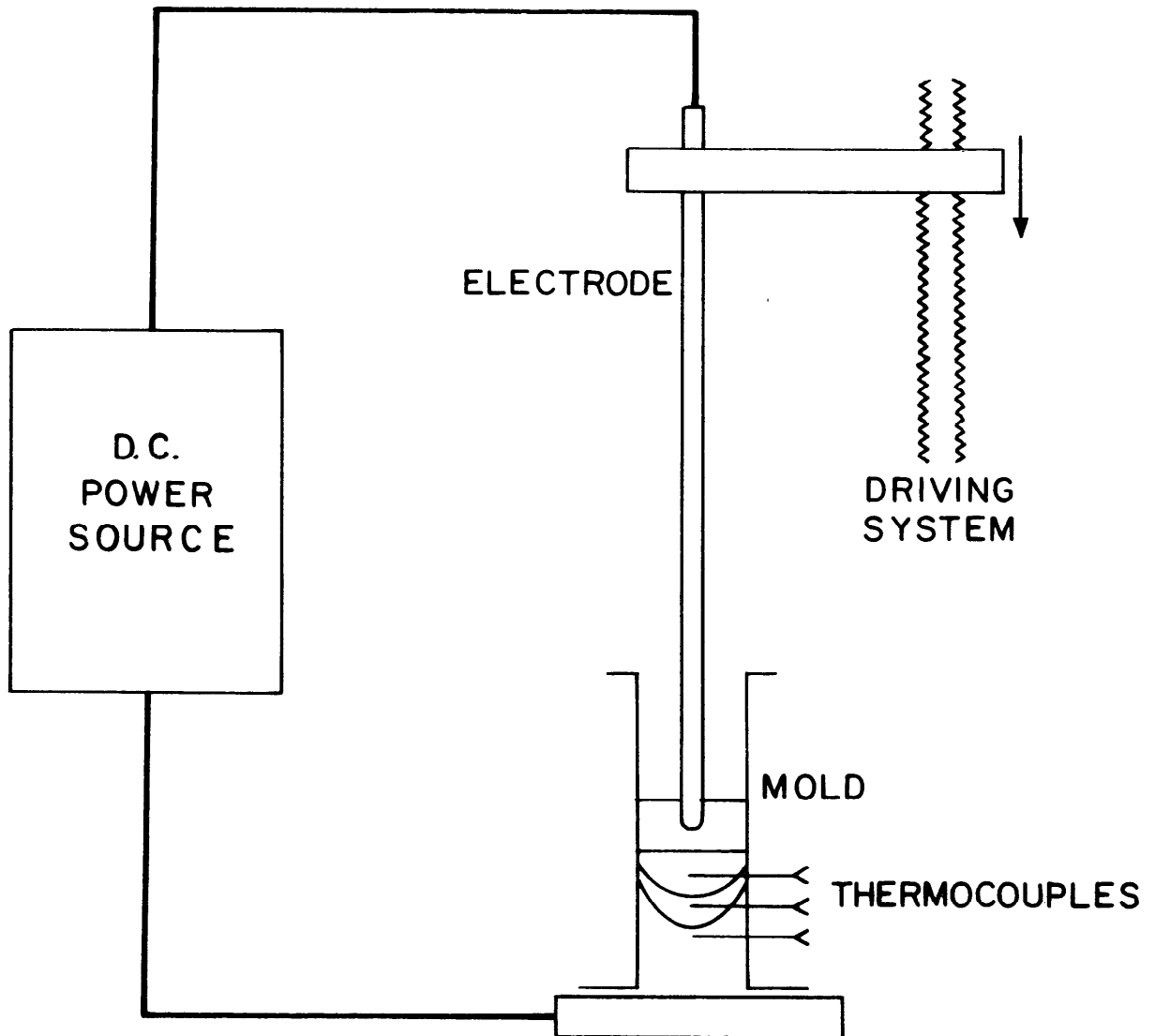
Figure 1: Schematic of the experimental set-up used to study macrosegregation in Al-4% Cu ESR ingots.
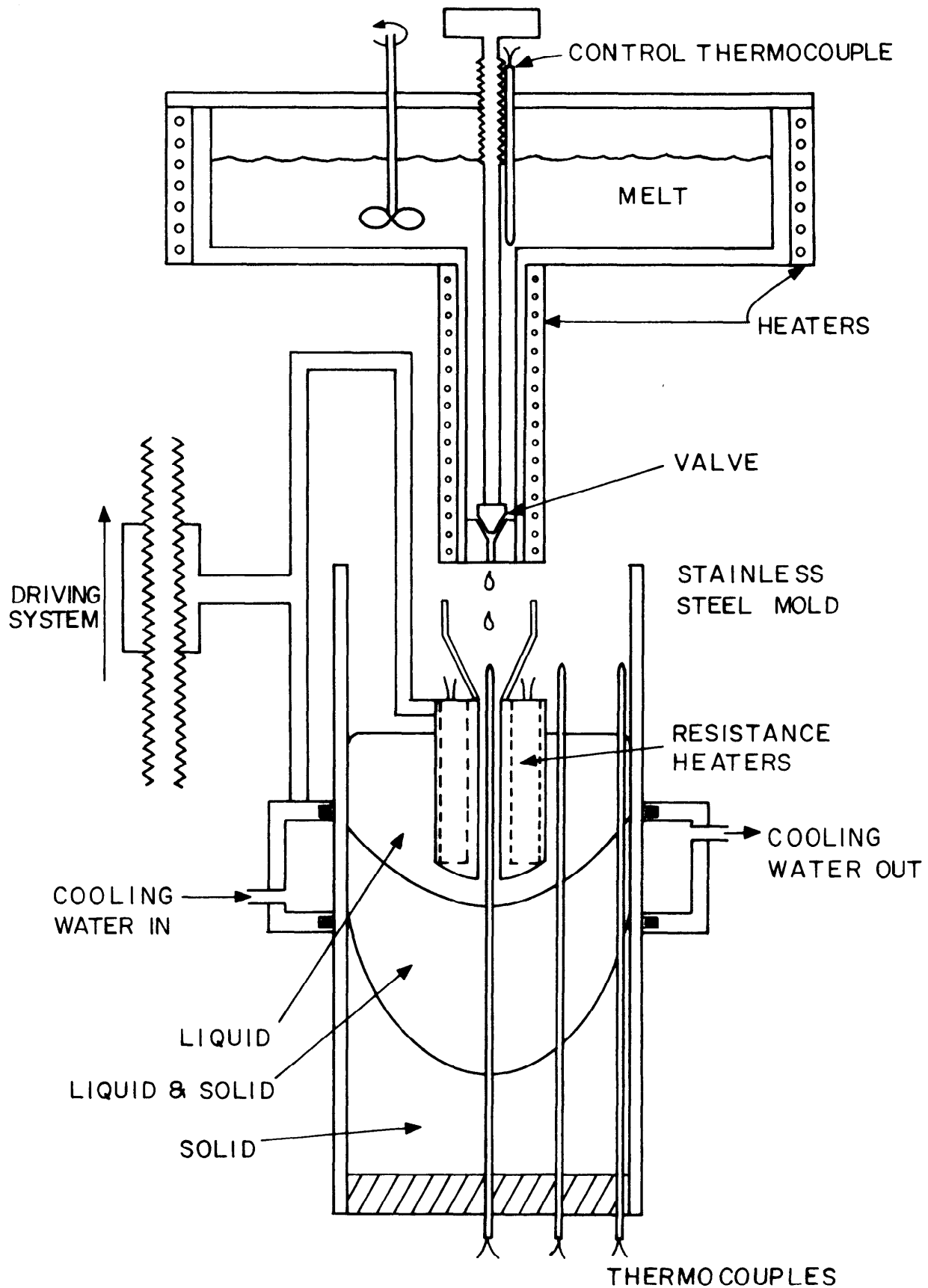
Figure 2: Apparatus used as an analog ESR process to produce Sn-15% Pb ingots.
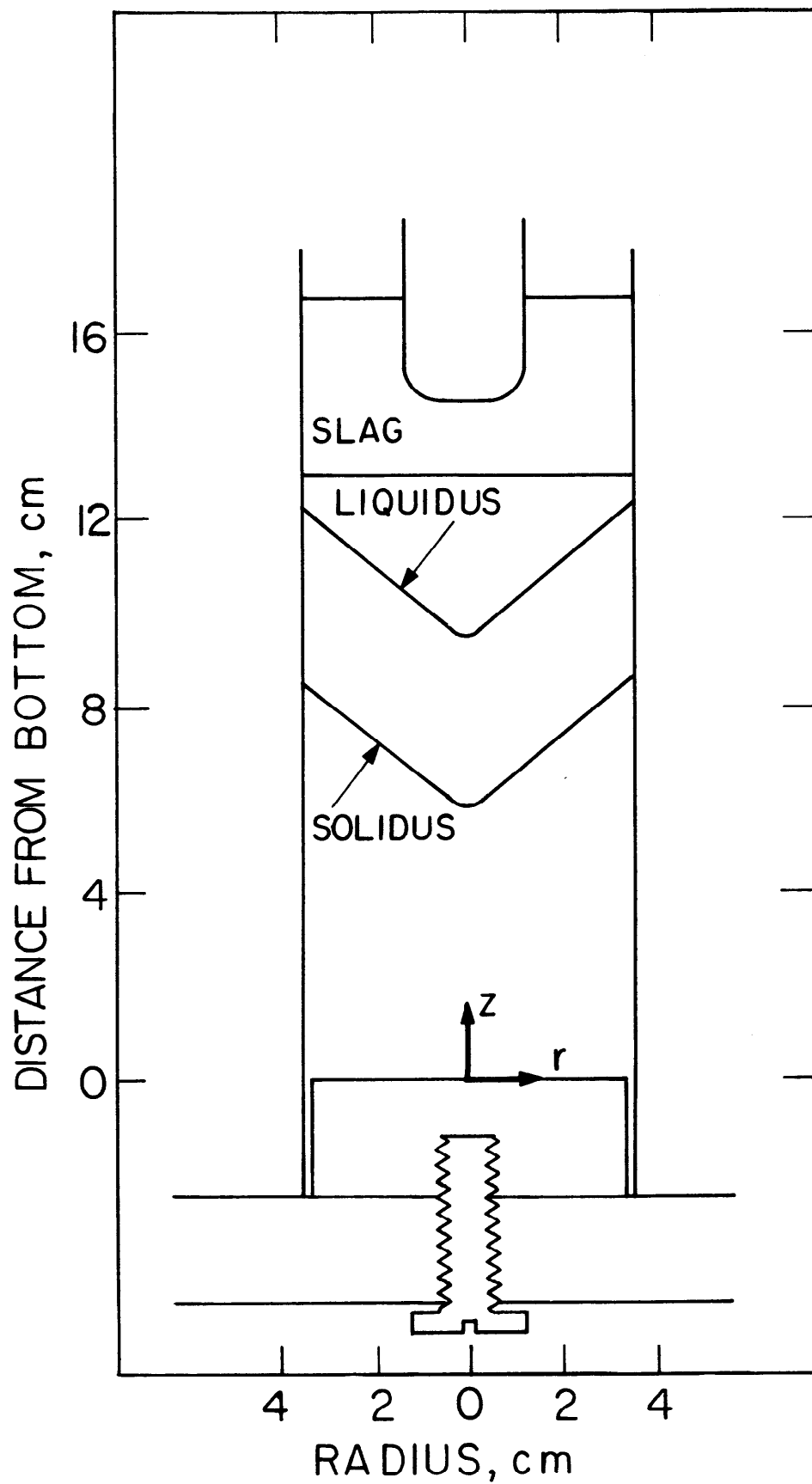
Figure 3: The position of liquidus and solidus isotherms after 7 minutes in ingot 1 (Al-4% Cu).
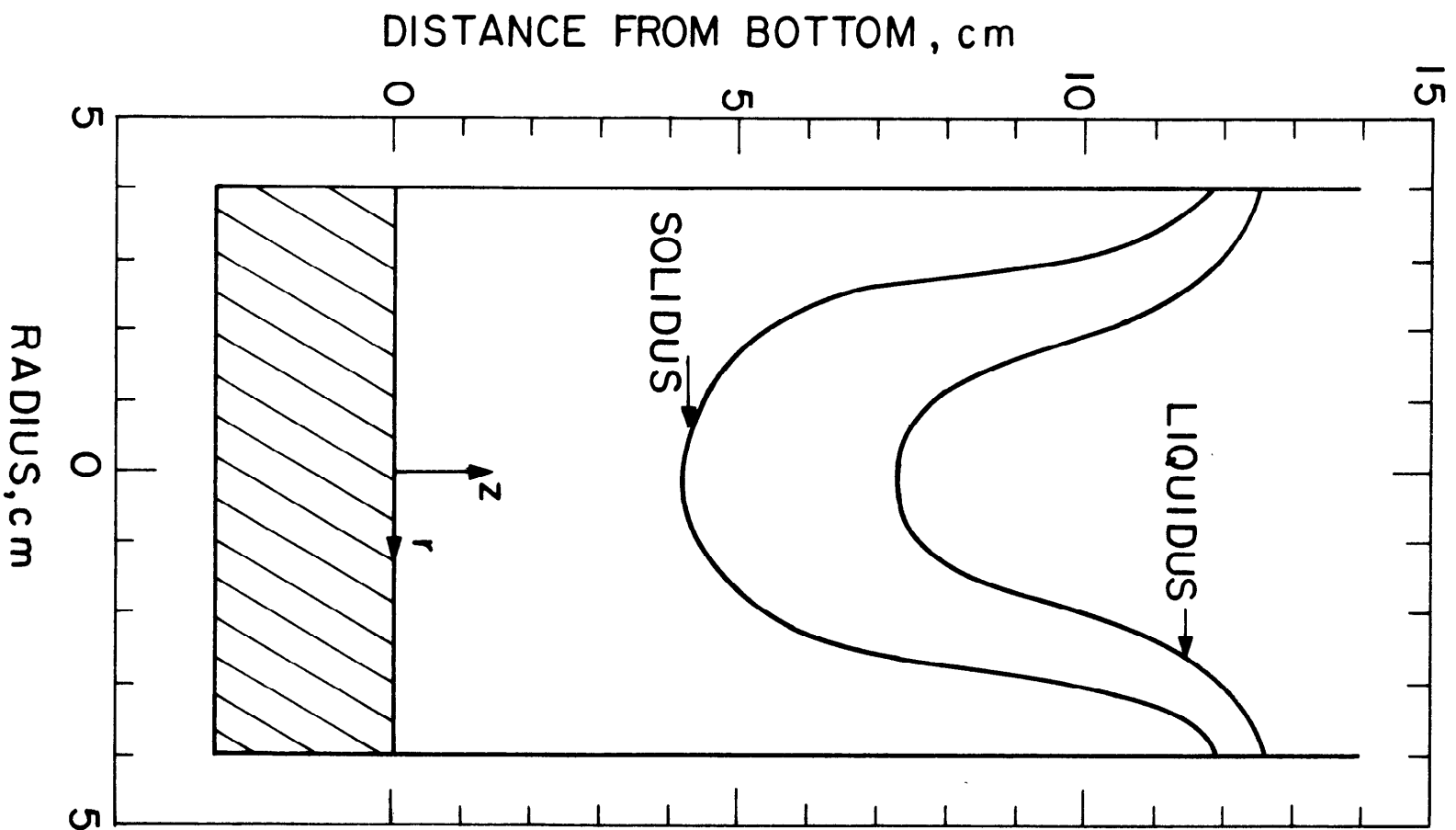
Figure 4: The shape of the mushy zone in the Sn-15% Pb ingot after 14 minutes.
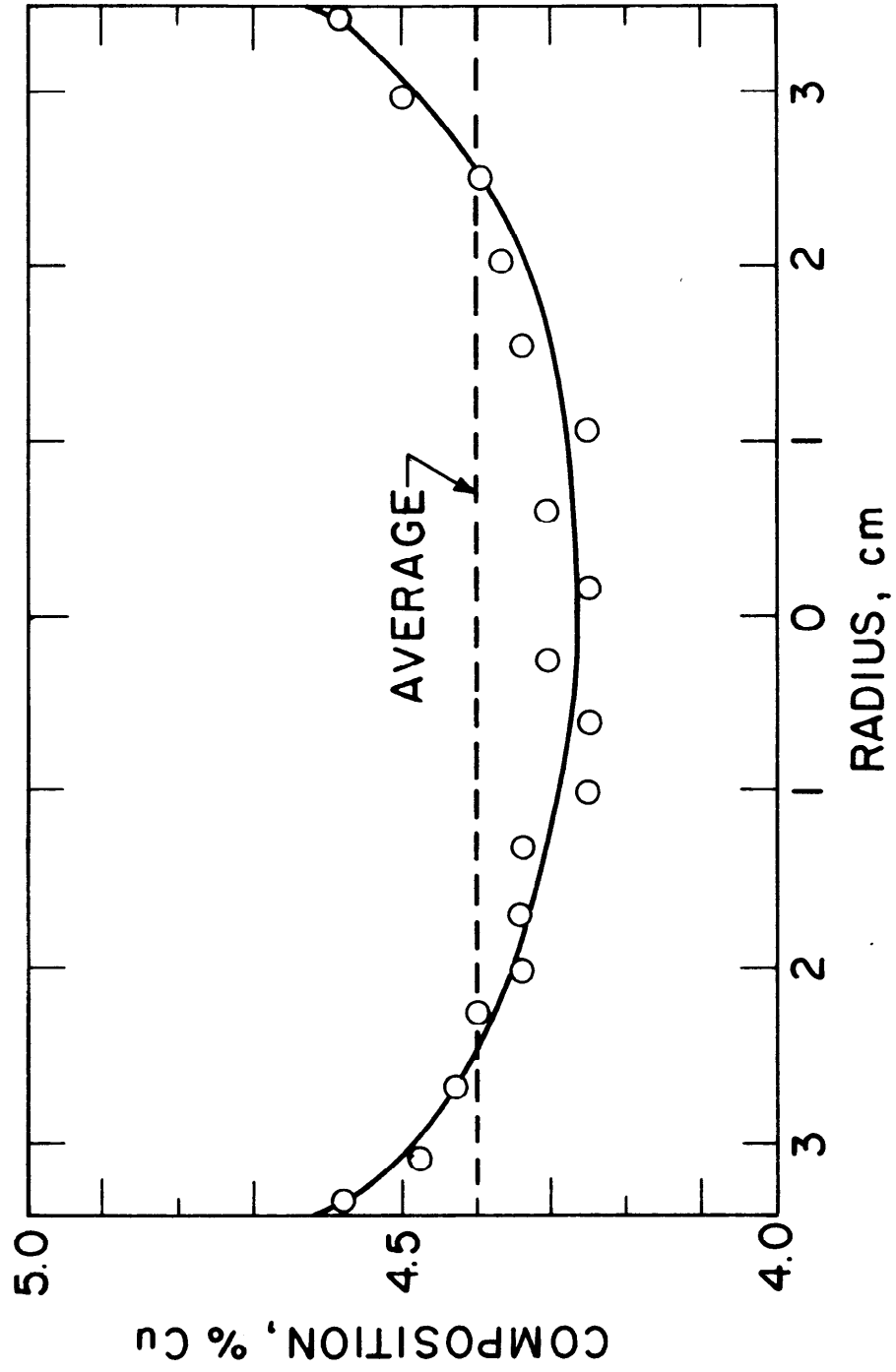
Figure 5: The macrosegregation pattern in ingot 1 (Al-4.4% Cu) determined by x-ray fluorescence.
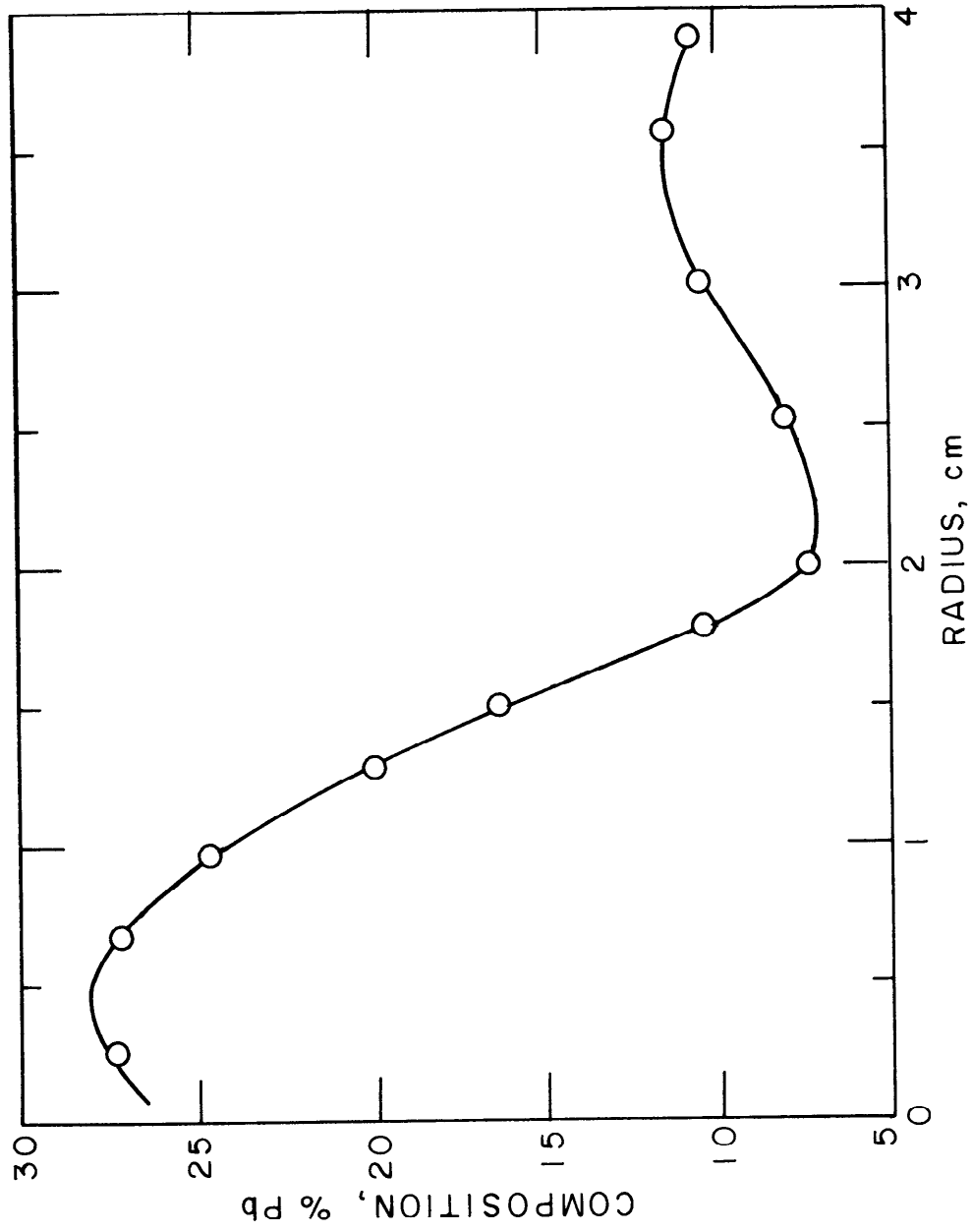
Figure 6. Severe segregation in the Sn-15% Pb ingot.
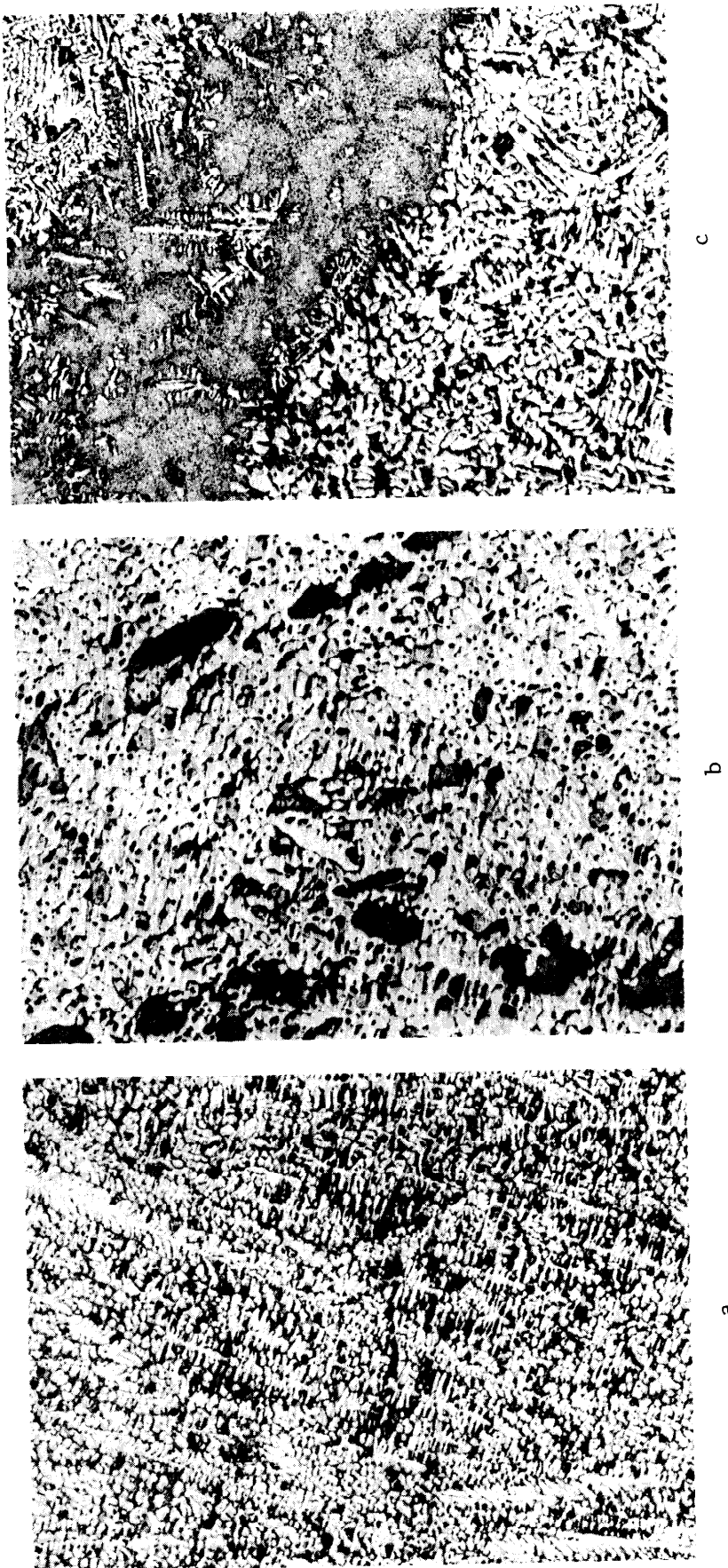
Figure 7: Structure of the Sn-15% Pb ingot: (a) near surface; (b) midradius; (c) center. Magnification, 25.6X.
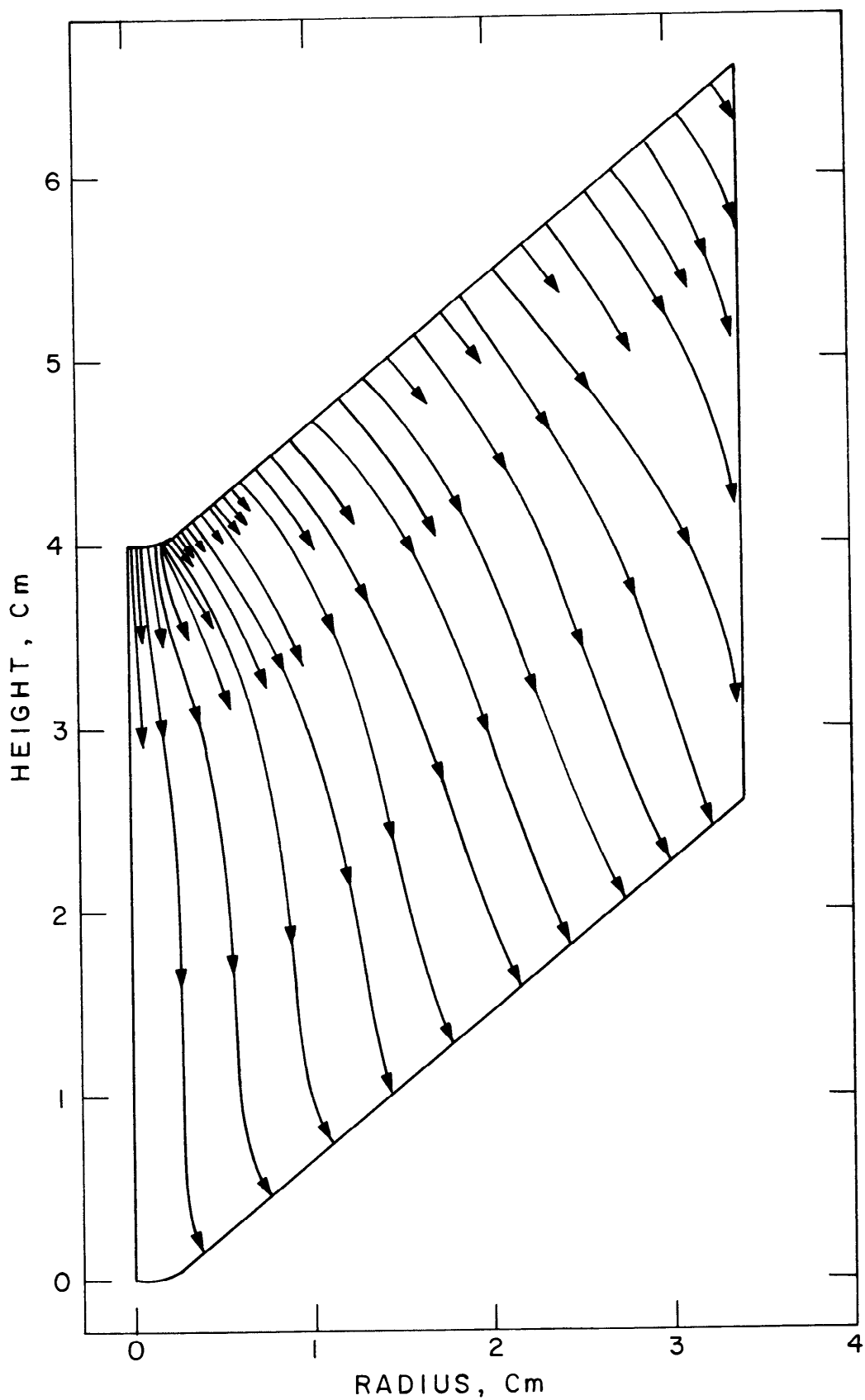
Figure 8: Flow lines in ingot 1 (Al-4.4% Cu) determined using $\gamma = 8 \times 10^{-8}$ cm^2. The spacing of the flow lines is approximately proportional to the inverse of the velocity magnitude.
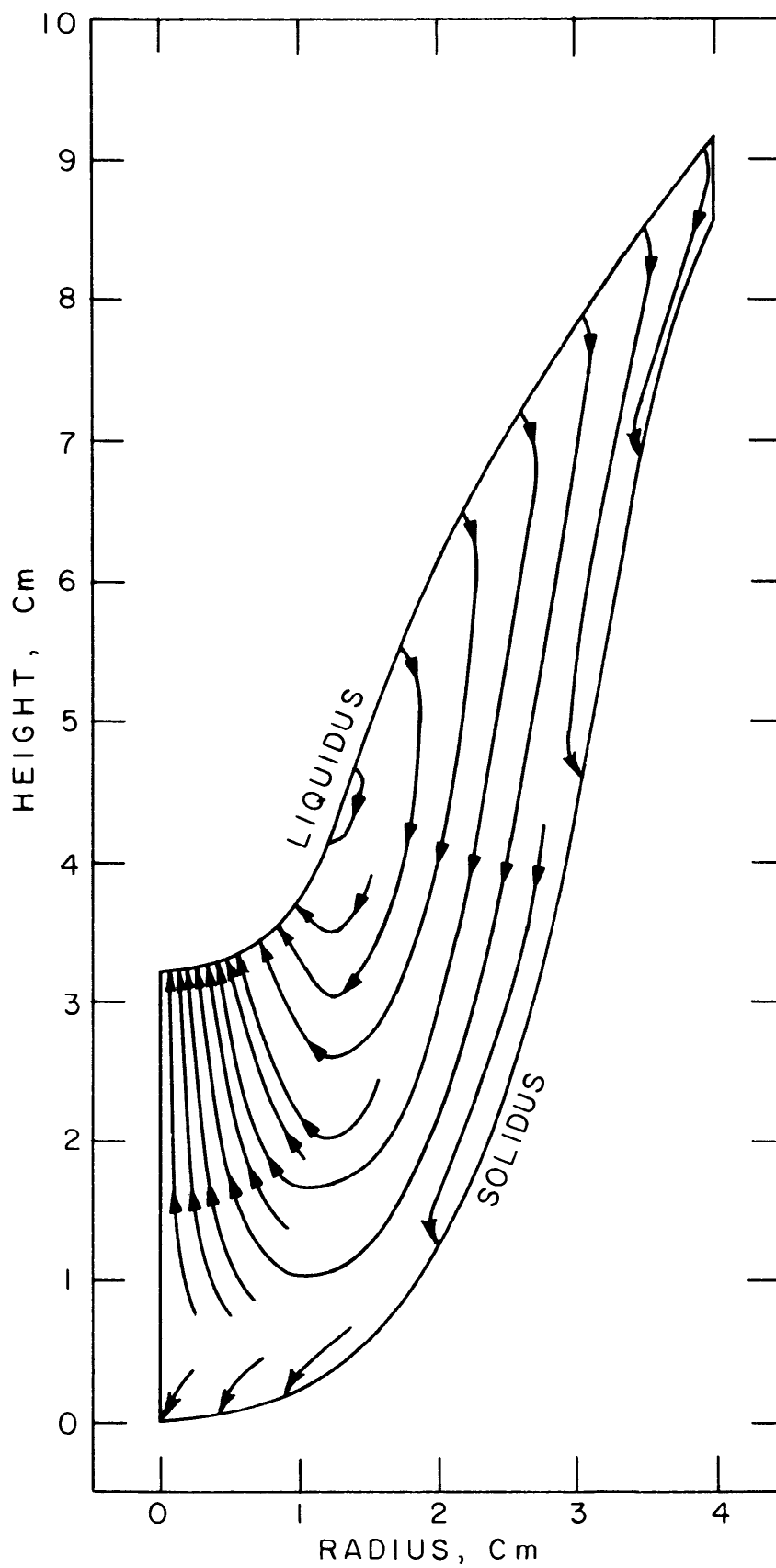
Figure 9:   Flow lines in the Sn–15% Pb ingot calculated using
$\gamma = 10^{-6}$ cm^2.   Spacings are approximately equal to the
inverse of the relative magnitude of velocity.
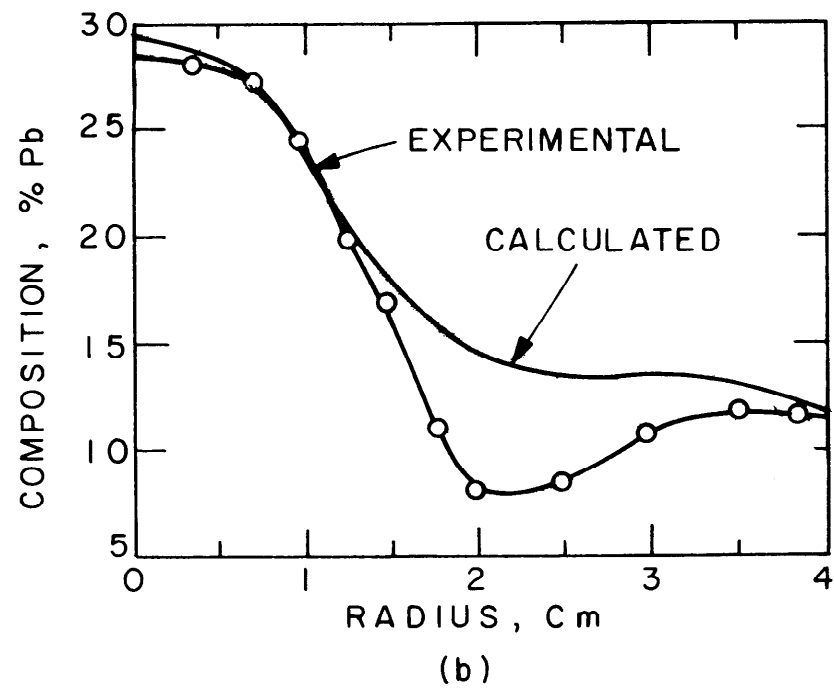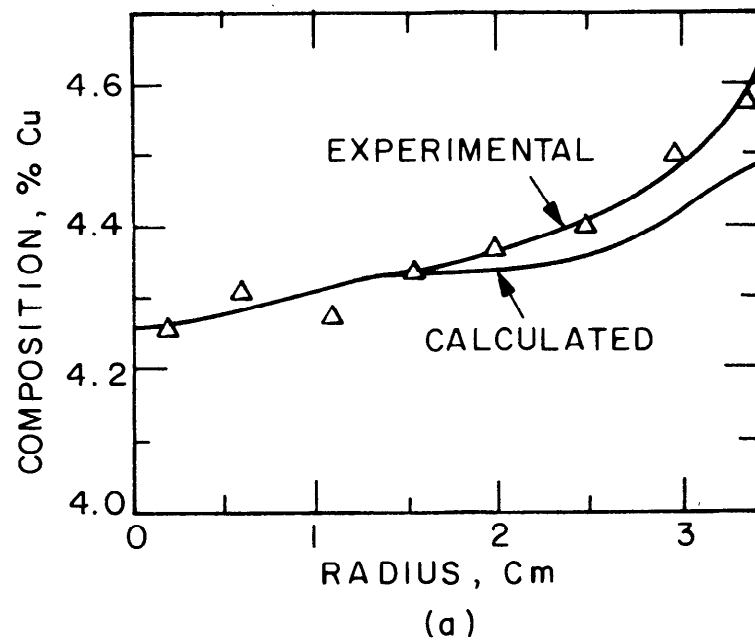
Figure 10: Comparison macrosegregation determined by experiment and by calculation. (a) Al-4.4% Cu ingot; (b) Sn-15% Pb ingot.

II. INTRODUCTION

A. Related Research

The ESR process is one of the most important new processes developed for special purpose alloys. The main advantages are the refining that can be obtained by melting through a slag of controlled composition, and the special control over solidification. Such control reduces dendrite arm spacing, microsegregation, and porosity, hence leading to a sound ingot.[20]

However, the recent production of ESR ingots for large forgings has shown that serious macrosegregation problems including centerline segregation and channel-type segregation (freckles) can result.[21] The non-uniformity of properties and structure can deleteriously affect the mechanical behavior of ingots during forging or rolling. The development of the continuous ESR process is also limited by the same macrosegregation problem.[22]

Like other solidification processes, the shape and depth of the "mushy" zone play an important role in the macrosegregation found in ESR ingots. It has been found that the operating conditions that favor a deeper shape of mushy zone will cause more macrosegregation in the ESR ingots.[23] The reason for this, according to the macrosegregation theory[17,24], is that solute-rich interdendritic fluid flow can be strongly affected by solidification shrinkage and gravity in a deep mushy zone.

Experimental and computer studies[10,25,26] have shown that the melting rate of the electrode is the most important parameter in determining the depth of liquid metal. A higher melting rate results in a deeper metal pool and hence a deeper mushy zone. Other operating parameters such as composition and amount of slag, thermal conductivity of metal, current and voltage, electrode polarity also affect the depth of liquid pool and mushy zone. The computer has also been used to investigate heat flow and gap formation in order to predict conditions which lead to break-outs in continuous casting.[50]

Heat flow models have been developed to relate the shape of mushy zone to the operating parameters mentioned above.[26-29] Up to now, the only quantitative study on macrosegregation in ESR ingots was carried out by Mitchell.[30] However, his approach was not rigorous since no macrosegregation theory was considered. Recently, Thomas et al[31] applied a magnetic field shield to solidifying ESR ingots and reduced macrosegregation. Cooper[21] reported on the so-called "central zone remelting technique" by trepanning and remelting the badly segregated central zone of a conventionally cast big ingot. This technique, however, provides no direct prevention of macrosegregation formation in the final core solidified as an ESR ingot.

As the solidification research group at M.I.T. worked on macrosegregation[13-19], other researchers reported on the importance of convection in the mushy zone during the solidification of castings and ingots.[24,32-34] In particular, Copley et al[34] have pointed out

how "density inversions" can lead to the formation of "freckles" in nickel-base superalloys.

One difficulty, in studying the solidification of ESR ingots, is obtaining thermal data. Mellberg and Sandberg[35] demonstrate that by measuring secondary dendrite arm spacing and "doping" to obtain the shape of the liquidus isotherm, it is possible to deduce temperature distribution, cooling rates, and thermal gradients within the mushy zone. Very recently Frost[36] has applied similar technique and analyses to describe the solidification of a series of AISI 4340 ESR ingots produced at different melt rates.

B. Permeability

In order to calculate extent of macrosegregation in ESR ingots, it is necessary to analyze the velocity of interdendritic liquid in the mushy zone. D'Arcy's law is used to describe flow through porous media; it is

$$\vec{v} \ = \ - \frac{K}{\mu g_L} \ (\nabla P + \rho_L \vec{g}) \tag{1}$$

where $\vec{v}$ is the interdendritic liquid velocity, μ is the viscosity, g_L is the volume fraction liquid, P is pressure, ρ_L is the liquid density, $\vec{g}$ is the acceleration constant, and K is the specific permeability or simply permeability. Permeability, as defined in Equation (1), has dimensions of length squared.

Physically, the permeability can be pictured in two ways, both
leading to the same result, but arrived at by slightly different
physical models. In one case, interdendritic flow is pictured as taking
place in long tortuous channels through the porous solid, and to account
for the fact that the channels are neither straight nor smooth, a
"tortuosity factor", τ, is applied. This model is referred to by
Mehrabian et al[18]; with this model the permeability, K, is

$$K = \frac{g_L^2}{8\pi n\tau^3} \qquad (2)$$

where n is the number of flow channels per unit area normal to flow, and
τ is the tortuosity factor. For a given dendrite arm spacing, if n and
τ are constants, the permeability is related to volume fraction liquid
by

$$K = \gamma g_L^2 \qquad (3)$$

where

$$\gamma = (8\pi n\tau^3)^{-1} \quad .$$

Piwonka and Flemings[37] report values of permeability measured in
Al-4% Cu alloy which obey Equation (3) for weight fraction liquid up to
about 0.35 with $\gamma \simeq 6 \times 10^{-9}$ cm^2. Using a somewhat different
experimental technique, Apelian et al[38] measured permeability in
porous dendritic networks of Al-4% Si alloys, and also observed that
Equation (3) is valid for volume fraction liquid up to 0.37 with
$\gamma \simeq 9 \times 10^{-9}$ cm^2 and $\gamma \simeq 3 \times 10^{-9}$ cm^2 for nongrain-refined and

grain-refined structures, respectively. In these works[37,38] permeability was not rigorously determined as a function of dendrite arm spacing. Apelian et al report approximate secondary dendrite arm spacings of 280 microns (nongrain-refined) and 150 microns (grain-refined) measured on two samples only. Piwonka and Flemings do not report dendrite arm spacings, but it appears that the secondary dendrite arm spacing is about 140 microns. The results of these measurements of permeability in aluminum alloys are shown in Figure 11. For $g_L > 0.35$, the work of Piwonka and Flemings show that the slope changes to a value much greater than 2 so that γ in Equation (3) is not constant. This can be interpreted to indicate that the number of channels available for flow (n) or tortuosity (τ) or both are not constant when $g_L > 0.35$. Also, one would expect in the range where γ is constant that permeability increase with increasing dendrite arm spacing. Figure 11 indicates that this is not necessarily the case, although, as mentioned, the secondary arm spacings are not systematically recorded in these studies.

A similar model for permeability is to imagine flow through channels which are neither straight nor smooth with areas normal to flow which are highly irregular. In this case the channels are characterized by their "hydraulic radius", R_H, which is shown to be[39]

$$R_H = g_L / S \tag{4}$$

where S is the surface area of the solid phase per unit volume of alloy

(i.e., per unit volume of "mush"). In this case,

$$K = \frac{g_L^3}{aS^2} \tag{5}$$

and a is constant in the range of 4.2 - 5. Equation (5) has the advantage that in order to calculate permeability, only one paramater of the structure, S, needs to be characterized whereas Equation (2) requires knowledge of n and τ.

Both expressions, Equations (2) and (5), can be used to predict, qualitatively, the effect of cooling rate during solidification on permeability. In ingots with high cooling rates, dendrite arms are more closely spaced than in ingots slowly cooled. Since n, in Equation (2), increases with decreasing dendritic spacings, then permeability should be less as ingot cooling rate increases. Also, the surface area of the dendritic phase, S, would increase with decreasing dendritic spacing, and Equation (5) likewise predicts that K should decrease.

Streat and Weinberg[40] measured permeability in partially solidified Pb-20% Sn at 193°C. In their experiments volume fraction liquid was held constant ($g_L = 0.19$), and dendrite arm spacing was varied. Using average primary arm spacings ($\bar{\lambda}$), and assuming that

$$n = (\bar{\lambda})^{-2} \tag{6}$$

they tested measured values of K against Equation (2). As predicted by Equations (2) and (6), permeability varies directly with $\bar{\lambda}^2$ and the

tortuosity factor is 4.6.

Permeability also varied, qualitatively, as expected with secondary arm spacing, but no simple relationship such as Equation (6) could be readily applied, so primary spacings were considered as the more useful parameter for characterizing the structure.[40] However, one could argue that since secondary arm spacing relates solely to cooling rate during solidification, it is better to characterize structures by secondary arm spacings even though a simple relationship between permeability and secondary arm spacing apparently does not exist. The results of Streat and Weinberg[40] are given in Figure 12 in terms of secondary arm spacings. For the largest spacing (83 microns) examined, permeability is about 7×10^{-9} cm^2; extrapolating results to arm spacings of 140 microns, permeability is about $10^{-8} - 10^{-7}$ cm^2. At fraction liquid 0.19, permeability in aluminum alloys is about 10^{-10} cm^2 (Figure 11). It appears, therefore, that the permeability (at a given secondary arm spacing) is one or two orders of magnitude greater in Pb-Sn alloys than in aluminum alloys.

To sum up, studies to date show that permeability increases with increasing fraction liquid and with increasing dendrite arm spacings but, as yet, there is no one relationship which takes into account both of these factors quantitatively. Because of these uncertainties in computing permeabilities, calculations done on ingots, reported herein, use permeability as given by Equation (3).
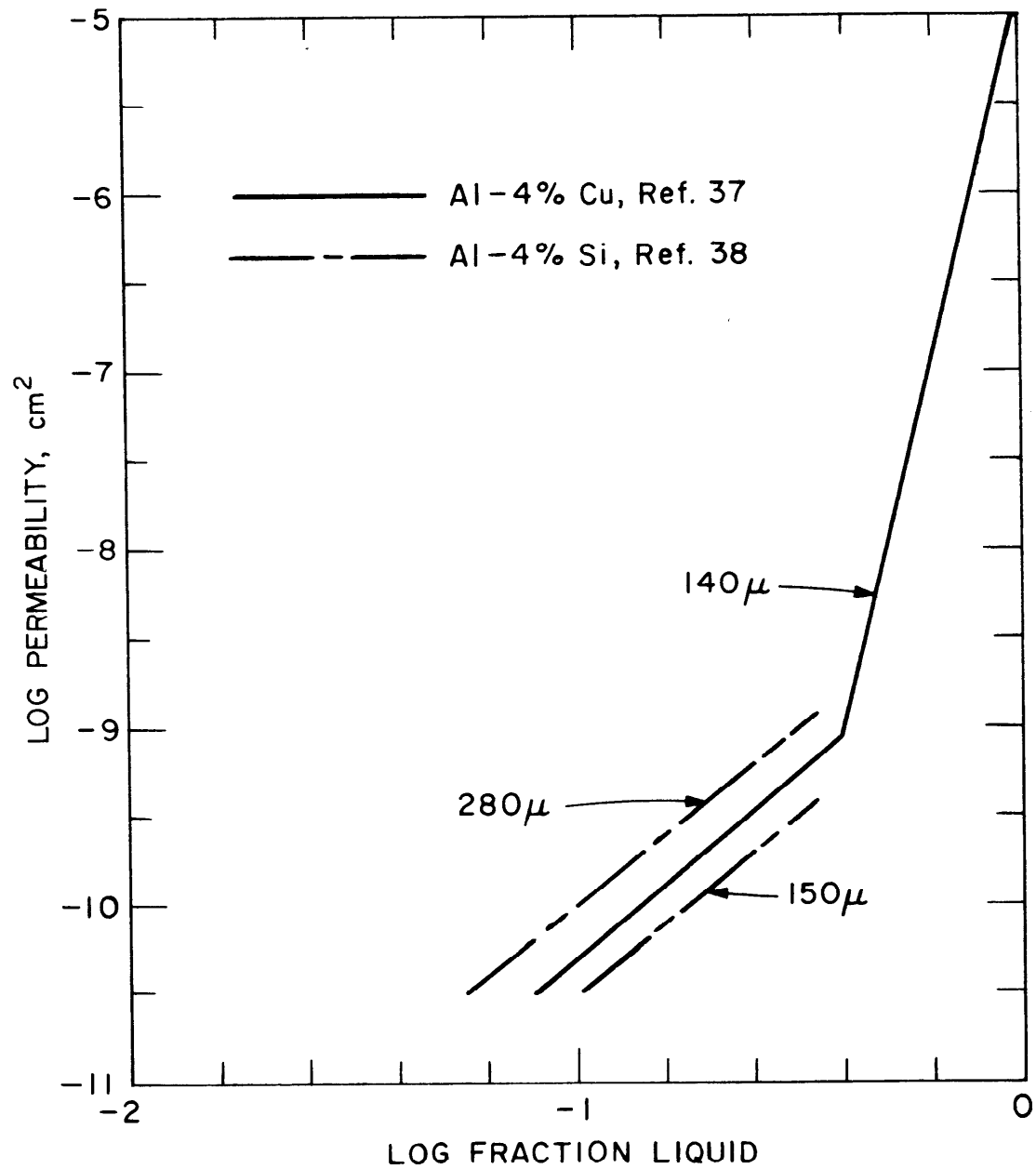
Figure 11: Permeability of aluminum alloys. Numbers on
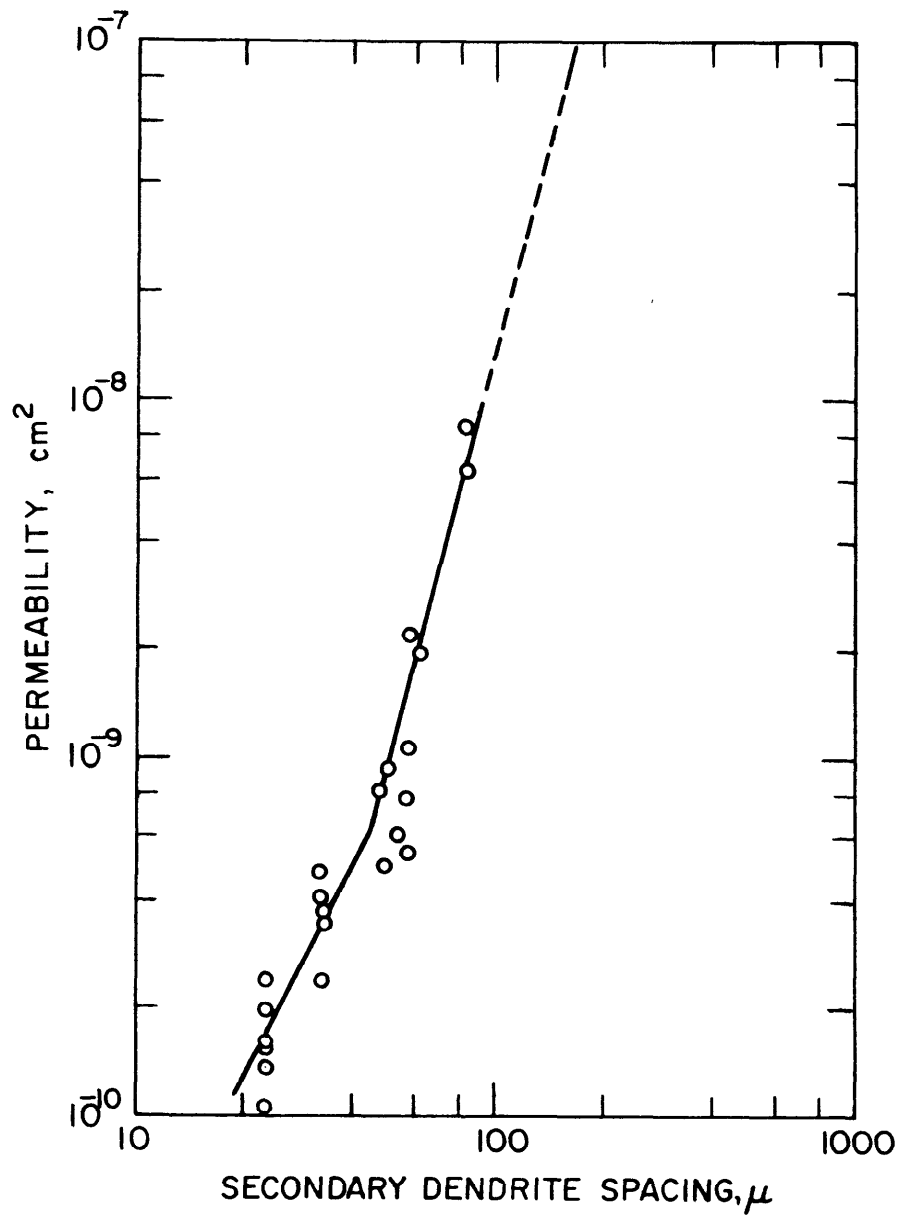curves are approximate secondary arm spacings.

Figure 12:   Permeability of Pb-20% Sn alloy.   Experimental
data of Streat and Weinberg[40] ; broken line is
used for extrapolation.

III. ANALYSIS OF MACROSEGREGATION

A. Theoretical Model

The interdendritic liquid within the mushy zone is acted upon by gravity; consequently if the density of that liquid varies during solidification, there is convection. We refer to this as "gravity-induced" convection. Convection of interdendritic liquid also occurs due to solidification shrinkage since liquid "feed metal" must flow towards regions within the mushy zone where the solidifying solid has a density greater than the local interdendritic liquid. This contribution to the convection is called the "solidification induced" convection. The combined effect of the "gravity induced" and the "solidification induced" convection gives the total convective pattern within the mushy zone of a solidifying ingot. If solidification time is long (as in a large steel ingot), "gravity induced" convection predominates because the dendrites in the solid-liquid region are coarse and open so that solute-rich interdendritic liquid flows with little resistance offered by the solid phase. Rather extensive flow also results because the time available for flow during solidification is large. In a "chill" casting, dendrites are fine and solidification time is small; hence, the amount of flow is considerably less than in large ingots and is primarily "solidification induced".

To describe the convection of interdendritic liquid within the mushy zone, D'Arcy's Law is used, so that Equation (1) applies.

The interdendritic liquid velocity $\vec{v}$ must satisfy continuity within the mushy zone which means that at all times

$$g_s + g_L = 1 \tag{7}$$

and

$$\frac{\partial}{\partial t}(\rho_s g_s + \rho_L g_L) = -\nabla \cdot \rho_L g_L \vec{v} \tag{8}$$

where g_s is volume fraction of the solid. Equation (8) is the continuity equation which is written for two phases, solid and liquid, with the assumption that the solid phase is stationary.

Volume fraction liquid varies according to the alloy under consideration and the manner in which solute partitions between the solid and liquid phases during solidification, the thermal gradient ∇T and cooling rate ε, and the amount of convection within the mushy zone. The expression which takes all of these factors into account has been derived by Flemings and Nereo[13] and is called the "local solute redistribution equation". It is

$$\frac{\partial g_L}{\partial C_L} = -\left(\frac{1-\beta}{1-k}\right)\left(1 + \frac{\vec{v}\cdot\nabla T}{\varepsilon}\right)\frac{g_L}{C_L} \tag{9}$$

where k is the equilibrium partition ratio, β is the solidification shrinkage defined as $(\rho_s - \rho_L)/\rho_s$ and C_L is the composition of the interdendritic liquid.

Equations (1) and (7 - 9) are combined to give an expression for the pressure distribution within the mushy zone. In cylindrical

coordinates (r,z), and with the mushy zone moving at a constant velocity, the pressure is described by

$$\frac{\partial^2 P}{\partial r^2} + A \frac{\partial P}{\partial r} + \frac{\partial^2 P}{\partial z^2} + B \frac{\partial P}{\partial z} + C = 0 \quad . \tag{10}$$

The method of arriving at Equation (10) is given in Appendix A where the coefficients A, B, and C, are also defined. Equation (10), along with the following boundary conditions, constitute the pressure distribution within the mushy zone.

By symmetry, there is no radial component of velocity at the centerline so the pressure gradient in the r-direction is zero; therefore

$$\frac{\partial P}{\partial r} (z,0) = 0 \quad . \tag{11}$$

Also, by virtue of the mold wall there is no radial velocity component at the ingot wall (r=R); so

$$\frac{\partial P}{\partial r} (z,R) = 0 \tag{12}$$

Within the bulk liquid, we assume no flow so that at the liquidus isotherm the pressure is that of a motionless liquid; i.e.,

$$P(\text{liquidus}) = P_0 + \rho_{LO} g h \tag{13}$$

where P_0 is the pressure at the top of the liquid pool (approximately 1 atm.), ρ_{LO} is the density of the liquid, g is the gravitational constant, and h is the height of the liquid pool which varies with radius unless solidification is unidirectional.

At the solidus isotherm, liquid feeds the contraction of the solidifying eutectic so that

$$\vec{v} \text{ (solidus)} = - \left(\frac{\rho_{SE} - \rho_{LE}}{\rho_{LE}} \right) \vec{U}_E \qquad (14)$$

$\vec{U}_E$ is the solidus (eutectic) isotherm; in general, its components vary along the solidus. Solidified eutectic density is ρ_{SE}, and the density of the eutectic liquid is ρ_{LE}.

To solve Equation (10) requires that the temperature distribution within the mushy zone be known. In this work, temperature is determined experimentally. With temperature, the coefficients in Equation (10) can be determined because the local composition of the interdendritic liquid is only a function of the temperature as given by the phase diagram. For the model system employed, Al-4% Cu and Sn-15% Pb, the phase diagrams used are given in Figures 13a and 14a. It is also necessary that the local values of liquid and solid densities be known throughout the mushy zone; the densities are given in Figures 13b and 14b for the two model alloys. Finally, the local volume fraction of liquid, g_L, must also be known to calculate the coefficients in Equation (10); however, their values are not known until Equation (10) is first solved and then

Equation (9) is satisfied. Therefore, a numerical technique is employed
to arrive at the correct values of g_L.

The sequence of calculations directed by the computer code is
outlined in Figure 15. After the input has been assimilated, the pressure
distribution is found according to finite-difference approximations of
Equations (10) - (14). At this point, reasonable approximations of g_L
are used as input; we have used the Scheil equation[47] in the form
which gives g_L as a function of temperature. The velocity field within
the mushy zone is then evaluated according to Equation (1) which leads
directly to a solution of Equation (9) giving "updated" values of g_L.
Calculations are repeated by replacing the initial values of g_L (estimated
with the Scheil equation) with "updated" values. The process is
continued until there is no change in values of g_L in the mushy zone.

Finally, macrosegregation in an ingot is given in terms of the
local average composition of solid after solidification is complete.
This is[18]

$$\bar{C}_S = \frac{\rho_S k \int_0^{1-g_E} C_L \, dg_S + \rho_{SE} g_E C_E}{\rho_S (1 - g_E) + \rho_{SE} g_E} \tag{15}$$

In Equation (15), g_E is the volume fraction of eutectic and C_E is the
eutectic composition. The integration in the numerator can be carried
out by picturing a fixed unit volume in which C_L continuously changes in
a known manner as the alloy solidifies. For an ESR ingot, when the
isotherms move at a steady velocity, the integration can be carried out

by integrating from the liquidus ($g_S = 0$) down to the solidus ($g_S = 1-g_E$) at a given radius. By doing this for different radial positions within the ingot, $\bar{C}_S$ versus radius is determined which can be plotted to give the pattern of macrosegregation.

To sum up, the analytical model (given a temperature distribution) can be used to predict:

(1) the pressure distribution within the mushy zone;

(2) the velocity of interdendritic liquid flow within the mushy zone;

(3) the distribution of volume fraction liquid within the mushy zone; and

(4) the local average composition after solidification is complete.

Accordingly, from step (4) the extent and pattern of macrosegregation is calculated which shows a continuous variation in composition from surface to center. Appendix B discusses in more detail the finite difference equations and other features of the computer code used to analyze macrosegregation.

B. Flow Instability and Localized Segregates

Up to this point solidification is pictured as progressively taking place as the temperature within the mushy zone decreases. Interdendritic liquid flows towards regions of increasing amounts of solid; i.e., flow is from hotter to colder regions in the mushy zone and is said to be "stable". However, as discussed by Mehrabian et al[17], under certain

conditions flow may become "unstable" with consequent formation of highly segregated channels called "freckles" when they occur in ESR ingots.

Figure 16 shows flow channels under conditions of "intermediate" flow, and "unstable" flow. These flows occur whenever $\vec{v} \cdot \nabla T / \epsilon < 0$; that is, whenever flow is from cooler to hotter regions. This can most easily be seen by first multiplying Equation (10) by (dC_L/dT) to obtain the local fraction of liquid as a function of temperature which is

$$\frac{\partial g_L}{\partial T} = - \left[\frac{1 - \beta}{1 - k} \quad \frac{g_L}{C_L} \frac{\partial C_L}{\partial T} \right] (1 + \frac{\vec{v} \cdot \nabla T}{\epsilon}) \qquad (16)$$

The quantity inside the brackets is always negative, regardless of the value of k. Now, imagine a perturbation such that one of the channels in the volume element sketched in Figure 16 becomes slightly larger than the surrounding channels. Resistance to flow through this channel is decreased, and flow (absolute value of $\vec{v}$) is increased, whatever its direction. If in addition, however, flow is in a direction of increasing temperature $(\vec{v} \cdot \nabla T / \epsilon < -1)$ then $\partial g_L / \partial T$ is negative, i.e., as temperature decreases, the local volume fraction liquid increases and so there is a driving force for the formation of channels; local melting occurs.

Consider the effect of a minor perturbation in the size of a flow channel when some flow occurs in the direction of isotherm movement. Specifically, consider the case when $0 < \vec{v} \cdot \nabla T / \epsilon < -1$. From Equation (16), the greater the flow, the less is the rate of solidification in a given channel. As sketched in Figure 16, therefore, the size of the perturbed channel does not decrease as rapidly as that of its neighbors during

solidification. However, as long as $\vec{v}\cdot\nabla T/\varepsilon$ remains within the limits given above, $\partial g_L/\partial T$ remains negative, and so no remelting occurs. If, however, the condition $\vec{v}\cdot\nabla T/\varepsilon < -1$ is reached in the perturbed channel, remelting does occur, and the size of the perturbed channel actually grows during cooling of the volume element. Growth can occur until it becomes optically visible as a "freckle".
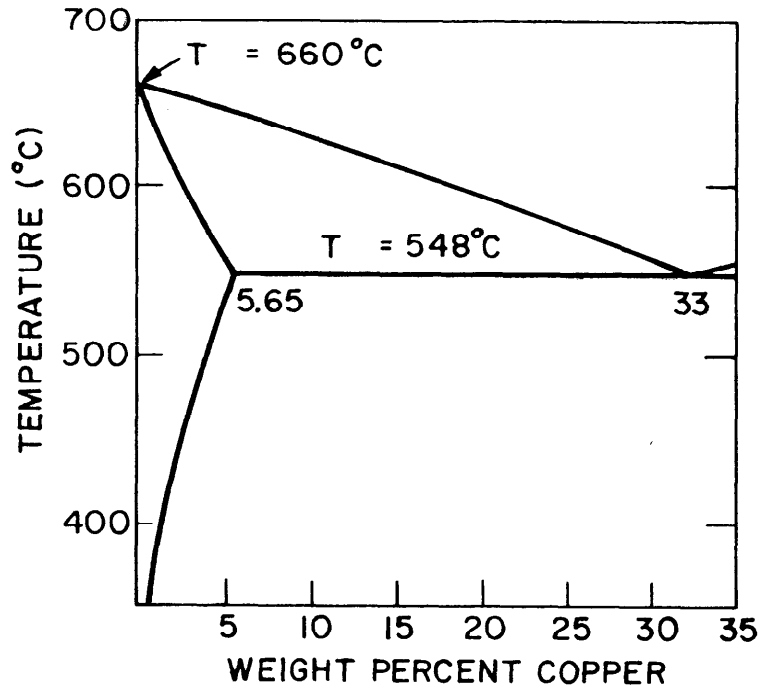
(a)
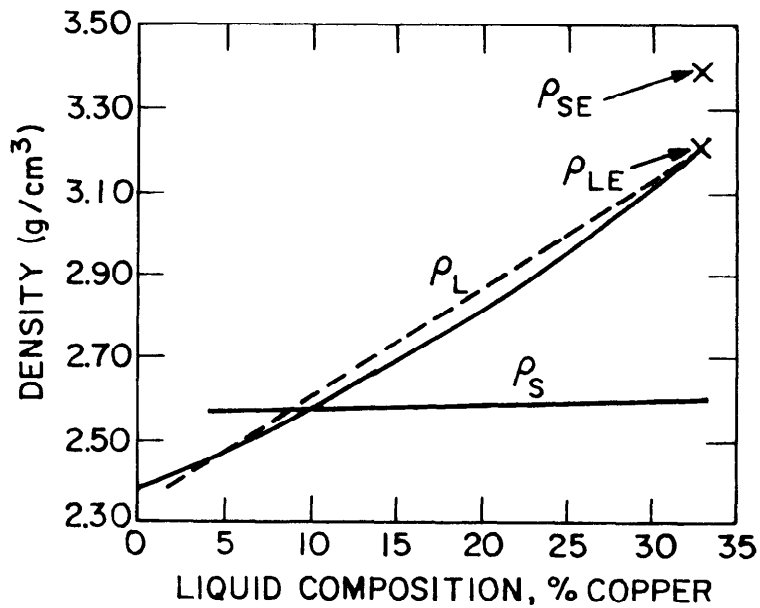
(b)

Figure 13: Phase diagram and density used for calculations of macrosegregation in Al-4% Cu ESR ingots. (a) Phase diagram, Ref. 41; (b) density of solid and liquid during solidification, Ref. 17.
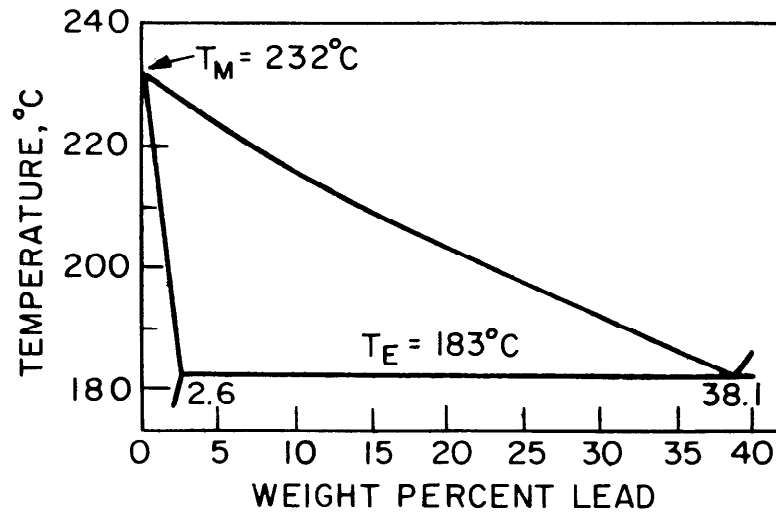
(a)
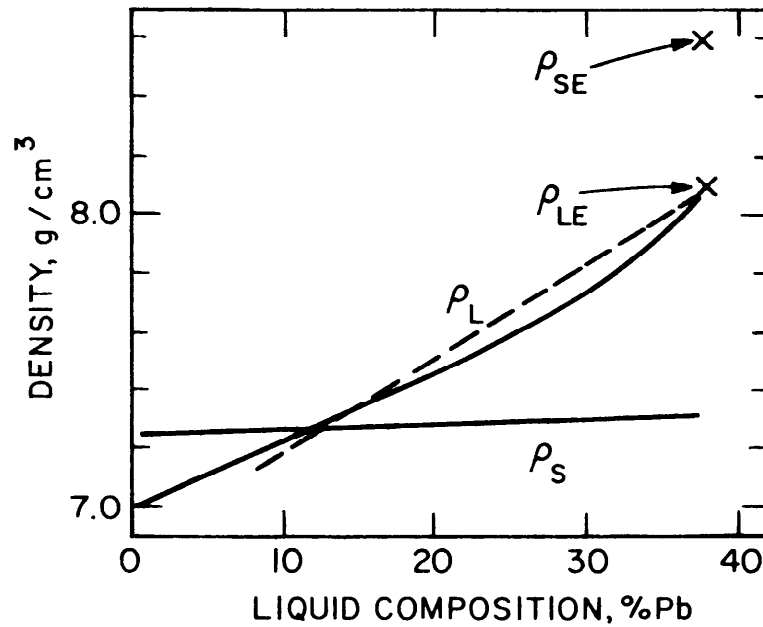
(b)

Figure 14:   Phase diagram and density used for calculations of
            macrosegregation in Sn-20% Pb ESR ingots.   (a) Phase
            diagram, Ref. 42;   (b) density of solid and liquid
            during solidification, Refs. 43-46.

35
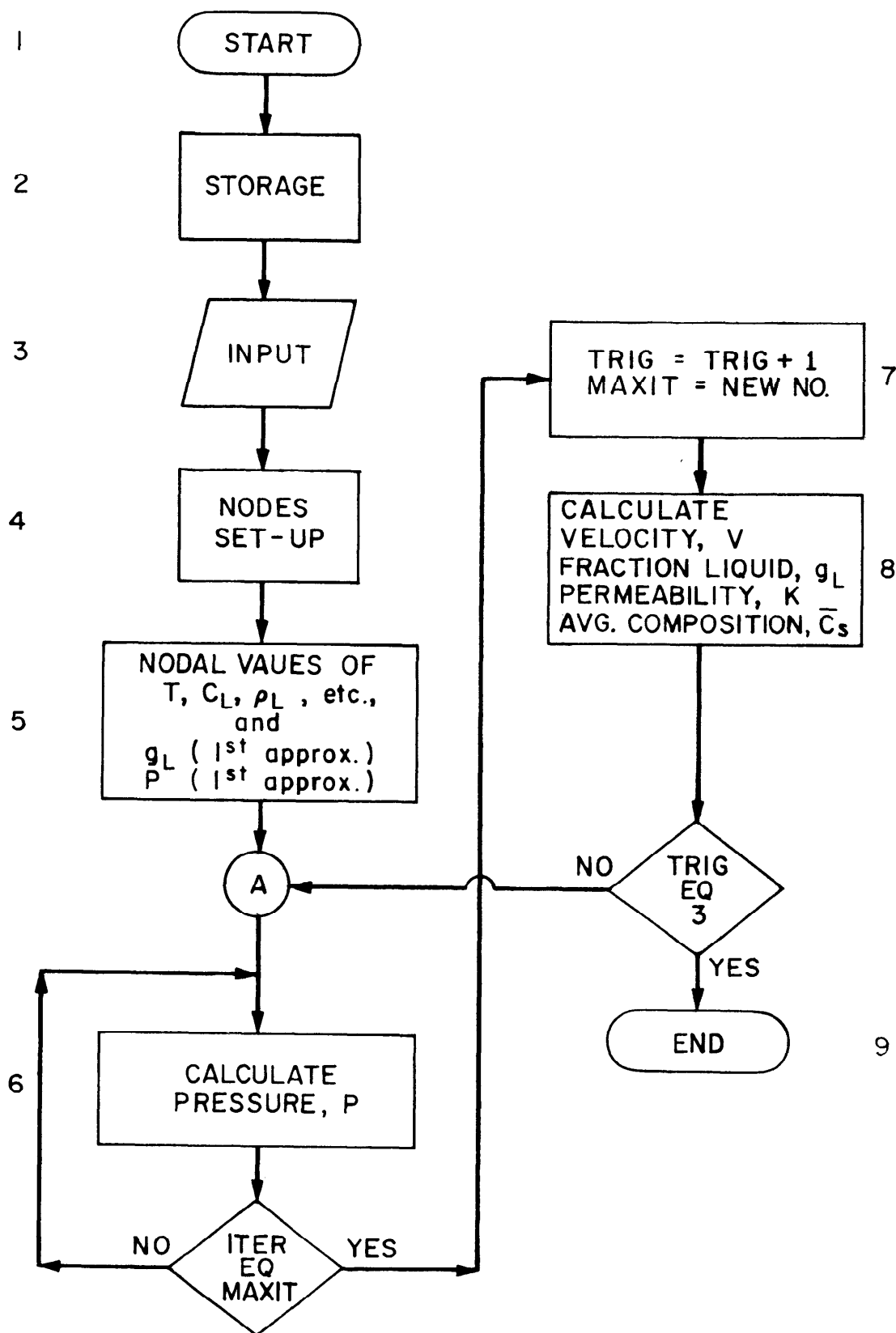
Figure 15: Flow chart of computer program to simulate macrosegregation.

$$\frac{\vec{v} \cdot \nabla T}{\epsilon} > 0$$

$$0 > \frac{\vec{v} \cdot \nabla T}{\epsilon} > -1$$

$$\frac{\vec{v} \cdot \nabla T}{\epsilon} < -1$$

STABLE   INTERMEDIATE   UNSTABLE
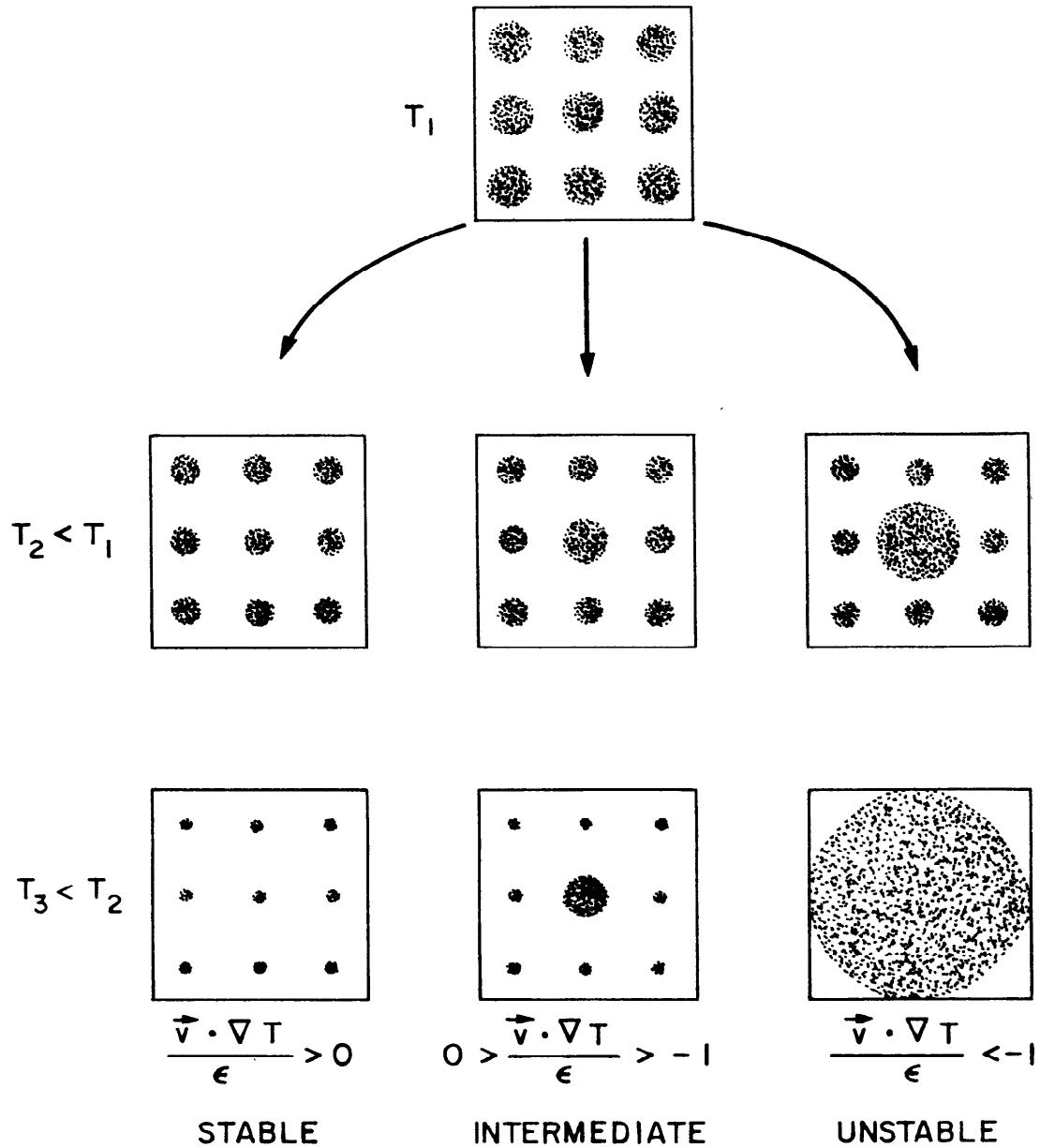
Figure 16:   Schematic illustration of change in flow channels during solidification. From Ref. 17.

IV. APPARATUS AND EXPERIMENTAL PROCEDURE

A. General

Two different types of experimental apparatus were employed in this work, and these are each described below. The first (employed for Al-4% Cu alloy) is a small scale ESR unit. This unit comprises a DC power source, a water cooled mold, a consumable electrode, and slag layer as in conventional ESR, Figure 1.

The second type of apparatus employed is one which simulates the solidification behavior of the ESR process, but does not employ slag. This unit, used for Sn-15% Pb alloy, comprises a source of molten alloy droplets, a cooled mold, and a heat source to simulate the heat input of the ESR process, Figure 2.

B. Small Scale ESR Unit

1. Apparatus

A sketch of the apparatus is shown in Figure 1 and, with the exception of the mold, is the same previously used by Basaran et al[12]. The power supply is a D.C. arc-welder capable of providing up to 1600 amp. and 40 volts for a total power of 55 KW (Miller Electric, SR 1000 BI). The electrode mount is connected to a feed screw about 6 feet long which is driven by one of two gear reduction boxes in series with an electric motor. The driving speed of the electrode is controlled by a Minarik

controller (Model SH-63); in this way the electrode can be operated with a linear speed in the range of 0.2 - 14 cm/min. The electrodes used were 2024 rods (Al-4% Cu) 1 inch in diameter by 6 feet long.

In the initial stages of the work, copper molds were designed and fabricated to provide for the flow of cooling water through the annulus between the closed jacket and the mold exterior (Figure 17). The inside dimensions of the mold were 3 inches in diameter by 8 inches high. A thin wash of aluminum oxide powder was applied to the mold wall in an attempt to eliminate corrosion of the mold by the slag (45% LiCl - 55% KCl). Several preliminary ingots were made in order to establish workable electrode power settings, slag volumes, and start-up techniques. Mold corrosion was a persistent problem particularly since the corrosion was sometimes localized making it necessary to fabricate new molds. Other mold washes were tried, such as a graphite wash and a wash composed of graphite and zirconia. The latter reduced the severity of the slag attack but molds were still attacked perchance the coating spalled during a run.

A second mold was designed mainly to incorporate the feature of being able to merely replace the mold wall rather than completely fabricate an entire mold. This design also made it easy to insert up to 5 thermocouples into the ingots during a run. This design is shown in Figure 18. Cooling water was sealed from the mold interior at the thermocouple entries with rubber rings. The replaceable copper mold was 3 inches in diameter by 14 inches in height. An aluminum bottom hearth

was used for bottom welding at start-up and to prevent slag corrosion of the copper bottom chill.

2. Experimental Procedure

About 250 c.c. of liquid KCl - LiCl slag of eutectic composition (45 wt% LiCl and 55 wt% KCl) was poured into the mold at start-up. Immediately after pouring the slag, the arc-welder was turned on to initiate melting with a power of 10 KW. The cooling water was turned on, and then the power was lowered to the working value between 2 and 4 KW. The amperage was kept constant by adjusting the driving speed of the electrode, and the electrode position was recorded during a run. When thermal data were desired, five chromel-alumel thermocouples were used. They were inserted into the mold and pushed to predetermined positions (shown as X's in Figure 18) immediately after the electrode passed these positions, and their output was recorded. Cooling curves obtained were used to determine the shape of mushy zone, temperature distribution, cooling rates and solidification rates. Thermal data for two ingots (Numbers 1 and 2) were obtained with the second mold design (Figure 18).

Three ingots, made in the first mold design (Figure 17) were doped with about five grams of Al-50% Cu to reveal the liquid pool shape. The ingots were cut into sections in order to obtain analyses by X-ray fluorescence to detect macrosegregation across the ingots. The ingots were also macroetched with Keller's etch to reveal the doping effect, and samples for microstructures were removed.

C. Simulated ESR Apparatus

1. Apparatus

A sketch of the apparatus is shown in Figure 2. The stainless steel mold is 3-1/4 in. in diameter and 13 in. long. The metal pool inside the mold is heated with six, 3 in. long, resistance heaters (G 3A133 Wattlow Electric Manufacturing Company) connected in parallel. These heaters were positioned inside holes drilled into a 3 in. long by 1-1/4 in. diameter stainless steel bar. They were connected in series to a 240-volt variare used to adjust and control the power input.

Cooling water runs through a movable cooling jacket surrounding the mold. Both the resistance heaters and the cooler are fixed to the same system used for driving the electrodes in making the Al-4% Cu ingots. Thermal measurements are made with three chromel-chromel thermocouples located inside three vertical stainless steel tubes. The tubes are fixed, but the position of the thermocouples is varied during a run by sliding them up and down inside the tubes.

In this analog set-up, the flow of liquid Sn-15% Pb alloy from the top stainless steel container is controlled by an adjustable valve. Heating of the melt in the top container is done with two 8 in. diameter by 1.5 in. wide band heaters (7533EX, Wattlow Electric Manufacturing Company). These heaters are controlled by a thermocouple hooked up with a Eurotherm temperature controller (917/FCP/K/600/115/230V/A/C2). A stirrer was used to insure uniform concentration distribution in the bath of the top container.

2. <u>Experimental Procedure</u>

Pure tin (99.9%) and pure lead (99.9%) of known weights were melted together in a crucible furnace. The liquid alloy was well stirred and about one-fourth of the charge was poured into the stainless steel mold until the liquid level rose to almost the top of the resistance heaters (about 3.5 in. from the bottom of the mold). The remaining alloy was then poured into the top container. Both the band heaters and the resistance heaters were then turned on. The cooling water was also turned on at the same time.

With the resistance heaters and the cooling jacket fixed, the initial position and the shape of the mushy zone were determined by moving the three thermocouples up and down and locating the position of the liquidus and solidus temperatures of the alloy. Power input to the heaters and cooling jacket position were adjusted until the desired position and shape of mushy zone were obtained.

Then, the resistance heaters and the cooler were moved upwards at the predetermined speed and the valve of the top container was adjusted so that the liquid level inside the mold rose at the same speed. As solidification progressed the three thermocouples were individually moved up and down so that a trace of solidus and liquidus temperature could be made along with the temperature distribution in the mushy zone. The position and time of each thermocouple reading were recorded. These thermal measurements were used to determine the position and the shape

of the mushy zone, the temperature distribution, and the cooling rates during solidification.

The ingot cast was cut into sections for microstructural study and analysis by X-ray fluorescence to determine degree of macrosegregation.

D. Chemical Analysis

Chemical analysis of macrosegregation in the ingots was by X-ray fluorescence. A General Electric X-ray diffraction unit (Model XRD3 Type 1) was used with a Mo tube. The primary white radiation from the tube fluoresced the samples on an area of 0.32 cm. diameter. This area covered many dendrite arms (secondary dendrite arm spacing is about 40μ) and, therefore, the compositions measured were local average compositions.

The secondary radiation from the sample was received by a Si (Li) X-ray detector (ORTEC Model 78915-10225) and the intensity of the characteristic line (K_α for Cu and L_α for Pb) was compared with a standard intensity versus composition curve to determine the composition.

The standards were prepared from rapidly cooled thin sections of known compositions. The Al-Cu standards used were those prepared by Nereo[48]. The Pb-Sn standards were prepared by melting pure lead and pure tin together in a graphite crucible to form the liquid alloy of desired composition. The liquid alloy was heated above 500°C, well stirred and skimmed. About 5 grams of the liquid alloy was quickly removed from the crucible and dropped 1.5 feet onto a copper chill (1.5 inches x 6 inches x 10 inches). The descending drop of liquid alloy hit

the copper and solidified very rapidly as a splat. A significant portion of the splat formed an area which was similar to a thin disk (about 0.8 mm. thick and 2 in. in diameter) with a very smooth and flat bottom surface. From the disk, a thin plate was then cut into a rectangular plate (0.8 inch x 1.2 inches) and polished to 600 grit metallographic paper for X-ray fluorescence. The remainder of the disk was analyzed by wet chemical analysis to determine the composition.
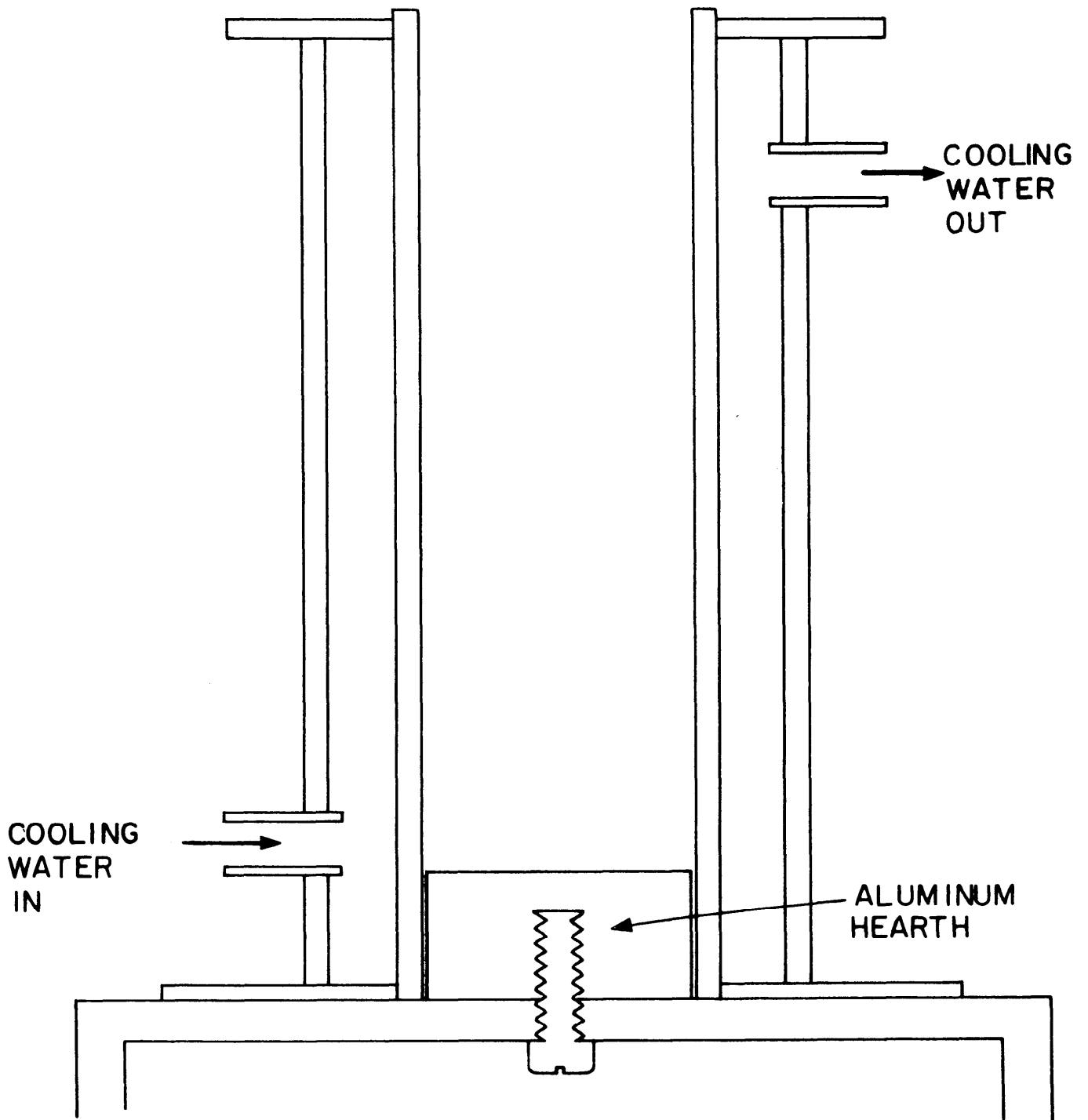
COOLING
WATER
OUT

COOLING
WATER
IN

ALUMINUM
HEARTH

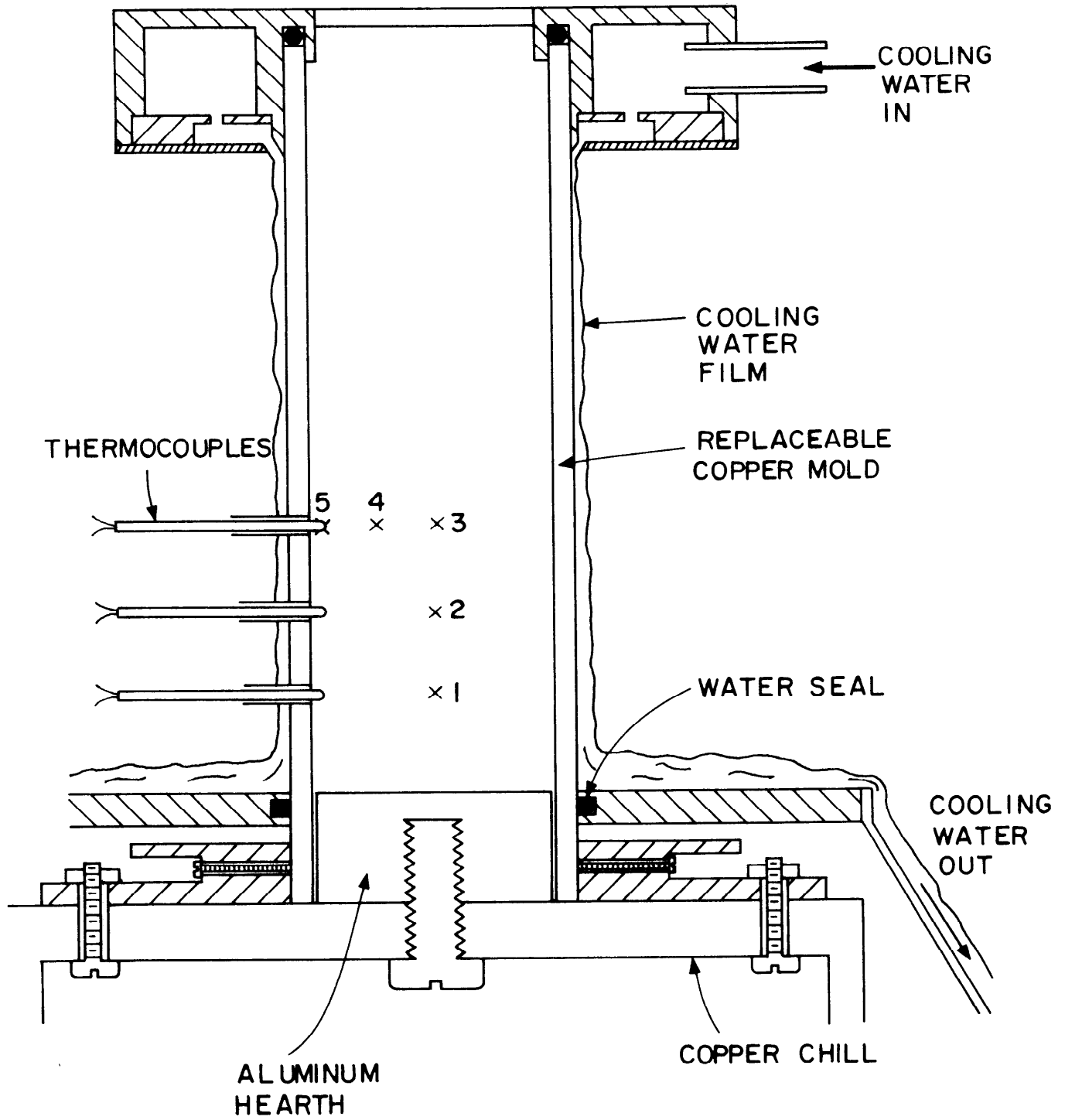Figure 17:   ESR mold design with brazed cooling-water jacket.

Figure 18: ESR mold design with replaceable mold wall. Numbers
indicate thermocouples.

V. EXPERIMENTAL RESULTS OF MACROSEGREGATION

A. Aluminum-4% Copper ESR Ingots

Results of five ingots are given which encompass an ingot with the deepest isotherm shapes obtained (No. 1), an ingot with flat isotherms (No. 2; i.e., unidirectional) and three ingots with isotherms of shapes intermediate between the deepest and the flat isotherms (Nos. 3, 4, and 5). The isotherms for ingots 1 and 2 were obtained from thermal measurements; for ingots 3, 4, and 5 the shapes of the isotherms were determined by doping.

The thermal data and measured compositions (to show degree of macrosegregation) in these five ingots follow in this section. Additional discussion of the experimental results is given later in this report in conjunction with calculations resulting from the analytical study of macrosegregation.

1. Ingot No. 1

The cooling curves obtained from the thermocouples as positioned in Figure 18 are given in Figure 19. Thermocouples 1, 2, and 3 were located along the ingot axis respectively, from the bottom chill. At a given temperature, the time lag between thermocouples 1 and 2 is somewhat greater than between 2 and 3 indicating that the solidification rate increased slightly as solidification proceeds from the bottom. As

expected, thermocouples 4 and 5 cooled sooner than No. 3 because they were located closer to the ingot wall. The interesting fact regarding these cooling curves, however, is that cooling rate over the solidification range is independent of the distance from the bottom chill.

Figure 20 shows plots of the position of the liquidus isotherm (Z_L) and eutectic isotherm (Z_E) at the center of the ingot. After steady state is achieved, the isotherms move with a vertical speed of 0.053 cm/s. Figure 21 shows that the isotherm speed in the axial direction, at 7.6 cm. up from the bottom chill, is independent of radius since the time lag between the liquidus and solidus are equal for the three thermocouples.

Figures 19 - 21 can be used to determine the shape of the mushy zone. This is shown in Figure 3 after 7 minutes of ingot solidification has elapsed. As a consequence of cooling rate not varying with radius, the isotherms are parallel. Finally, temperature gradient in the mushy zone is shown in Figure 22. Since isotherms are parallel, this temperature gradient is independent of radius. Figures 19 - 22 provide the thermal data necessary as input to the computer simulation which calculates macrosegregation in Ingot 1.

Figure 5 shows the degree of macrosegregation obtained in Ingot 1 as measured by X-ray fluorescence. The overall analysis of the ingot is 4.4% Cu; as a result of solidification, there is positive segregation at the surface (about 4.6% Cu) and negative segregation at the center (about 4.25% Cu). Macroetching showed no evidence of localized segregates, such as "freckles" or "V"-segregates along the center line, so segregation is continuous from center to surface. Since commercial

2024 aluminum alloy containing titanium was used as electrode, the ingot structure is equiaxed and fine-grained; this is true of all five aluminum ingots.

Because the structure is equiaxed, measurements of the average dendrite cell size, $\bar{d}$, were made rather than the often reported measurements of secondary dendrite arm spacing. Here we define the dendrite-cell size as the distance between the centers of adjacent primary phases separated by eutectic constituent. The average value of the dendrite-cell size is obtained by drawing random lines over photomicrographs and counting the numer of intercepts between the lines and the eutectic constituent. About 200 intercepts for each sample were counted in photomicrographs with a magnification of 128X. Dendrite cell size, $\bar{d}$, in Ingot No. 1 is shown in Figure 23. No significant variation in $\bar{d}$ is observed which, of course, is predictable by the fact that cooling rate during solidification is also constant across the ingot.

2. Ingot No. 2

This ingot was cast and examined in the same manner as Ingot No. 1 with the exception that an unusually thick (about 0.3 cm.) coating of mold wash (graphite and powdered zirconia) was applied to the inside mold wall. As a result, solidification was unidirectional.

Figures 24 and 25 show cooling curves and isotherm positions, respectively. At 7.6 cm. from the bottom, temperature is independent of radius (Figure 24) so isotherms must be flat. Cooling rate during

solidification is about equal to that observed in Ingot 1, but the vertical temperature gradients are somewhat greater (Figure 25). Figure 26 shows the mushy zone after 7 minutes have elapsed, and Figure 23 shows the average dendrite cell size which is equal to that observed in Ingot No. 1.

Since solidification is unidirectional, no macrosegregation is detected in this ingot; nor is there any evidence of localized segregates found in an etched macrosection.

3. Ingots 3, 4, 5

Thermal data for these ingots were not measured, but with isotherm shapes obtained by doping and cooling rates calculated using measurements of dendrite cell sizes, the thermal history can be constructed.

Figure 27 shows the etched macrostructure of Ingot No. 4. The important feature seen is that doping outlines the shape of an isotherm. Since doping was carried out by suddenly increasing the composition of copper in the bulk liquid, then a melting back of the dendrite tips protruding into the liquid pool must have occurred. Therefore, the extent of this remelting must be known in order to predict the precise isotherm indicated by the doping in Figure 27. However, since thermal data for Ingots 1 and 2 indicate that isotherms are parallel and Ingots 1 and 2 represent the extremes in isotherm shapes, we assume that isotherms in Ingots 3, 4, and 5 are also parallel. As such, exactly which isotherm is brought out by doping is not an important consideration, but it is important to detect the shape of the isotherms.

Another indication that isotherms are parallel in these ingots is given in Figure 28; dendrite cell size in these ingots is uniform across each of the ingots which is consistent with the existence of parallel isotherms.

Figure 28 is used to deduce the local solidification times in Ingots 3, 4, and 5. For aluminum alloys, the secondary arm spacing, d is related to solidification time, θ, by[49]:

$$d = 7.5 \times 10^{-4}\theta^{0.39} \tag{17}$$

with d in cm. and θ in seconds. Dendrite cell size, $\bar{d}$, as defined herein would only equal d when, perchance, the plane of polish includes a row of aligned secondary dendrite arms and is parallel to the center of the arms. In general, therefore, for random planes $\bar{d}$ is greater than d, but the ratio $d/\bar{d}$ is a constant fraction. As such,

$$\bar{d} = A\theta^{0.39} \tag{18}$$

in which A is constant and greater than the proportionality constant in Equation (17).

Measured local solidification time of Ingot No. 1 is 95 s (average obtained from thermocouples 3, 4, and 5, in Figure 19); average dendrite cell size is 61.5×10^{-4} cm. (Figure 23). Similarly, for Ingot 2 (Figures 23 and 24), θ is 78 s and $\bar{d}$ is 61×10^{-4} cm. By calculating A for Ingots 1 and 2, and using the average value, we arrive at

$$\bar{d} = 1.08 \times 10^{-3}\theta^{0.39} \tag{19}$$

Values of $\bar{d}$ obtained from Figure 28 are then substituted into Equation (19) to determine the local solidification times in Ingots 3, 4, and 5. Results are 89, 89, and 54 s, respectively.

Degree of macrosegregation for Ingot 3 is shown in Figure 29. The extent of segregation is considerably less than that detected in Ingot 1 which has a deeper isotherm shape. The isotherms are more nearly flat in Ingots 4 and 5 (Figure 30), enough so that no segregation is detected in these ingots (Figure 31).

B. Tin-15% Lead ESR Analog Ingot

Results of macrosegregation in the series of the five Al-4% Cu experimental ingots show that severe-localized segregates, as sometimes found in large commercial ESR ingots, cannot be produced using this alloy cast by ESR in small laboratory scale (3 inches in diameter) molds. Although surface to center compositional variations were produced, these variations are rather modest and no severe-localized segregates were detected. It was decided, therefore, to design laboratory experiments which could be used to study a wider range of segregation problems encountered in ESR ingots. Accordingly, experimental efforts were directed towards solidifying Pb-15% Sn alloy in the simulated ESR apparatus (Figure 2). Results obtained from our initial ingot are very encouraging and experimental emphasis will continue on the analog apparatus and the Sn-Pb alloy selected as the model alloy.

Figure 32 shows thermal data obtained from the experiment made in the ESR-analog apparatus. The motion of the liquidus and non-equilibrium solidus is plotted for three radial positions: at the center, slightly beyond mid-radius, and almost at full-radius. After about 5 minutes all curves are linear and parallel which indicates steady state is achieved above 9 cm. from the ingot base. But the distance between isotherms varies with radius so the mushy zone is not comprised of parallel isotherms as in the experimental Al-4% Cu ESR ingots. Rather, as shown in Figure 4, the mushy zone is widest at ingot center and decreases as ingot radius is approached. Predictably, the microstructure shows finer dendrites near ingot radius, and they coarsen as the ingot center is approached (Figure 33).

In this ingot, macrosegregation is severe. Figure 6 shows that the composition varies from a high of about 26% Pb in the center to a minimum of 6% Pb slightly beyond mid-radius. The curve showing the overall segregation can only be drawn approximately since there are localized-segregates ("freckles") in this ingot. Figure 7 shows "freckles" at approximately mid-radius and an abnormally high fraction of eutectic constituent in the central zone. From an experimental viewpoint, therefore, the analog ESR experiment provides a method of producing, in the laboratory, the severe segregation sometimes found in large ESR ingots. As discussed later, our analytical studies confirm this conclusion and so we plan to conduct future experiments using this apparatus. Currently, the apparatus is being used by one of the authors (S.K.) to obtain experimental results for his Ph.D. thesis research work.
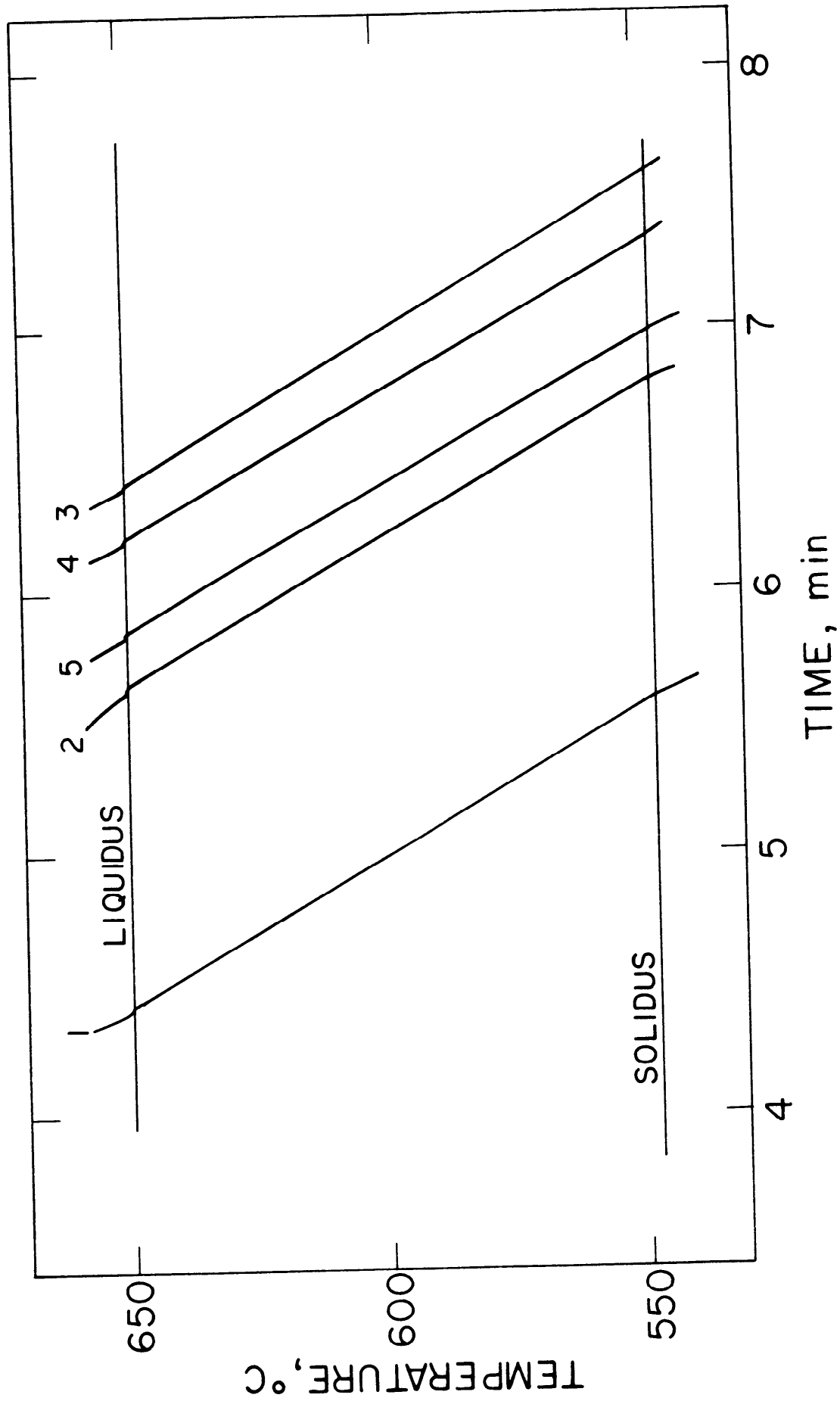
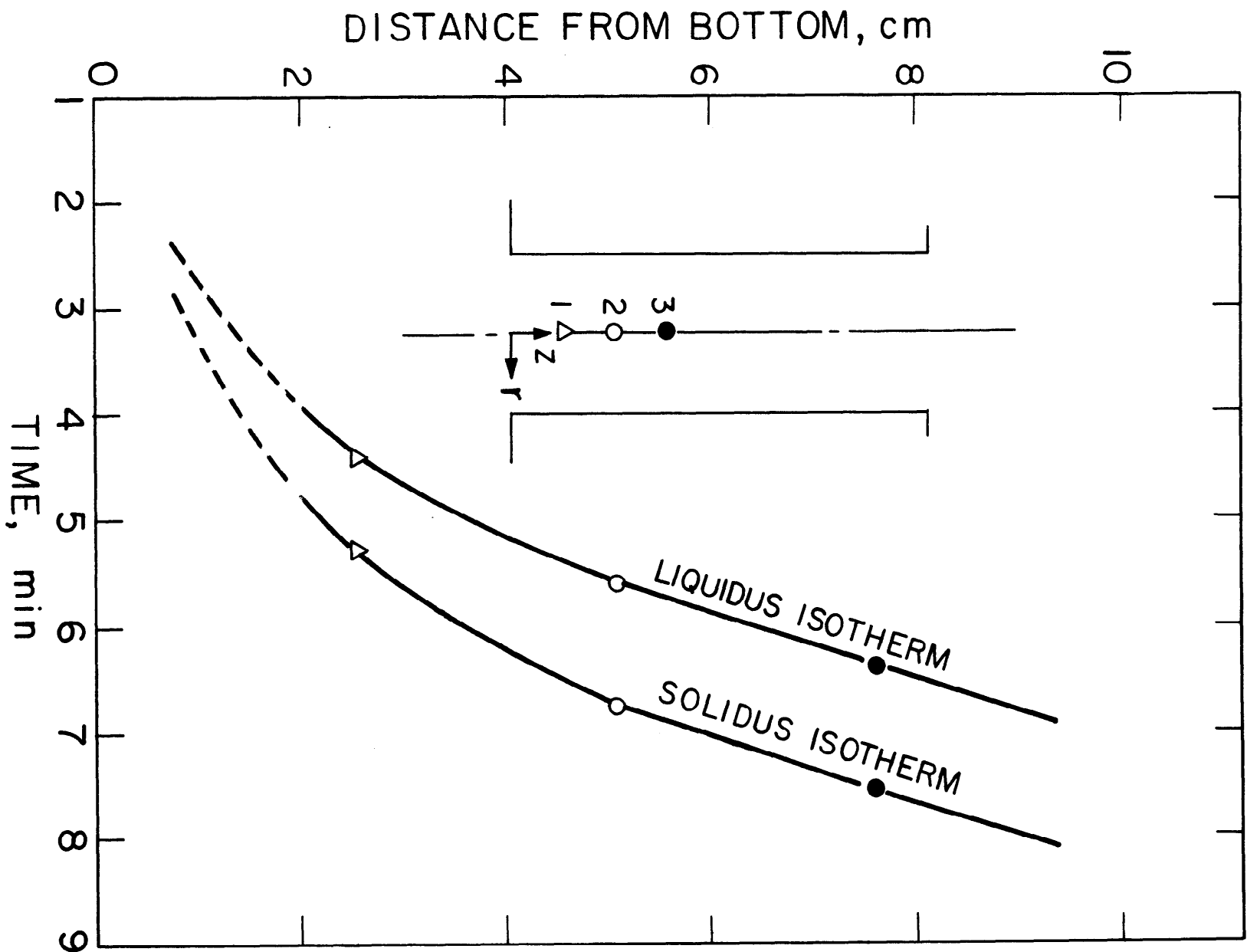Figure 19: Cooling curves for ingot 1 (Al-4% Cu). Numbers refer to thermocouples shown in Figure 9.

Figure 20: Liquidus and solidus isotherms along axis in ingot 1 (Al-4% Cu).
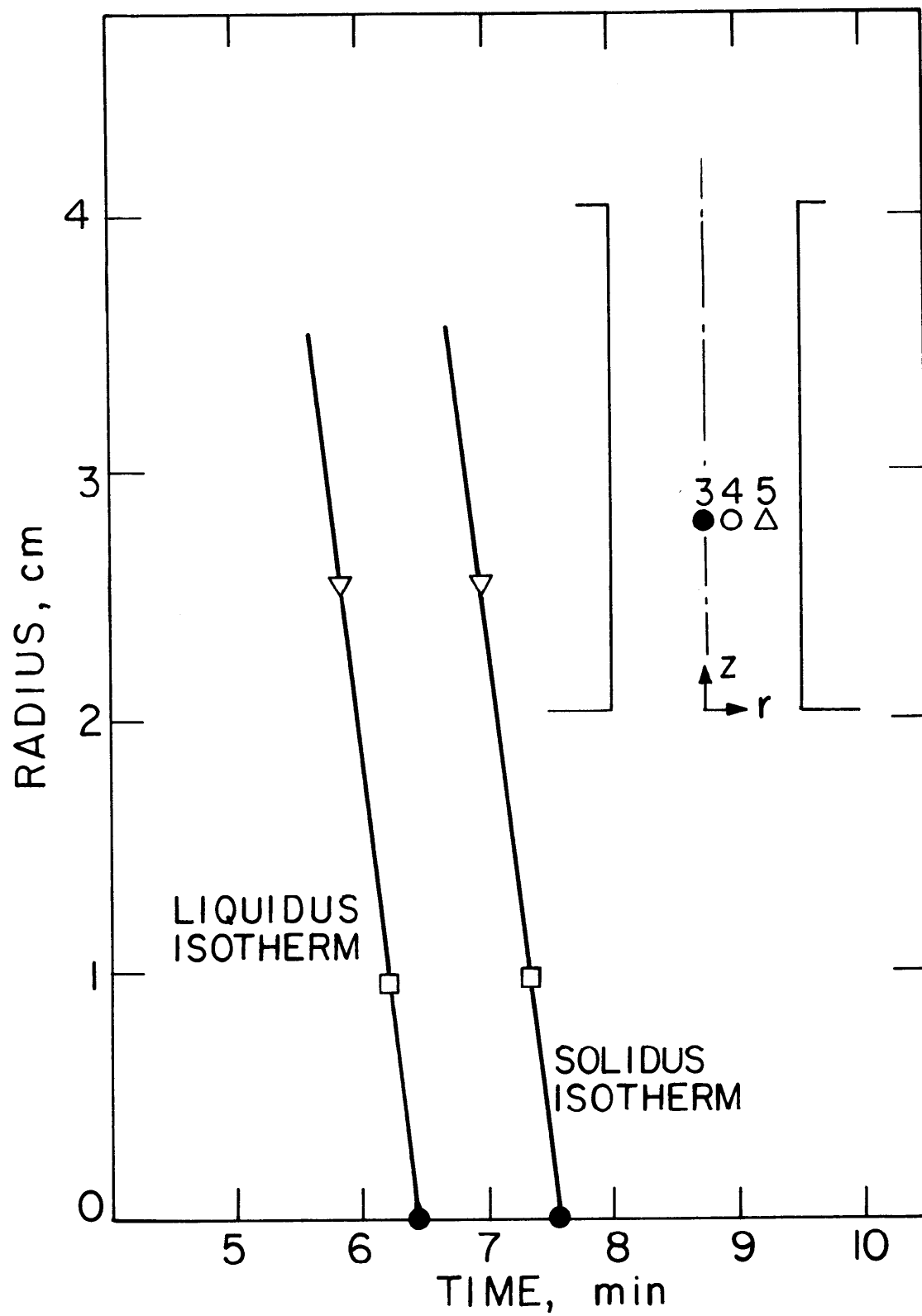
Figure 21: Liquidus and solidus isotherms with respect to radius at 7.6 cm from the bottom in ingot 1 (Al-4% Cu).
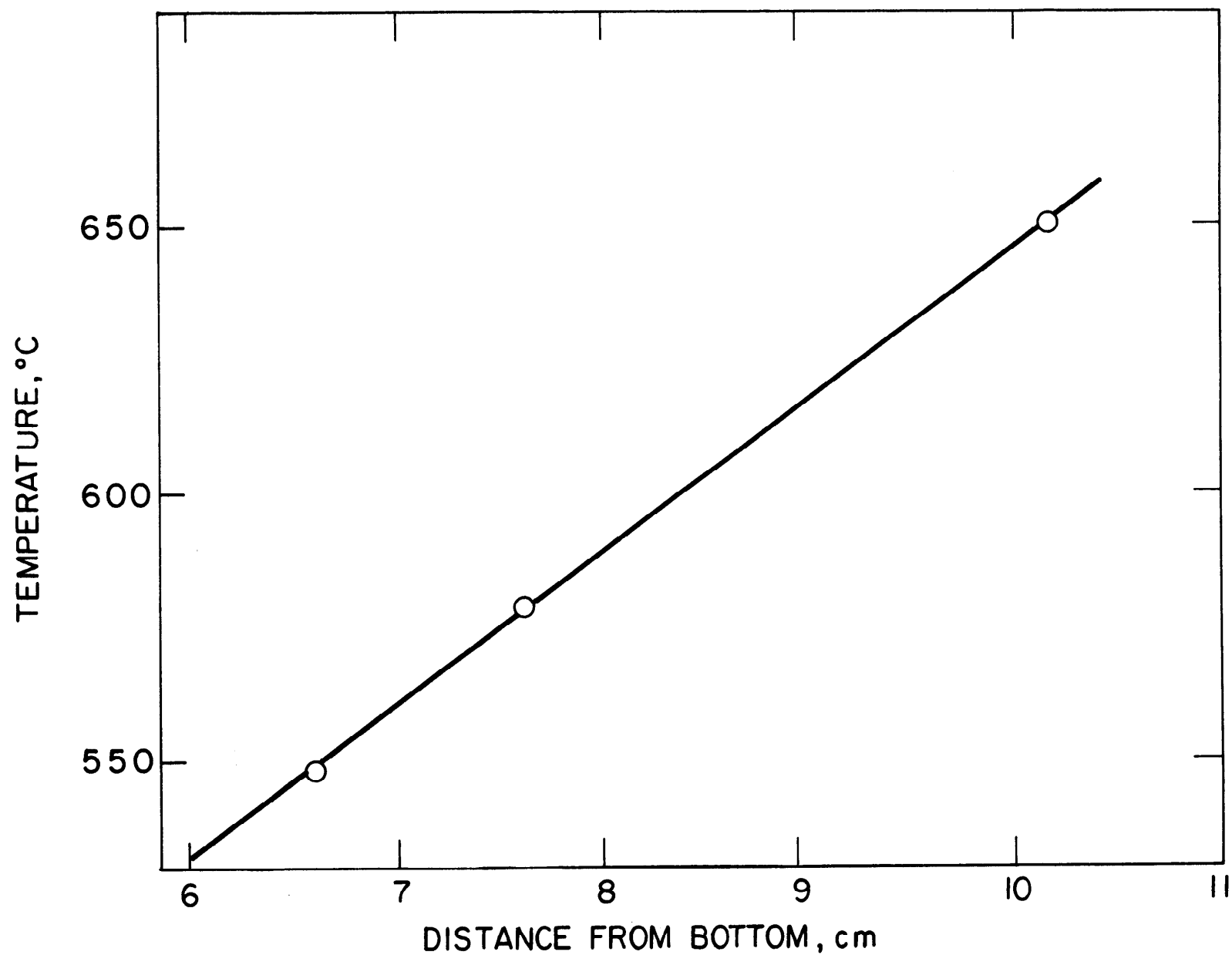
Figure 22: The temperature gradient in Ingot 1 (Al-4% Cu).
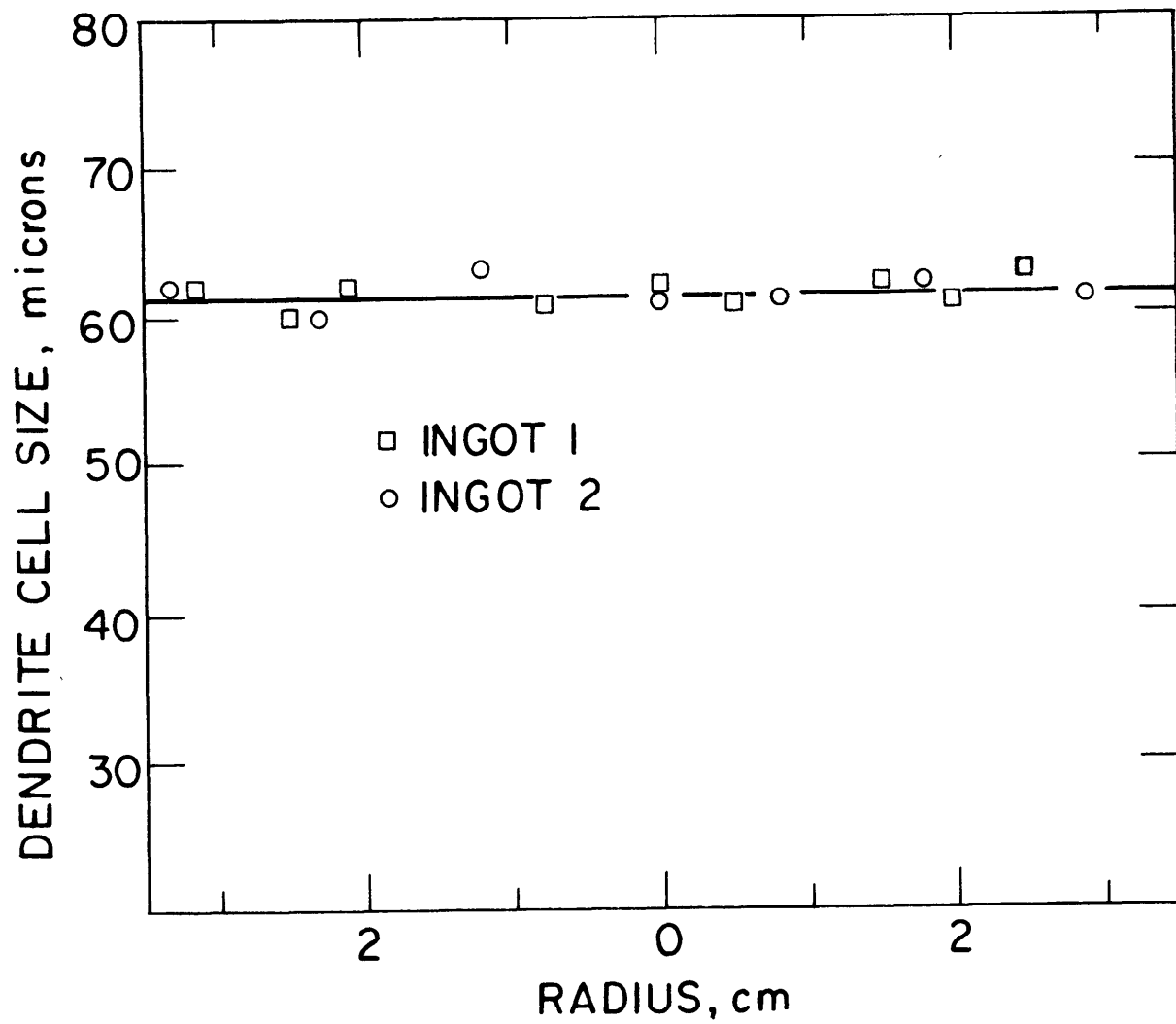
Figure 23: Dendrite cell size in ingots 1 and 2 (Al-4% Cu).
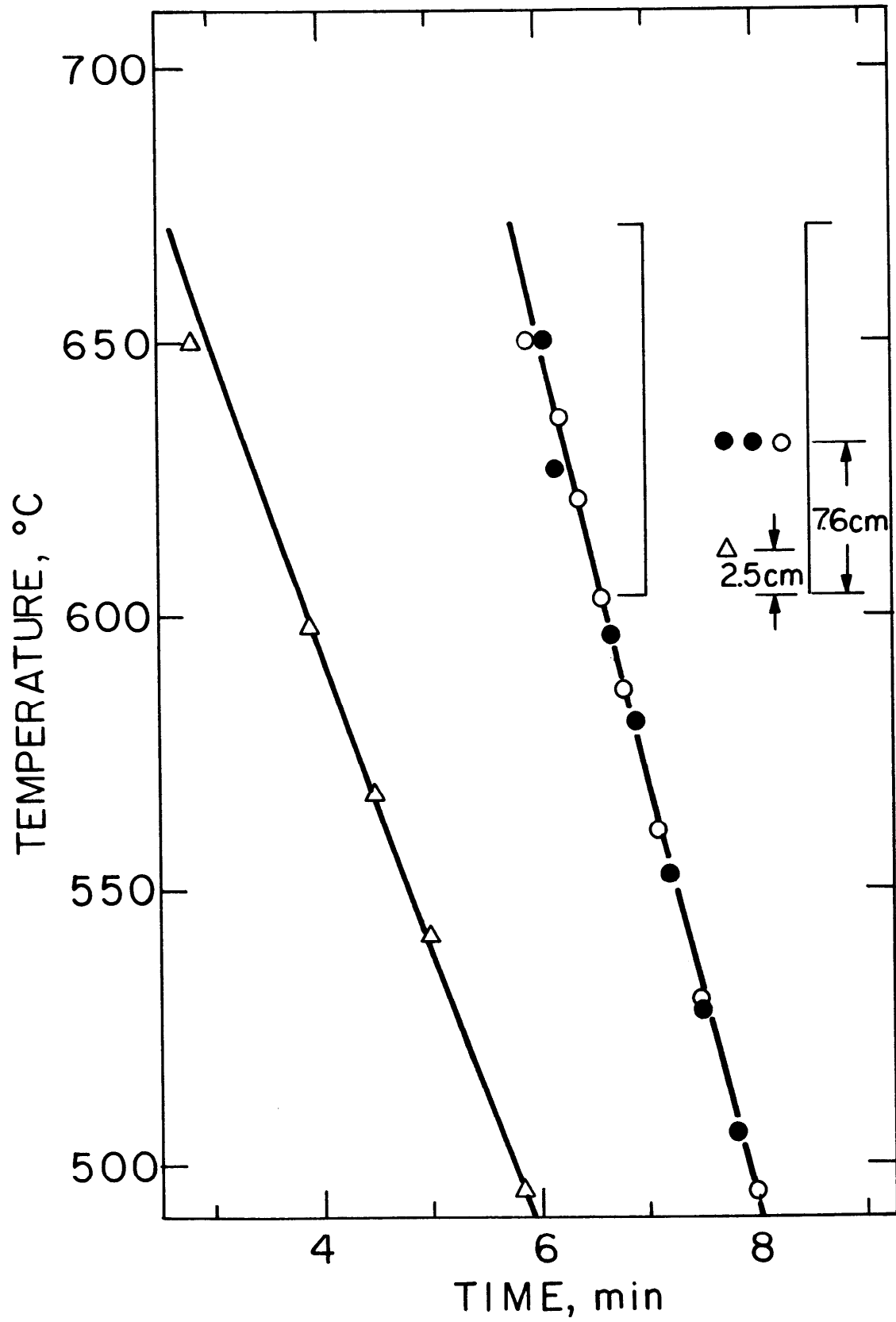
Figure 24: Cooling curves for ingot 2 (Al-4% Cu).
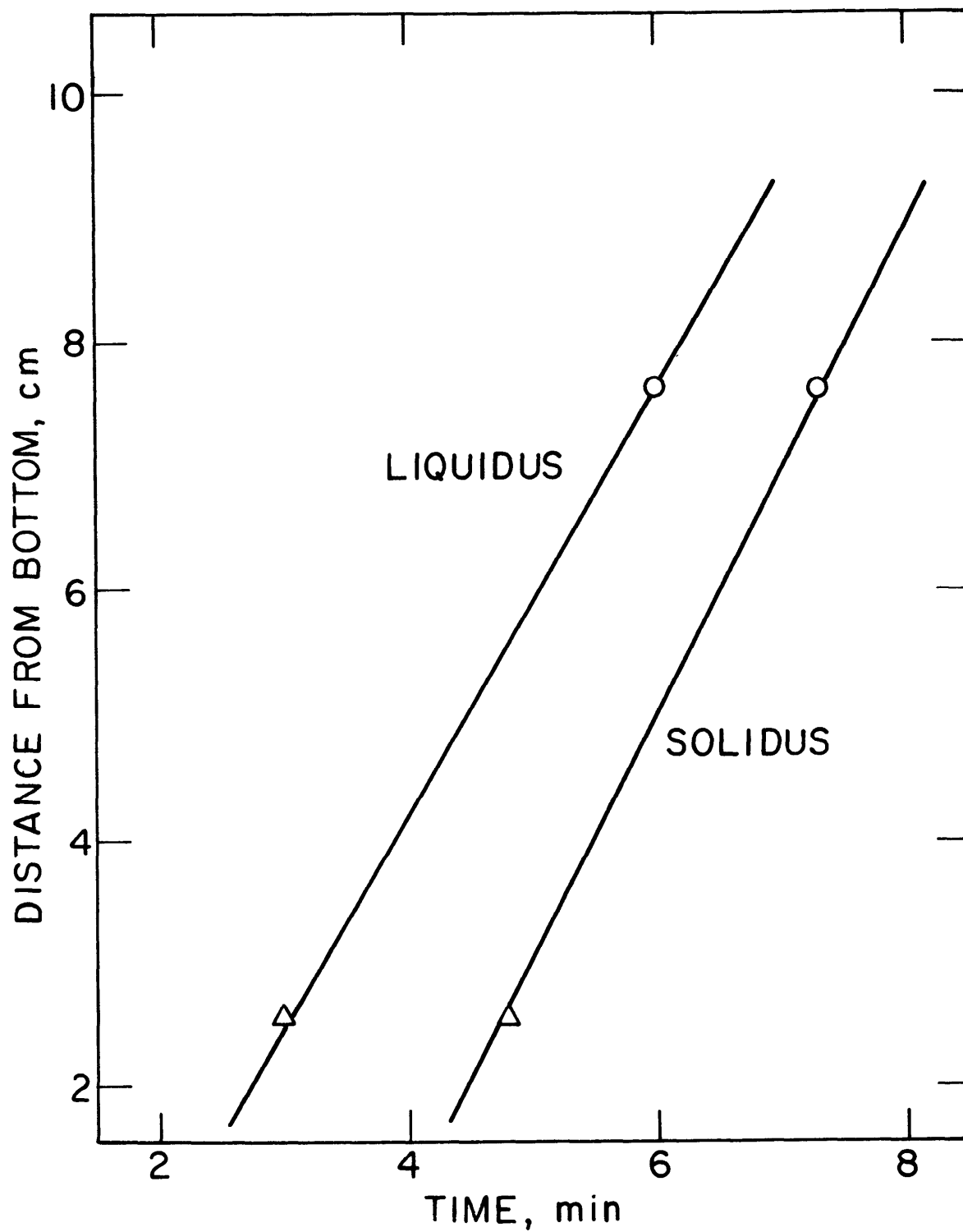
Figure 25: The liquidus and solidus isotherms in ingot 2 (Al-4% Cu).
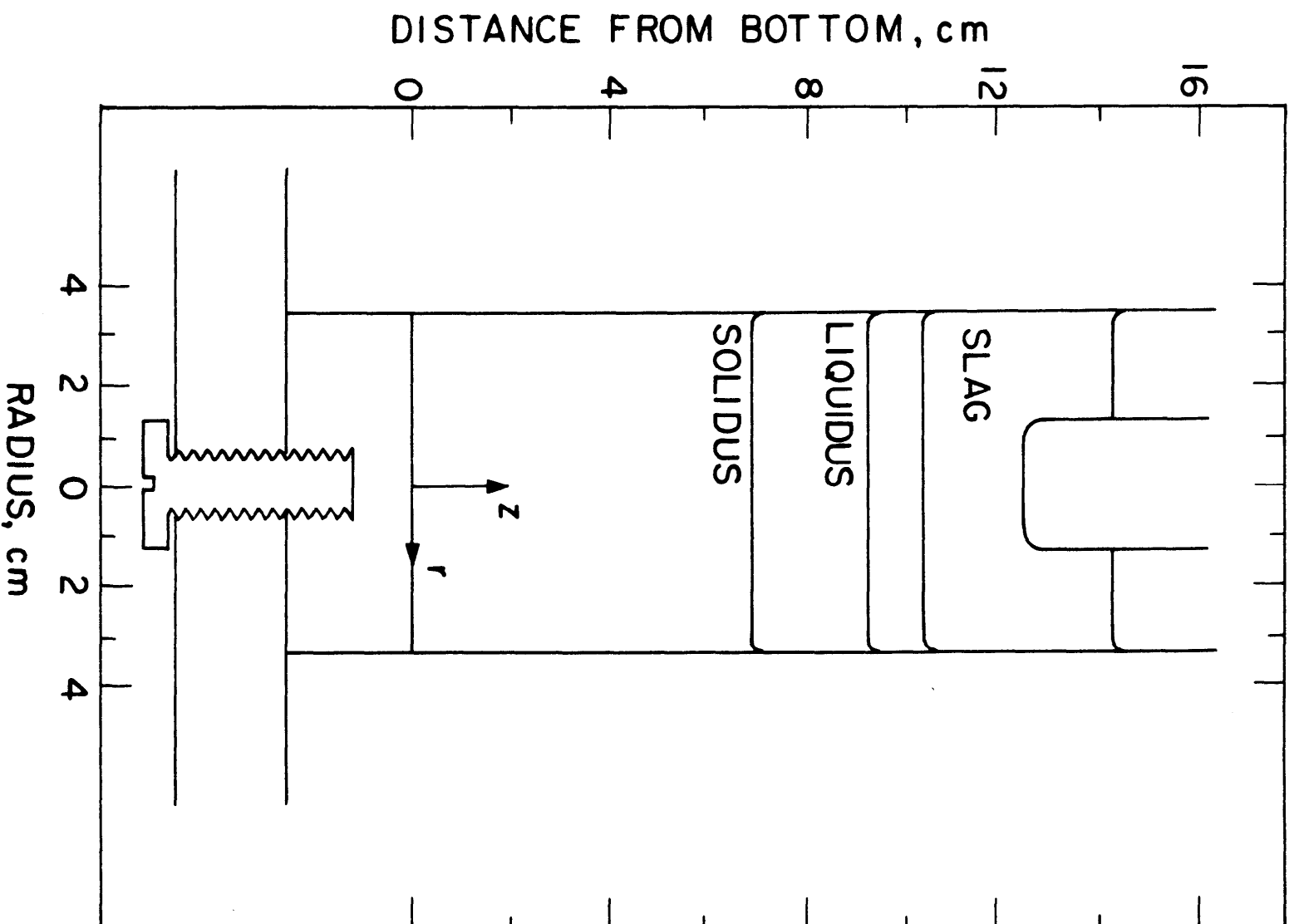
Figure 26: The shape of the mushy zone at 7 minutes in ingot 2 (Al-4% Cu).

60
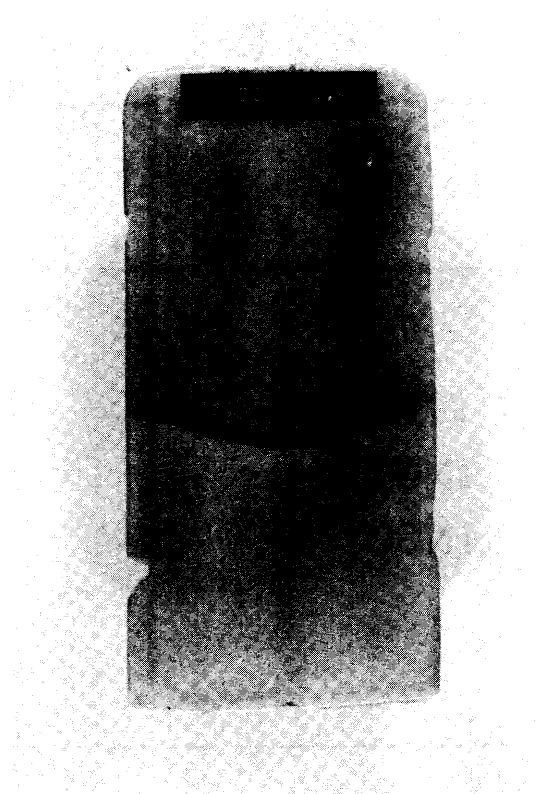
Figure 27: Isotherm detected by doping ingot 4 (Al-4% Cu).
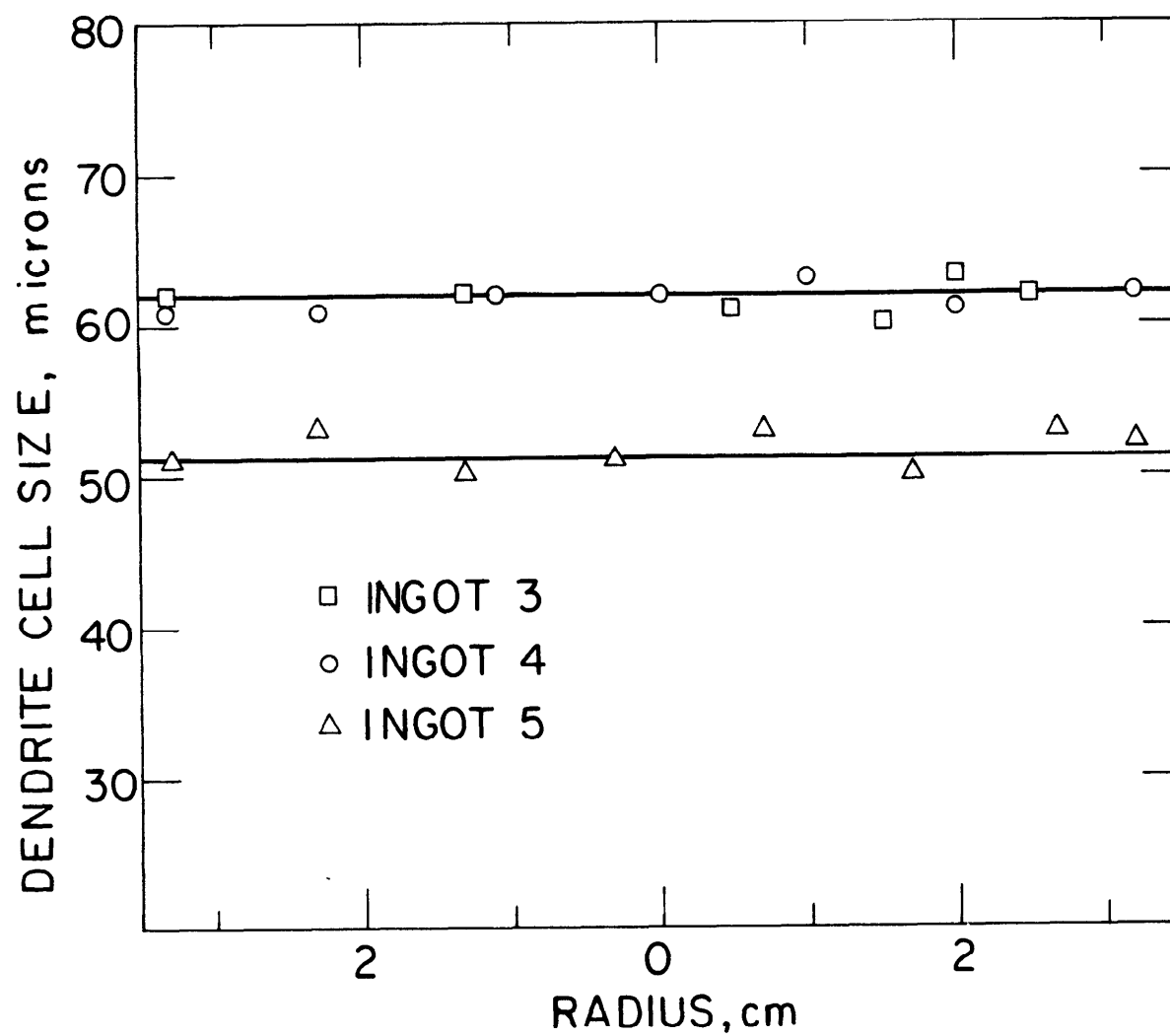
Figure 28: Dendrite cell size in ingots 3, 4, and 5 (Al-4% Cu).
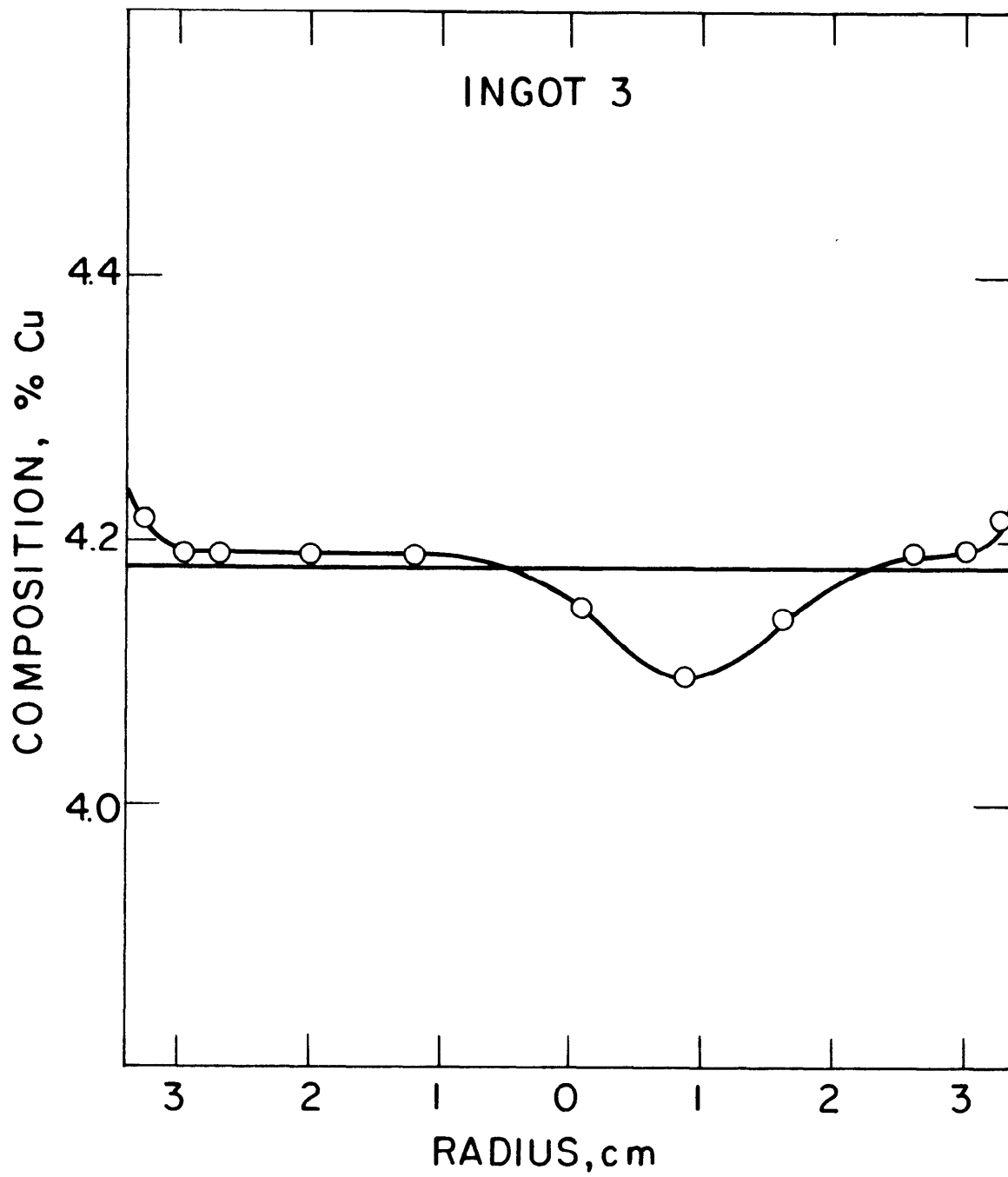
Figure 29: The macrosegregation pattern in ingot 3 (Al-4% Cu).
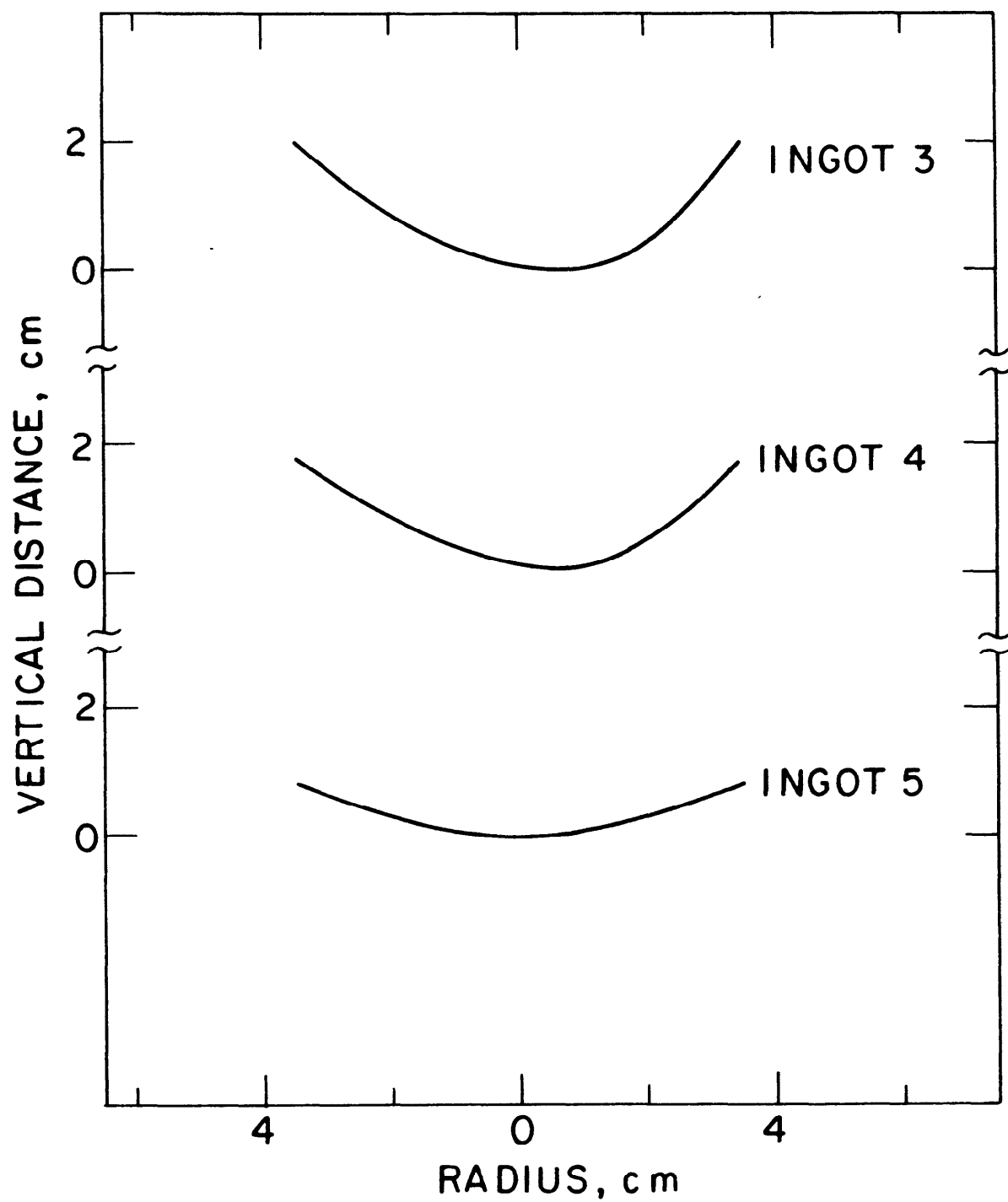
Figure 30: Shape of isotherms in ingots 3, 4, and 5 (Al-4% Cu) detected by doping.
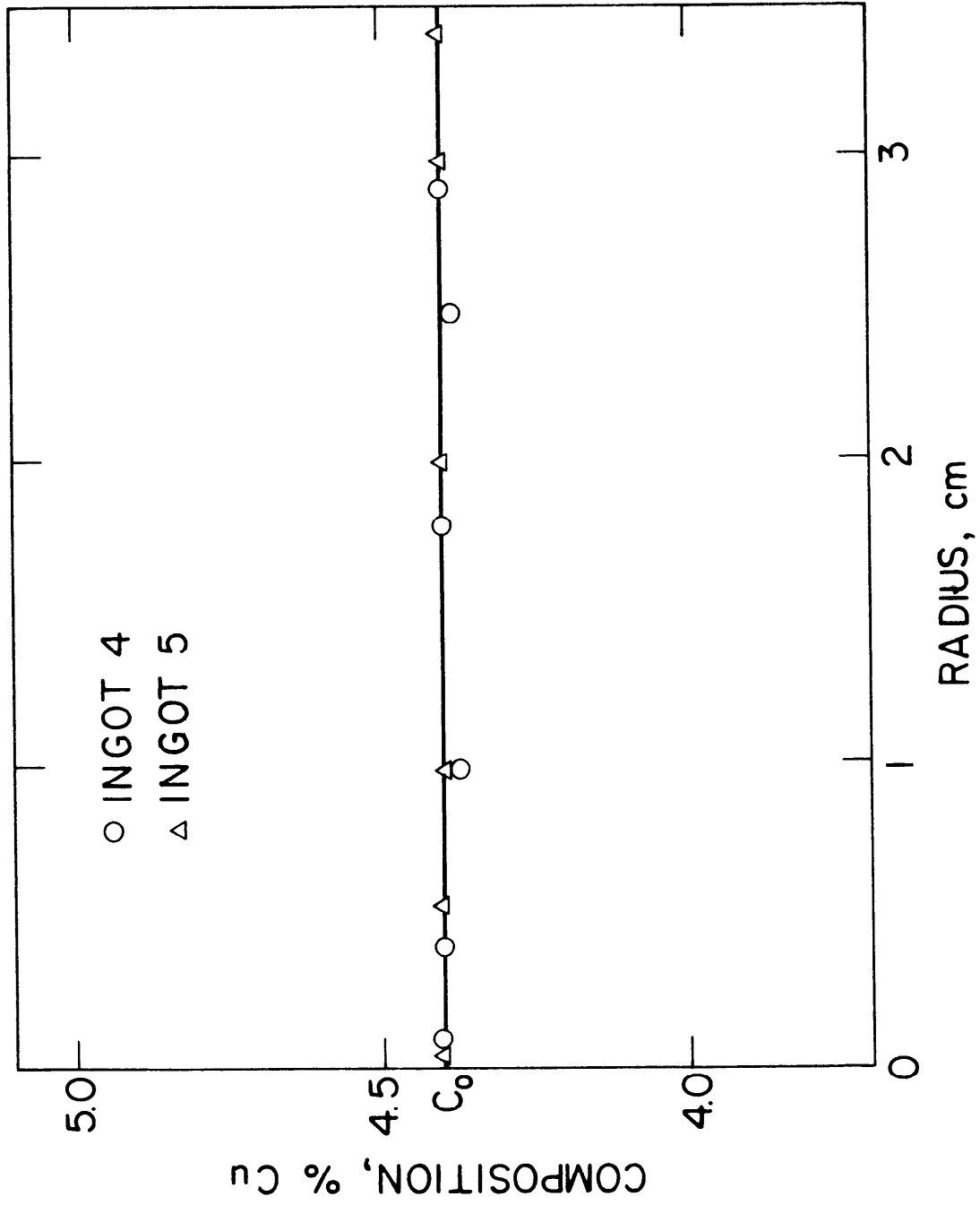
Figure 31: Uniform composition across ingots 4 and 5 (Al-4% Cu).
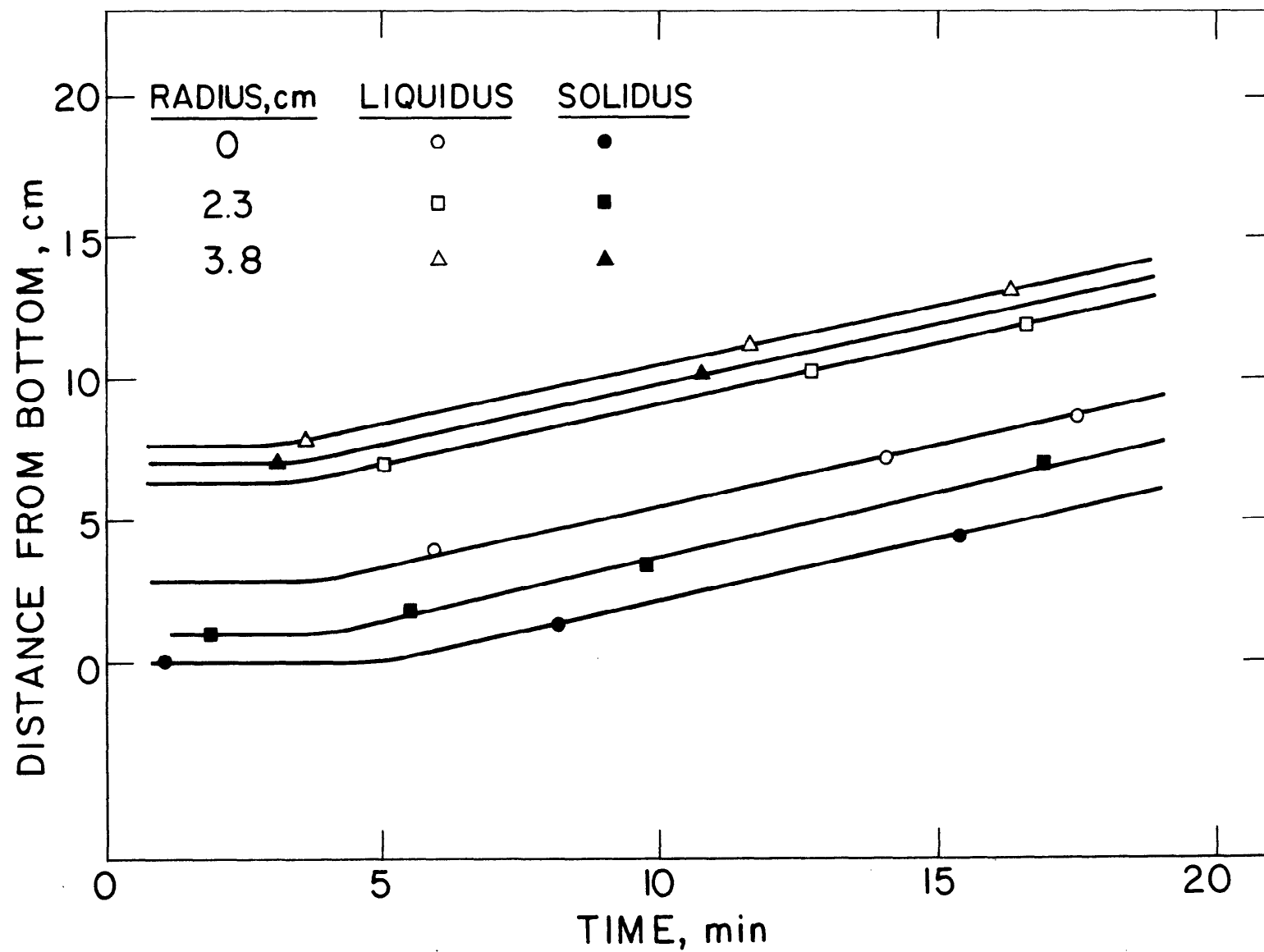
Figure 32:   Position of the liquidus and solidus isotherms in the Sn-15% Pb ingot.
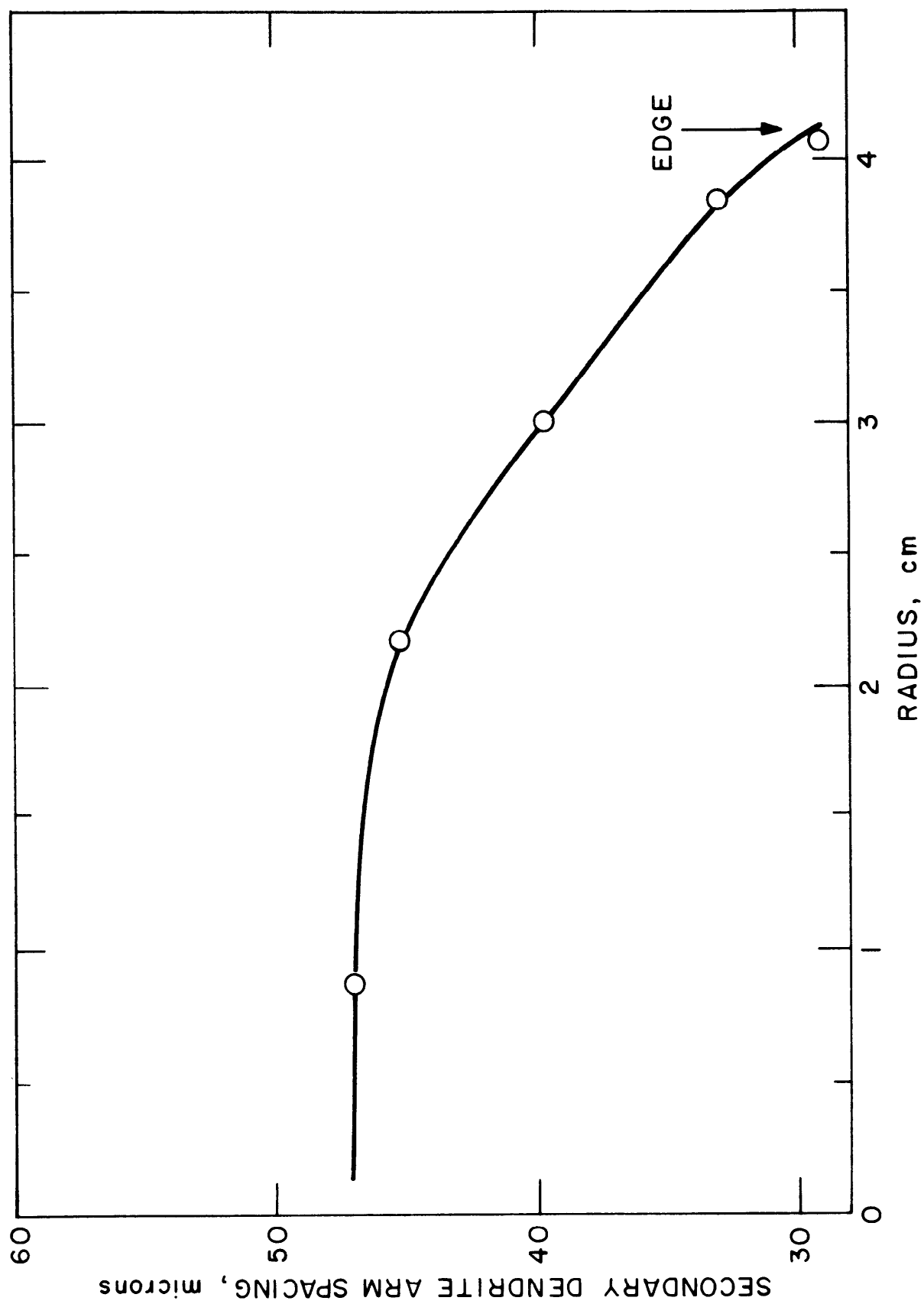
Figure 33: Secondary dendrite spacing in the Sn-15% Pb ingot.

VI. RESULTS OF COMPUTER SIMULATIONS

A. Al-4% Cu Ingots

Since ingot No. 1 exhibits the greatest degree of macrosegregation, we present results of calculations in detail for that ingot. Figures 34 and 35 are plots of pressure within the mushy zone calculated assuming that permeability varies with fraction liquid according to

$$K = \gamma g_L^2 \qquad (3)$$

In Figures 34, $\gamma = 2 \times 10^{-7}$ cm^2 and pressure increases as depth down within the mushy zone increases. If, however, permeability within the mushy zone is reduced by making $\gamma = 8 \times 10^{-8}$ cm^2, flow decreases in the lower portion of the mushy zone causing a decrease in pressure due to friction (Figure 35).

With the pressure distribution within the mushy zone, velocity is calculated according to Equation (7). It is of more interest, however, to examine values of $\vec{v} \cdot \nabla T / \varepsilon$ since this dimensionless group controls the extent of macrosegregation (see Equation (10)), and is also a measure of channel stability, i.e., "freckle" formation. Figure 36 shows that $\vec{v} \cdot \nabla T / \varepsilon$ is greater than zero so there should be no channels leading to "freckles" even when γ is made as great as 10^{-6} cm^2. In the central region of the ingot (Figure 36a) the effect of increasing γ is to reduce the value of $\vec{v} \cdot \nabla T / \varepsilon$ and to increase its value as the ingot radius is approached (Figures 36b and c). In terms of macrosegregation, this

effect is important because it determines whether segregation is positive or negative at ingot center or ingot radius.

Figure 37 summarizes results of calculations for values of γ ranging 10^{-6} to 10^{-8} cm^2. When $\gamma < 5 \times 10^{-7}$ cm^2 permeability is low and "shrinkage induced" flow predominates over "gravity induced" flow leading to negative segregation at ingot center and positive segregation at ingot radius. At $\gamma = 10^{-6}$ cm^2, permeability is high and "gravity induced" flow predominates causing the dense interdendritic liquid, rich in copper, to flow towards the ingot center thereby leading to positive segregation at the center and negative segregation at ingot radius.

Agreement between calculations and experiment for ingot 1 appears to be for $10^{-7} < \gamma < 5 \times 10^{-7}$ cm^2. This is much lower than the value of 3×10^{-9} to 9×10^{-9} cm^2 according to Figure 11, but secondary arm spacing is also significantly less (about 45 microns versus 200 microns).

Flow lines are shown in Figure 8 corresponding to $\gamma = 8 \times 10^{-8}$ cm^2. As expected, at this value of γ, "shrinkage induced" flow (towards the solidus isotherm) predominates, and there is no flow of copper-rich liquid towards ingot center; hence, segregation is negative at ingot center and positive at ingot radius.

In the central regions (r < 2 cm.), experimental results (Figure 37) follow the calculated curve for $\gamma = 5 \times 10^{-7}$ cm^2; towards the ingot radius (2 $\leq$ r < 3.4 cm.), there is better agreement with $\gamma = 10^{-7}$ cm^2 (Figure 37). Thus, it appears that the model is sufficiently well defined to predict, reasonably well, overall variation in segregation (i.e., whether segregation is positive or negative at ingot center and wall), but

is not sensitive enough to give exact agreement with experimental compositions across the entire ingot cross section.

A thin slice, 4 mm. thick, removed from across the ingot, was radiographed to see if the presence of porosity could account for difference between experimental results and calculations; no porosity was detected radiographically. At this time, it appears that there are two reasons for the discrepancy between calculated and experimental results. Permeability is probably not isotropic with respect to flow direction since the dendritic structure is not isotropic nor is γ uniform throughout, because dendrite arm spacing is not constant during solidification within the mushy zone. The second reason, and probably the more important of the two, is that bulk liquid convection influences flow within the mushy zone so that the boundary condition used – Equation (13) – does not precisely describe reality. With the limited knowledge of convection within liquid pools of ESR ingots, it would be difficult to describe this boundary condition precisely; it would be helpful, however, to examine the sensitivity of the model to various flow patterns imposed at the liquidus isotherm to make a judgment on the usefulness of Equation (13) as a boundary condition.

Using $\gamma = 10^{-7}$ cm^2, calculations indicate no segregation for ingot 2, as expected, since flow lines are vertical in unidirectional solidification. Calculations are also compared for ingots 3, 4, and 5 in Figure 38 assuming $\gamma = 10^{-7}$ cm^2. Again the model, using a single value of γ, does not predict precisely the exact segregation pattern (see Figures 29 and 31), but the model does predict less segregation in ingots

4 and 5 than in ingot 3 which is expected since solidification in ingots 4 and 5 more nearly approaches unidirectional solidification than does solidification in ingot 3 (Figure 30).

B. Sn-15% Pb Ingot

As in the case of Al-4% Cu ingots, agreement between experimental and calculated results is not precise, but the computer model does predict the overall segregation pattern, across an ingot, reasonably well. Figure 39 indicates that calculations using $\gamma = 10^{-6}$ cm^2 agree more closely with experimental results than when $\gamma = 5 \times 10^{-7}$ cm^2. On this basis alone, it appears that the permeability (at a given fraction liquid) is greater in Sn-15% Pb alloys than in Al-4% Cu alloys by about one order of magnitude. Measured values of permeability in lead rich Pb-Sn alloys are reported to be $10^1 - 10^2$ greater than the value of permeability reported for aluminum alloys[40,37]. Assuming similar behavior of tin-rich and lead-rich alloys, it is reasonable, therefore, to use $\gamma = 10^{-6}$ cm^2 in the Sn-15% Pb ingot contrasted to $\gamma = 10^{-7}$ cm^2 in the Al-4% Cu ingot.

In the Sn-15% Pb ingot, flow is extensive as indicated by the values of $\vec{v} \cdot \nabla T / \varepsilon$ shown in Figure 40. In most of the central region (Figure 40a), $\vec{v} \cdot \nabla T / \varepsilon$ is negative and drops below -1 for $r \lesssim 0.8$ cm. Away from the center (Figures 40b and c), $\vec{v} \cdot \nabla T / \varepsilon$ is sometimes negative but predominantly positive; it never drops below a value of -1. Figure 9 shows that in much of the ingot, interdendritic flow is from colder to hotter isotherms.

Obviously, in this ingot "gravity induced" flow predominates and consequently segregation is not only positive towards the center, but there is a high degree of channeling and copious freckling. To sum up, the analytical model predicts the occurrence of "freckles" which were also found in the experimental ingot of Sn-15% Pb alloy (Figure 7).

Work is currently underway to predict conditions necessary to avoid formation of "freckles" in ESR ingots, using the model alloy and the computer program together.
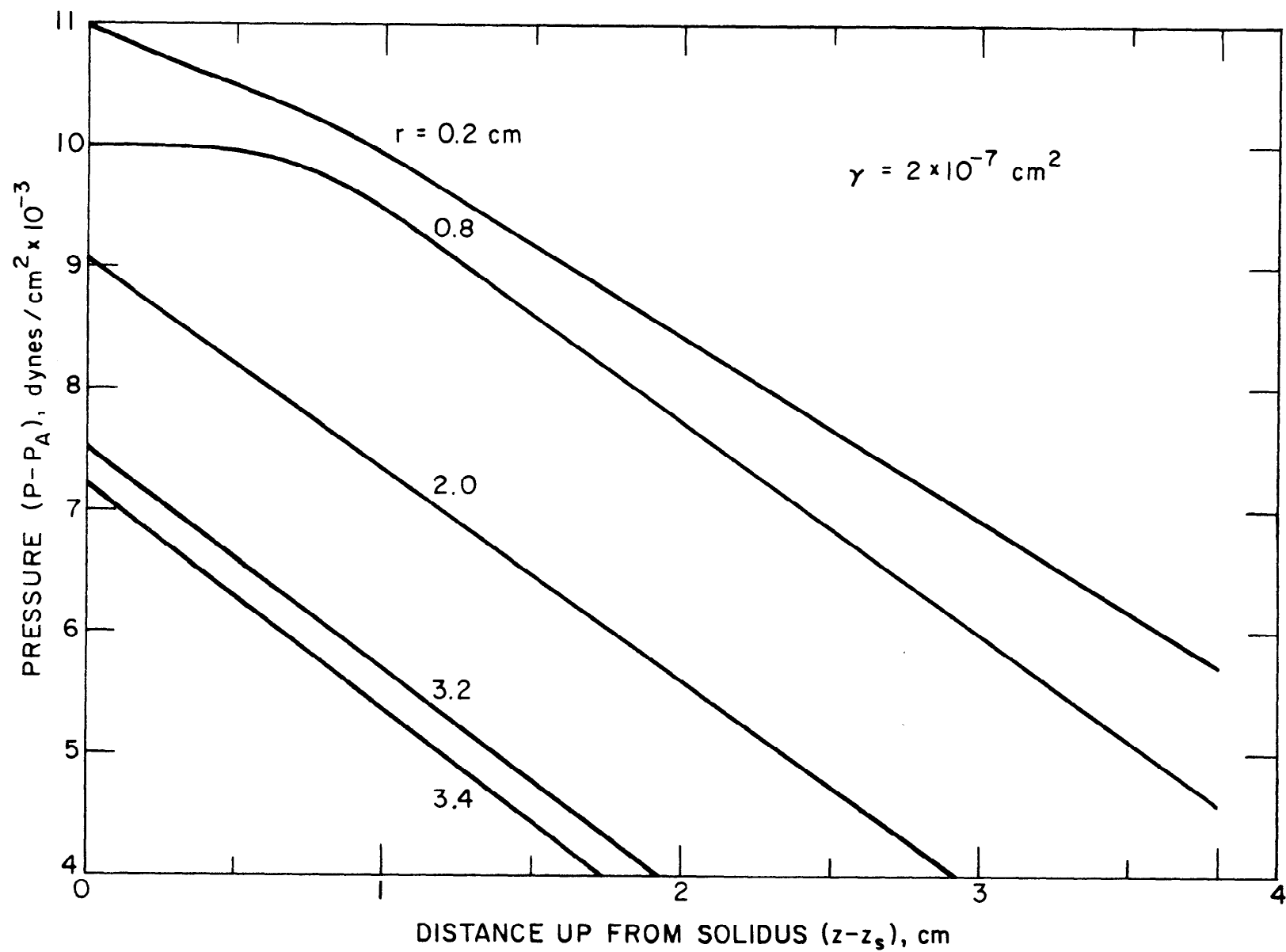
Figure 34: Pressure in ingot 1 calculated with $\gamma = 2 \times 10^{-7} \text{cm}^2$,
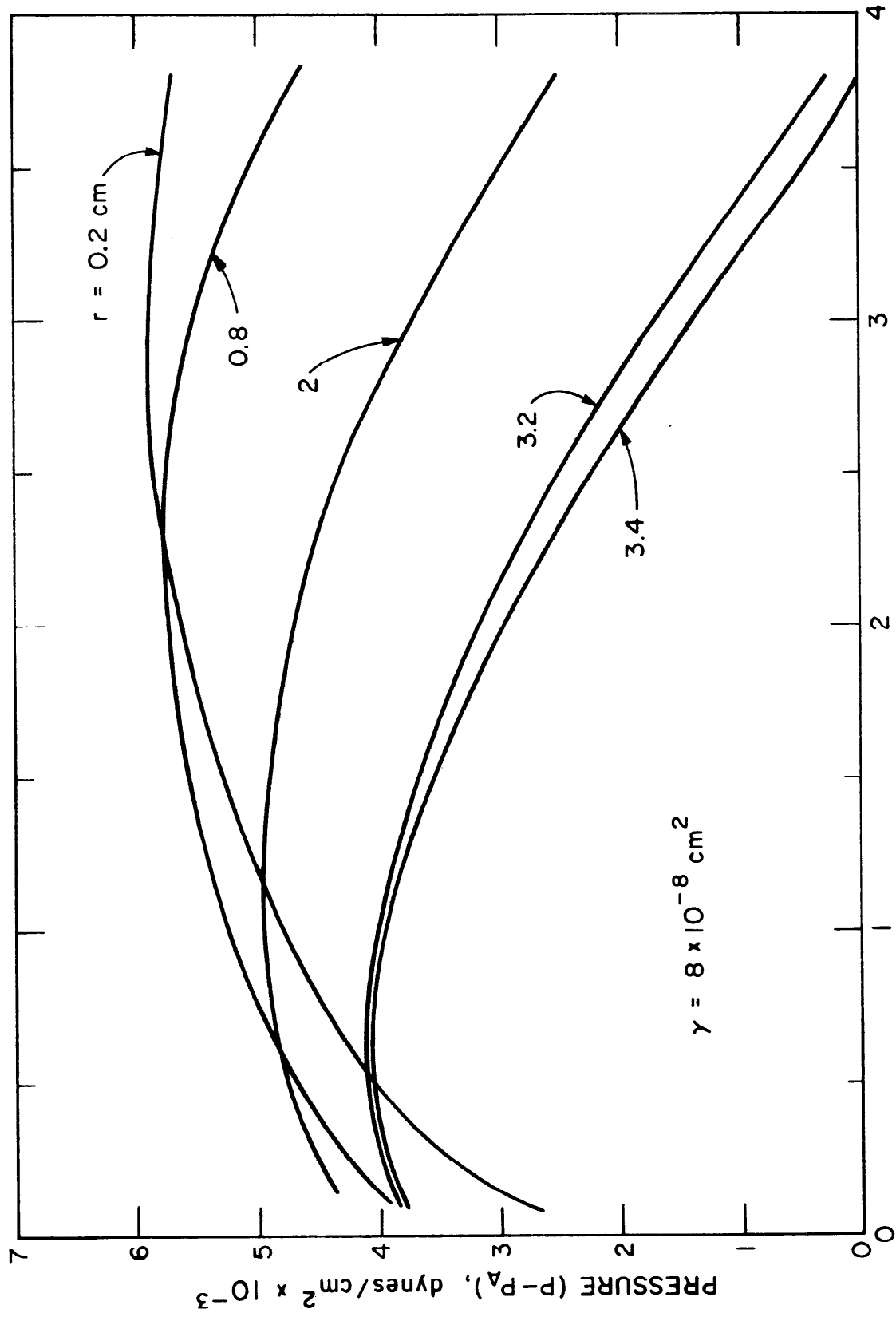
Figure 35: Pressure in ingot 1 calculated with $\gamma = 8 \times 10^{-8} cm^2$.
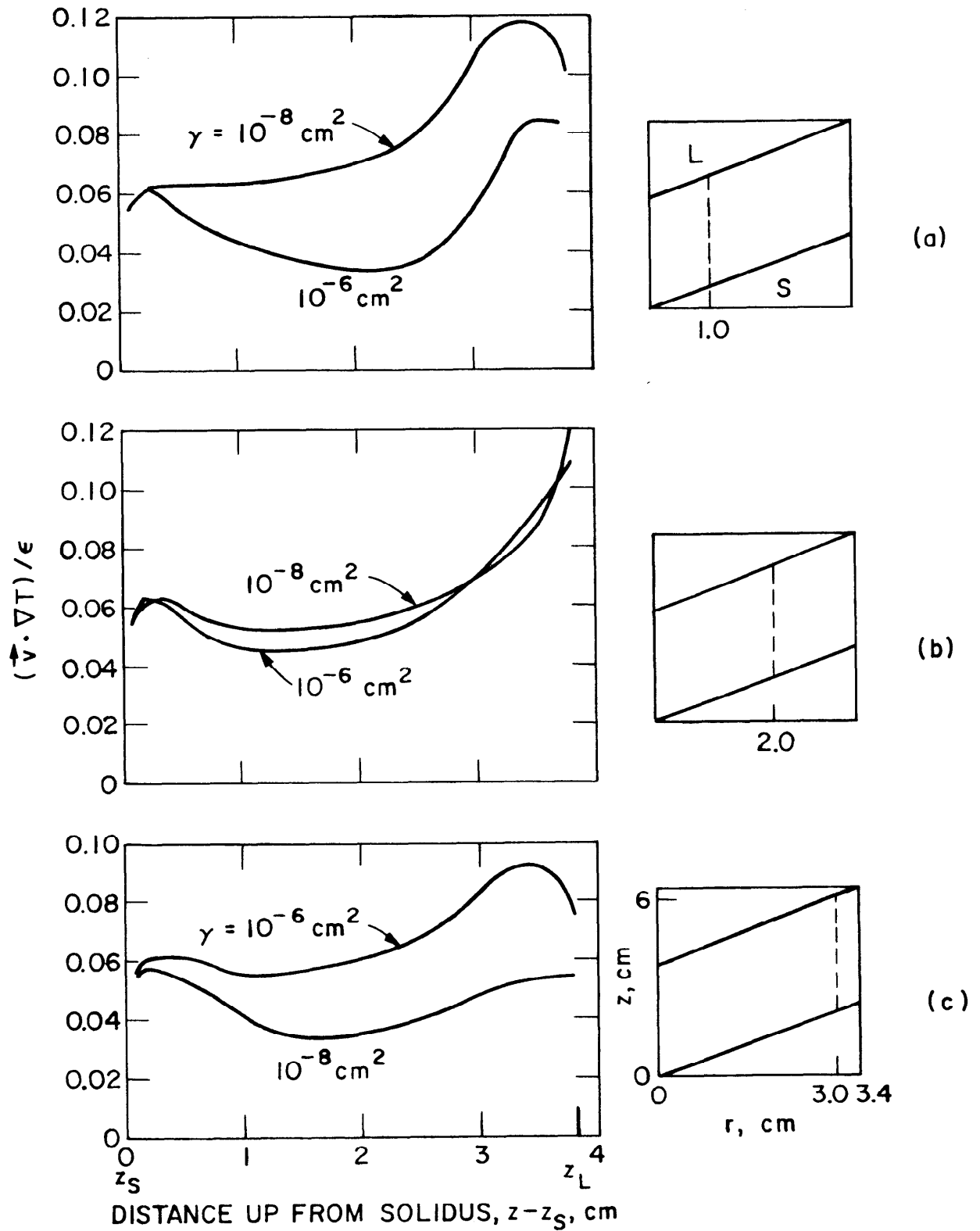
Figure 36: Calculated values of the dimensionless group $\vec{v}\cdot\nabla T/\varepsilon$ in ingot 1. (a) r = 1 cm; (b) r = 2 cm; (c) r = 3 cm.
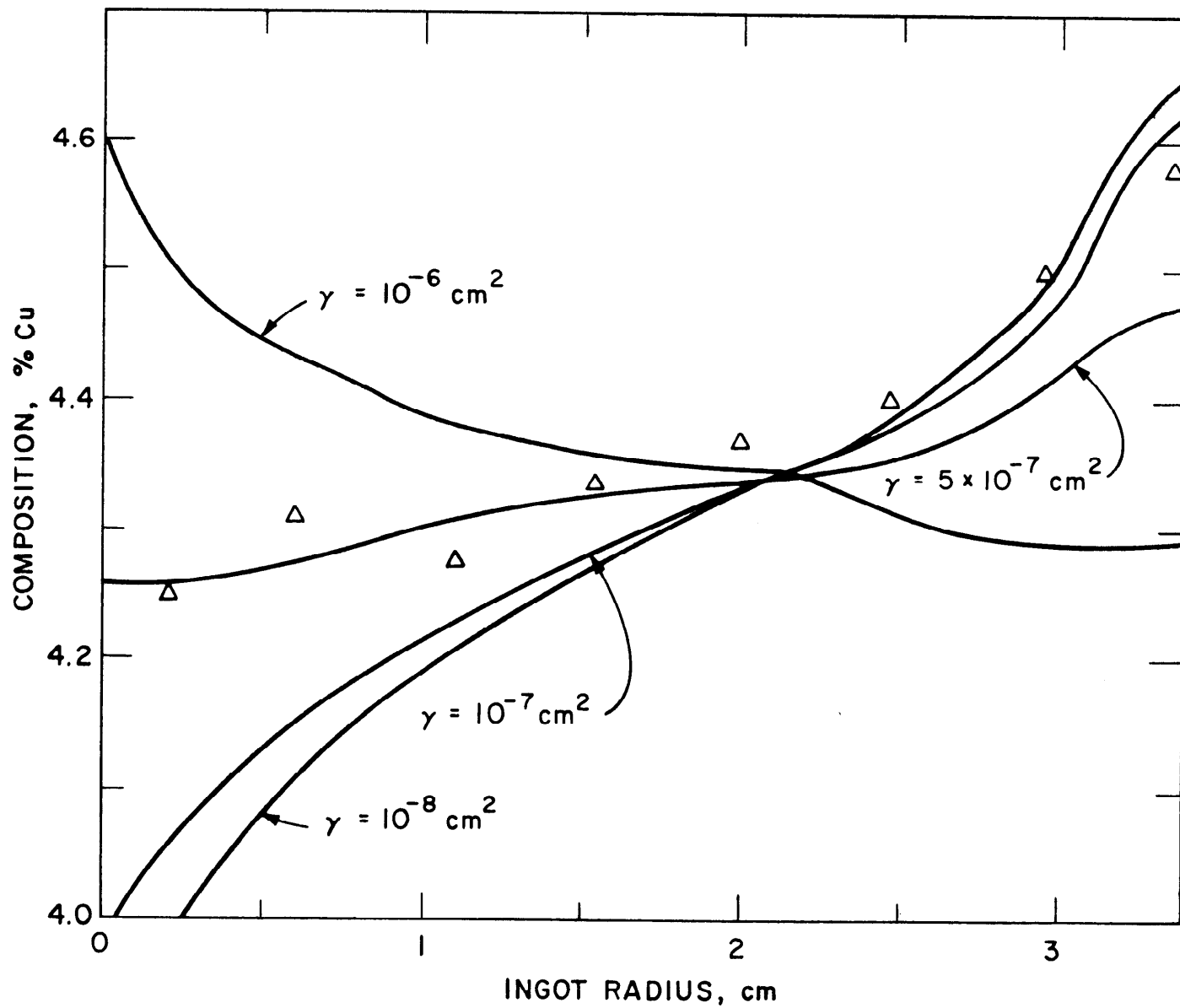
Figure 37: Calculation of segregation in ingot 1 for various values
of γ.
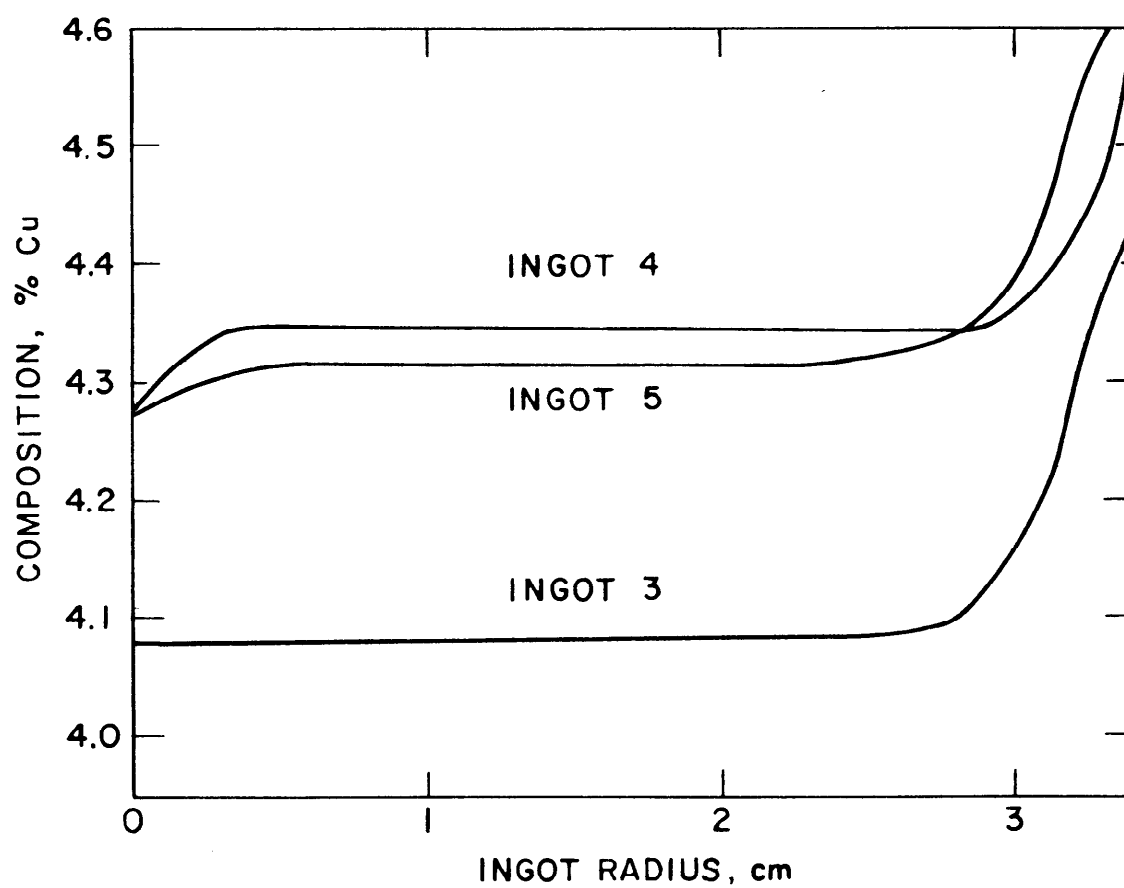
Figure 38: Calculations of segregation in ingots 3, 4, and 5 with $\gamma = 10^{-7}$ cm^2.
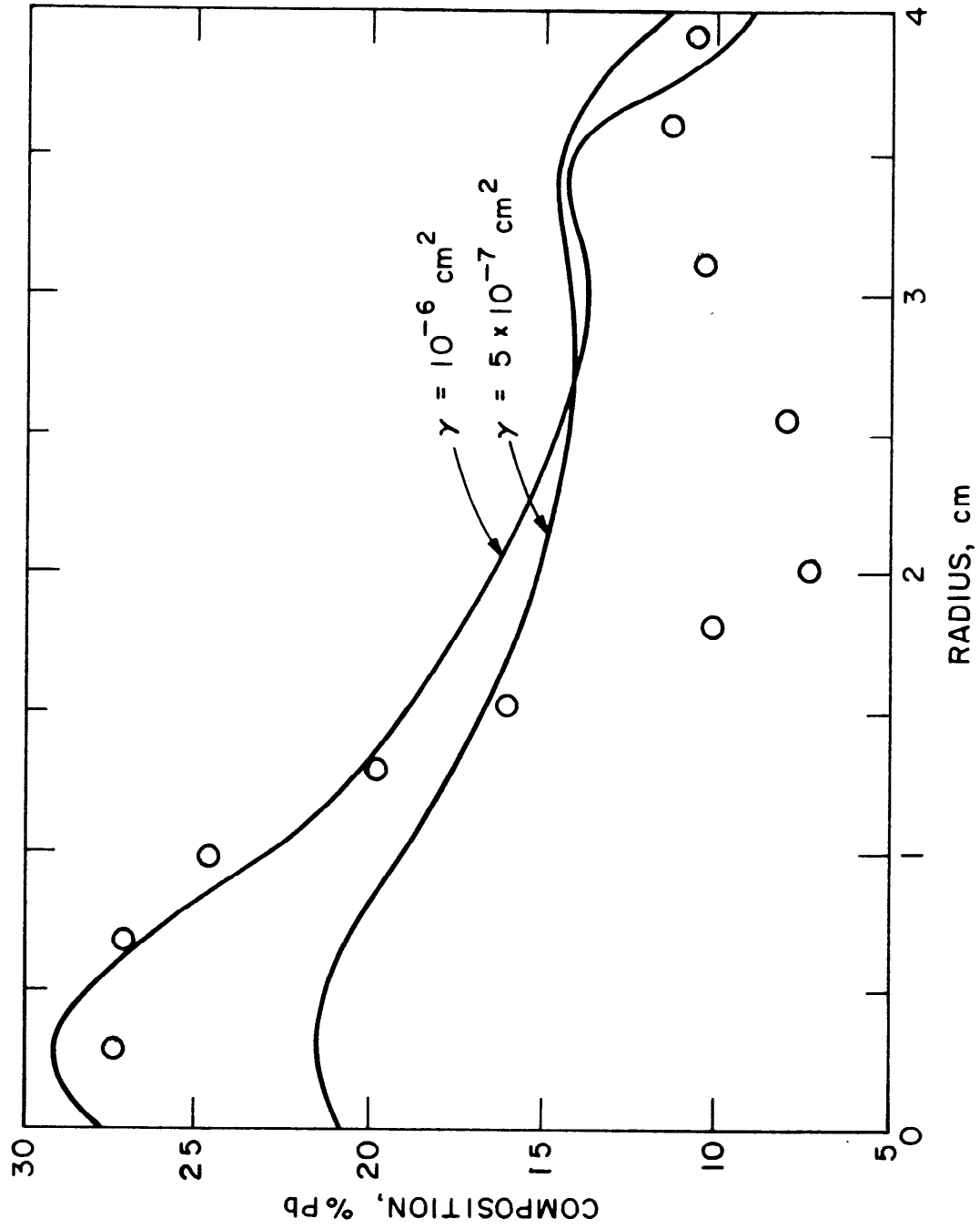
Figure 39: Calculation of segregation in the Sn-15% Pb ingot.
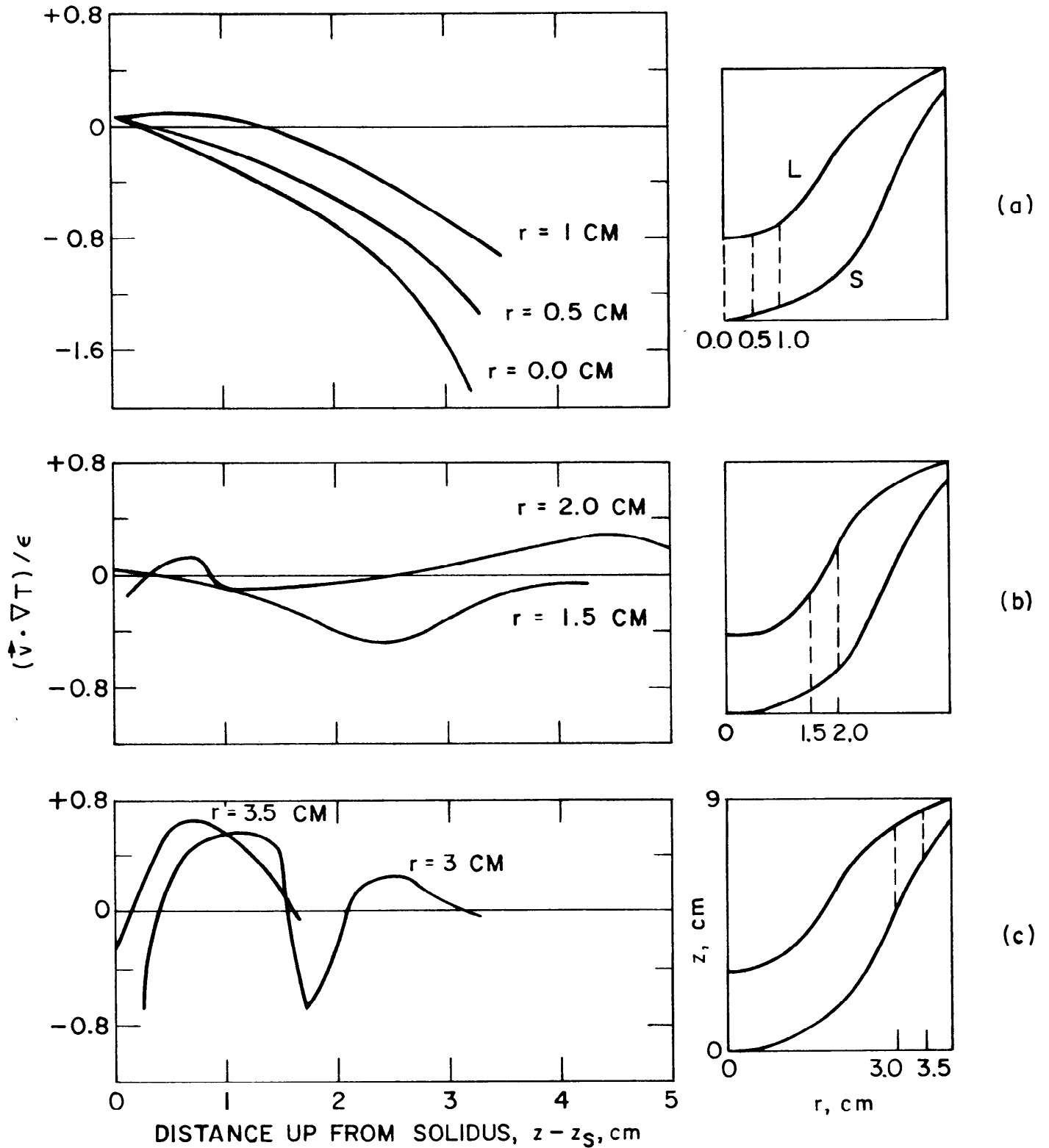
Figure 40: Calculated values of the dimensionless group $\vec{v}\cdot\nabla T/\varepsilon$ in the Sn-15% Pb ingot with $\gamma = 10^{-6}$ cm^2.

VII. CONCLUSIONS

1.   Severe macrosegregation in ESR ingots, such as "freckles" and
other "channel"-type segregates, as well as overall surface to
center variations in composition, can be produced and studied
using laboratory-scale apparatus.

2.   Calculations of macrosegregation, using a theoretical model, agree
well with experimental results considering the number of variables
involved. The model calculates surface to center variations in
composition using as input the temperature distribution within the
"mushy zone" of a solidifying ESR ingot. The model also predicts
the formation of "freckles" and "channel"-type segregates.

3.   Heat flow conditions which tend to make deeper isotherms within
the "mushy zone" accentuate segregation in ESR ingots. On the
other hand, in ingots with low cooling rates, permeability within
the partially solidified alloy is high (because dendrite arms are
more widely spaced), and interdendritic flow of solute-rich
liquid is extensive, leading to severe macrosegregation.

VIII. REFERENCES

1. M. C. Flemings, R. V. Barone, S. Z. Uram, H. F. Taylor, "Solidification of Steel Castings and Ingots", Trans. AFS, v. 69, 1961, pp. 422-435.

2. G. E. Nereo, R. F. Polich, M. C. Flemings, "Unidirectional Solidification of Steel Castings", Trans. AFS, v. 73, 1965, pp. 1-13.

3. R. F. Polich, M. C. Flemings, "Mechanical Properties of Unidirectional Steel Castings", Trans. AFS, v. 73, 1965, pp. 28-33.

4. T. Z. Kattamis, M. C. Flemings, "Dendrite Morphology, Microsegregation and Homogenization of Low Alloy Steel", Trans. Met. Soc. AIME, v. 233, 1965, pp. 992-999.

5. "Casting Process and Apparatus for Obtaining Unidirectional Solidification", Patent No. 3,204,301, M. C. Flemings, H. F. Taylor, October 24, 1960.

6. M. C. Flemings, "Directional Solidification and Composite Structures", Surfaces and Interface II, Ed. J. Burke et al., Syracuse University Press, 1968, pp. 313-352.

7. L. K. Bigelow, M. C. Flemings, "Sulfide Inclusions in Steel", U.S. Army Materials and Mechanics Research Center, Contract No. DAAG 46-68-C-0043, Report for the period January 1, 1968, to December 31, 1969.

8. M. Myers, M. C. Flemings, "Behavior of Silica Inclusions during Solidification of an Iron Base Alloy", U.S. Army Materials and Mechanics Research Center, Contract No. DAAG 46-68-C-0044, Final Report for the period January 1, 1968, to December 31, 1969.

9. D. S. Gnanamuthu, M. Basaran, T. Z. Kattamis, R. Mehrabian, M. C. Flemings, "Investigation of Solidification of High Strength Steel", U.S. Army Materials and Mechanics Research Center, Contract No. DAAG-46-68-C-0043, Report for the period January 1, 1970, to December 31, 1970.

10. D. S. Gnanamuthu, M. Basaran, T. Z. Kattamis, R. Mehrabian, M. C. Flemings, "Investigation of Solidification of High Strength Steel", U.S. Army Materials and Mechanics Research Center, Contract No. DAAG 46-68-C-0043, July, 1972.

11. E. F. Fascetta, T. Z. Kattamis, R. Mehrabian, M. C. Flemings, "Investigation of Solidification of High Strength Steel", U.S. Army Materials and Mechanics Research Center, Contract No. DAAG 46-68-C-0043, October, 1973.

12. M. Basaran, T. Z. Kattamis, R. Mehrabian, M. C. Flemings, "A Study of the Heat and Fluid Flow in Electroslag Remelting", U.S. Army Materials and Mechanics Research Center, Contract No. DAAG 46-73-C-0088, April, 1974.

13. M. C. Flemings, G. E. Nereo, "Macrosegregation, Part I", Trans. Met. Soc. AIME, v. 239, 1967, pp. 1449-1461.

14. M. C. Flemings, R. Mehrabian, G. E. Nereo, "Macrosegregation, Part II", Trans. Met. Soc. AIME, v. 242, 1968, pp. 41-49.

15. M. C. Flemings, G. E. Nereo, "Macrosegregation, Part III", Trans. Met. Soc. AIME, v. 242, 1968, pp. 50-55.

16. R. Mehrabian, M. C. Flemings, "Macrosegregation in Ternary Alloys", Met. Trans., v. 1, 1970, pp. 455-464.

17. R. Mehrabian, M. A. Keane, M. C. Flemings, "Interdendritic Fluid Flow and Macrosegregation; Influence of Gravity", Met. Trans., v. 1, 1970, pp. 1209-1220.

18. R. Mehrabian, M. A. Keane, M. C. Flemings, "Experiments on Macrosegregation and Freckle Formation", Met. Trans., v. 1, 1970, pp. 3238-3241.

19. M. A. Keane, Sc.D. Thesis, Department of Materials Science and Engineering, Massachusetts Institute of Technology, 1973.

20. E. Plokinger, "Electroslag Remelting - A Modern Tool in Metallurgy", J.I.S.I., August, 1973, pp. 533-541.

21. L. Cooper, "Central Zone Remelting of Ingots Using an Electroslag Process", Fifth International Symposium on ESR Process, Carnegie-Mellon University, Pittsburgh, October, 1974, pp. 202-238.

22. R. Schumann, C. Ellebrecht, "Metallurgical Process Problems Releated to ESR of Forging Ingot Larger than 40 Inch Diameter and 150 Inch Length in Single Electrode Technique", Fifth International Symposium on ESR Process, Carnegie-Mellon University, Pittsburgh, October, 1974, pp. 180-201.

23. H. Fredriksson, O. Jarleborg, "Solidification of ESR Ingots", J. of Metals, v. 23, September, 1971, p. 32.

24. R. J. McDonald, J. D. Hunt, "Fluid Motion through the Partial Solid Region of a Casting and Its Importance in Understanding 'A' Type Segregation", Trans. Met. Soc. AIME, v. 245, 1969, p. 1993.

25. Yu M. Mironov, M. M. Klyuev, "Some Features of the Solidification of Electroslag Ingots", Russian Metallurgy, No. 2, 1968, pp. 72-76.

26. M. A. Maulvault, "Temperature and Heat Flow in the Electroslag Remelting Process", Ph.D. Thesis, 1971, M.I.T., Department of Metallurgy and Materials Science.

27. R. C. Sun, J. W. Pridgeon, "Predicting Pool Shapes in a Laboratory Electroslag Remelting Process", Union Carbide Corporation, Materials System Division, Technology Department, Kokomo, Indiana, September, 1969, Report No. 7649.

28. A. Mitchell, S. Joshi, "The Thermal Characteristics of the Electroslag Process", Met. Trans., v. 4, 1973, pp. 631-642.

29. B. Z. Paton et al., "Calculation of Temperature Fields in Plate Ingots and in Ingot-Slabs of ESR", Fifth International Symposium on ESR Process, Carnegie-Mellon University, Pittsburgh, October, 1974, p. 323.

30. A. Mitchell, "Macrosegregation, Liquid Movement and Heat Flow in the ESR Process", Fourth International Symposium on Electroslag Remelting Process, Tokyo, Japan, June 7-8, 1973, p. 1.

31. F. W. Thomas, F. Knell, E. Weingartner, "Magnetic Field Effects in Vacuum ARC and Electroslag Remelting", Fifth International Symposium on ESR Process, Carnegie-Mellon University, Pittsburgh, October, 1974, p. 722.

32. D. J. Hebditch, J. D. Hunt, "Observations of Ingot Macrosegregation on Model Systems", Met. Trans., v. 5, 1974, p. 1557.

33. N. Streat, F. Weinberg, "Macrosegregation During Solidification Resulting from Density Differences in the Liquid", Met. Trans., v. 5, 1974, p. 2539.

34. S. M. Copley, A. F. Giamei, S. M. Johnson, M. F. Hornbecker, "The Origin of Freckles in Unidirectionally Solidified Castings", 69-028, Pratt & Whitney Aircraft, Middletown, Connecticut.

35. P. O. Mellberg and H. Sandberg, Scand. J. Metallurgy, v. 2, 1973, pp. 83-86.

36. R. Frost, private communication.

37. T. S. Piwonka, M. C. Flemings, "Pore Formation in Solidification", Trans. Met. Soc. AIME, v. 236, 1966, pp. 1157-1165.

38. D. Apelian, M. C. Flemings, R. Mehrabian, "Specific Permeability of Partially Solidified Networks of Al-Si Alloys", Met. Trans., v. 5, 1974, pp. 2533-2537.

39. G. H. Geiger, D. R. Poirier, _Transport Phenomena in Metallurgy_, Addison-Wesley, Reading, Mass. (1973), pp. 93-94.

40. N. Streat and F. Weinberg, "Interdendritic Fluid Flow in a Lead-Tin Alloy", Department of Metallurgy, University of British Columbia, Vancouver, B.C.

41. _Metals Handbook_, v. 8, A.S.M., 1973, p. 259.

42. _Metals Handbook_, v. 8, A.S.M., 1973, p. 330.

43. H. R. Thresh, A. F. Crawley, D. G. White, Trans. TMS-AIME, v. 242, 1968, p. 819.

44. H. J. Fisher, A. Phillips, Trans. TMS-AIME, v. 200, 1954, p. 1060.

45. J. A. Lee, G. V. Raynor, Proceedings of the Physical Society-London, v. 67B, 1954, p. 737.

46. C. Tyzack, G. V. Raynor, Acta Cryst., v. 7, 1954, p. 505.

47. M. C. Flemings, _Solidification Processing_, McGraw-Hill, New York, 1974, p. 142.

48. G. E. Nereo, Sc.D. Thesis, Department of Materials Science and Engineering, Massachusetts Institute of Technology, 1966.

49. M. C. Flemings, ibid., p. 150.

50. A. Grill, K. Sorimachi, J. K. Brimacombe, "Heat Flow, Gap Formation, and Break-outs in the Continuous Casting of Steel Slabs", Met. Trans. B, v. 7B, June, 1976, pp. 177-189.

APPENDIX A – ANALYSIS OF FLOW OF INTERDENDRITIC LIQUID

In analyzing the flow within the mushy zone, the volume element taken is large enough so that fraction solid within it is exactly the local average, but small enough so that it can be treated as a differential element. This is the typical differential volume element chosen in two-phase flow. For solidification problems it contains several dendrite arms. To analyze macrosegregation many of the details of solute redistribution on the microscale must be described. For dendritic freezing such as the model alloys selected for this study, we can assume the following[13,17]:

1. Liquid composition and temperature within the differential are uniform.

2. Equilibrium exists at the solid-liquid interface so that the equilibrium partition ratio, k, applies and $k = C_s^*/C_L$ where C_s^* and C_L are the compositions of the interface solid and liquid phases, respectively, and their values are from the equilibrium phase diagram at the temperature of the differential element.

3. Diffusion in the solid is negligible.

4. Only mass flow in or out of the differential element by convection is considered. Mass flow in or out of the differential element by diffusion in the liquid or mass input by flow of settling solid phase is neglected.

5. Density of solid, ρ_s, during solidification is constant. This is a very close approximation for Al-4% Cu and Sn-15% Pb systems used as model alloys herein.

6. No pore formation; i.e., $g_s + g_L = 1$ where g_s and g_L are volume fraction solid and liquid, respectively.

Conservation of mass within the differential element is

$$\frac{\partial}{\partial t} (\rho_s g_s + \rho_L g_L) = -\nabla \cdot \rho_L g_L \vec{v} \tag{20}$$

where t is time and $\vec{v}$ is velocity of the interdendritic liquid. With g_s plus $g_L = 1$ and ρ_s constant, Equation (20) becomes

$$(\rho_L - \rho_s) \frac{\partial g_L}{\partial t} + g_L \frac{\partial \rho_L}{\partial t} = -\nabla \cdot \rho_L g_L \vec{v} \tag{21}$$

In the mushy zone we apply D'Arcy's Law for flow through porous media. Therefore

$$\vec{v} = -\frac{K}{\mu g_L} (\nabla P + \rho_L \vec{g}) \tag{1}$$

where K is the permeability*, P is pressure, and μ is the liquid viscosity. A relationship of the form

$$K = \gamma g_L^2 \tag{3}$$

---

* K is actually the "specific permeability" as defined in Geiger and Poirier[39] but is called permeability in this report.

has been used by Mehrabian et al[17] to study macrosegregation based on the experimental work of Flemings and coworkers[37,38].

By substituting Equations (1) and (3) into Equation (21), we get

$$(\rho_L - \rho_s) \frac{\partial g_L}{\partial t} + g_L \frac{\partial \rho_L}{\partial t} = \nabla \cdot (\frac{\gamma g_L^2 \rho_L}{\mu} \nabla P + \frac{\gamma g_L^2 \rho_L^2}{\mu} \vec{g}) \qquad (22)$$

During dendritic solidification the interdendritic liquid is a function of temperature only, i.e., C_L versus T is given by the phase diagram. This follows from assumptions (1) and (2). Since C_L is a function of T only, we can write

$$\frac{\partial C_L}{\partial t} = (\frac{dC_L}{dT})(\frac{\partial T}{\partial t}) = \frac{\epsilon}{m} \qquad (23)$$

where m is the slope of the liquidus from the equilibrium phase diagram, and ϵ is the local cooling rate of the differential element.

Based upon the assumptions listed above, the "local solute redistribution equation" has been derived[13]. It gives volume fraction liquid as a function of the local composition of the interdendritic liquid (and hence, as a function of temperature during solidification); it is

$$\frac{\partial g_L}{\partial C_L} = - (\frac{1 - \beta}{1 - k})(1 + \frac{\vec{v} \cdot \nabla T}{\epsilon}) \frac{g_L}{C_L} \qquad (9)$$

From the chain rule, we have

$$\frac{\partial g_L}{\partial t} = (\frac{\partial g_L}{\partial C_L})(\frac{\partial C_L}{\partial t}) \qquad (24)$$

and by substituting Equations (23) and (9) into Equation (24), we get

$$\frac{\partial g_L}{\partial t} = - (\frac{1-\beta}{1-k})(1 + \frac{\vec{v}\cdot\nabla T}{\epsilon}) \frac{g_L}{C_L} \frac{\epsilon}{m} \qquad (25)$$

The density of the interdendritic liquid, ρ_L, is a function of concentration and temperature. But since $C_L = f(T)$, then ρ_L is a function of C_L only (Figures 13b and 14b). Therefore,

$$\frac{\partial \rho_L}{\partial t} = (\frac{d\rho_L}{dC_L})(\frac{\partial C_L}{\partial t}) \qquad (26)$$

where $(d\rho_L/dC_L)$ is the slope of a plot of ρ_L versus C_L.

By substituting Equations (25) and (26) into Equation (22), and applying D'Arcy's Law, we get

$$\nabla \cdot (\frac{\gamma g_L^2 \rho_L}{\mu} \nabla P + \frac{\gamma g_L^2 \rho_L^2}{\mu} \vec{g}) =$$

$$- (\rho_L - \rho_s)(\frac{1-\beta}{1-k})[1 - \frac{\gamma g_L}{\mu\epsilon} (\nabla P + \rho_L\vec{g}) \cdot \nabla T] \frac{g_L}{C_L} \frac{\epsilon}{m}$$

$$+ g_L \frac{d\rho_L}{dC_L} \frac{\epsilon}{m} . \qquad (27)$$

Equation (27) can be solved along with appropriate boundary conditions to give pressure within the mushy zone of a solidifying ingot. For application to our analytical model - specifically for cylindrical ESR ingots - we expand Equation (27) into cylindrical coordinates (z,r), and use

$$\frac{\partial^2 P}{\partial r^2} + A \frac{\partial P}{\partial r} + \frac{\partial^2 P}{\partial z^2} + B \frac{\partial P}{\partial z} + C = 0 \quad , \tag{10}$$

where

$$A = \frac{1}{r} + \frac{2}{g_L} \frac{\partial g_L}{\partial r} + \frac{1}{\rho_L} \frac{\partial \rho_L}{\partial r} + \alpha \frac{\partial C_L}{\partial r} \quad ,$$

$$B = \frac{2}{g_L} \frac{\partial g_L}{\partial z} + \frac{1}{\rho_L} \frac{\partial \rho_L}{\partial z} + \alpha \frac{\partial C_L}{\partial z} \quad ,$$

$$C = g\rho_L \left[\frac{2}{g_L} \frac{\partial g_L}{\partial z} + \frac{2}{\rho_L} \frac{\partial \rho_L}{\partial z} + \alpha \frac{\partial C_L}{\partial z} \right] - \frac{\varepsilon\mu}{m\gamma g_L}\left[\alpha + \frac{1}{\rho_L} \frac{d\rho_L}{dC_L}\right]$$

and

$$\alpha = \frac{\beta}{(1 - k)C_L} \quad .$$

APPENDIX B – METHOD OF SOLUTION

1. Finite Difference Approximations

Equation (10), along with the boundary conditions, Equations (11) – (14), are solved using a computer program based on finite difference approximations of the derivatives.

Interior Nodes

Figure 41a depicts an interior node within the mushy zone at a pressure P_0 surrounded by four nodes at pressures P_1, P_2, P_3, and P_4. Node spacing in the r-direction is $\Delta r = h$ and in the z-direction is $\Delta z = k$. The finite difference approximations for the pressure derivatives are

$$\frac{\partial P}{\partial r} \simeq \frac{1}{2} \left(\frac{P_2 - P_0}{h} - \frac{P_0 - P_4}{h} \right) = \frac{P_2 - P_4}{2h} \quad ; \quad (28)$$

similarly

$$\frac{\partial P}{\partial z} \simeq \frac{P_1 - P_3}{2k} \quad ; \quad (29)$$

also

$$\frac{\partial}{\partial r} \left(\frac{\partial P}{\partial r} \right) \simeq \frac{1}{h} \left(\frac{P_2 - P_0}{h} - \frac{P_0 - P_4}{h} \right) = \frac{P_2 + 2P_0 + P_4}{h^2} \quad , \quad (30)$$

and

$$\frac{\partial}{\partial z} \left(\frac{\partial P}{\partial z} \right) \simeq \frac{P_1 - 2P_0 + P_3}{k^2} \quad . \quad (31)$$

The coefficients A, B, and C are evaluated by assigning a temperature at each node, thus determining C_L, ρ_L, α, μ, ε, and $(d\rho_L/dC_L)$. To initiate calculations, values of g_L at each node are approximated by the Scheil equation (i.e., Equation (9) with $\vec{v} = 0$ and $\beta = 0$); by an iteration technique, values of g_L are "updated" as calculations proceed.

Boundary Nodes Along the Liquidus

The liquidus isotherm does not necessarily pass through the location of nodal points so "boundary nodes" are defined by determining the node (above or below the isotherm) which is closer to the isotherm. That node is then considered to be a "boundary node". Specifically in Figure 41b, the boundary nodes are 2, 3, and 6 because they are closer to the liquidus isotherm than nodes 1, 4, and 5, respectively.

The assumption of no convection in the liquid pool is made so that the pressure along the liquidus is given by the metallostatic head above the liquidus. Thus, taking node 3 as example,

$$P_3 = P_a + \rho_{L0} g \ell \tag{33}$$

where P_a is the pressure at the top of the liquid pool (1 atmosphere is used in our calculations), ℓ is the height of liquid metal above node 3 and ρ_{L0} is the density of the liquid metal pool.

If the liquidus isotherm is steep enough, then locating "boundary nodes" is done by deciding which of two nodes at a given z-value is the closer rather than deciding which of two nodes at a given r-value is

closer as depicted above. Obviously as the grid spacing decreases, then the positions of the "boundary nodes" more nearly approximate the liquidus isotherm. For ingot 1, calculations were done with k = 0.1 cm and h = 0.2 cm; in ingot 2, k = 0.2 cm and h = 0.2 cm. In ingots 3, 4, and 5 k = 0.03 cm and h = 0.2 cm. Calculations using k = 0.14 cm and h = 0.25 cm were made for the Sn-15% Pb ingot.

Boundary Nodes Along the Solidus

At the solidus isotherm, alloy solidification is completed by eutectic liquid solidifying to form eutectic solid of the same composition. If no pores form, then the flow of interdendritic liquid must equal the rate at which the solidifying eutectic liquid is shrinking. Hence,

$$\vec{v} = - \left(\frac{\rho_{SE} - \rho_{LE}}{\rho_{LE}}\right) \vec{U}_E \tag{14}$$

where $\vec{U}_E$ is the eutectic isotherm velocity normal to the isotherm. The components of Equation (14) are

$$v_r = - \left(\frac{\rho_{SE} - \rho_{LE}}{\rho_{LE}}\right) U_r \tag{33}$$

and

$$v_z = - \left(\frac{\rho_{SE} - \rho_{LE}}{\rho_{LE}}\right) U_z \tag{34}$$

Equations (33) and (34) are in terms of velocity; it is necessary to transform them into statements which describe pressure gradient along the boundary. This is done by using the components of D'Arcy's equation, Equation (1), with $\rho_L = \rho_{LE}$ and $g_L = g_{LE}$, as follows:

$$v_r = -\frac{K}{\mu g_{LE}} \frac{\partial P}{\partial r} \tag{35}$$

and

$$v_z = -\frac{K}{\mu g_{LE}} \left(\frac{\partial P}{\partial z} - \rho_{LE} g \right) . \tag{36}$$

By combining Equations (33) and (35) and Equations (34) and (36), we express the components of the pressure gradient at the solidus isotherm.

$$\frac{\partial P}{\partial r} = \left(\frac{\mu g_{LE}}{K} \right) \left(\frac{\rho_{SE} - \rho_{LE}}{\rho_{LE}} \right) U_r \tag{37}$$

and

$$\frac{\partial P}{\partial z} = \left(\frac{\mu g_{LE}}{K} \right) \left(\frac{\rho_{SE} - \rho_{LE}}{\rho_{LE}} \right) U_z + \rho_{LE} g . \tag{38}$$

To formulate these pressure gradients into the finite-difference computer program, we must first locate the "boundary nodes" along the solidus in a manner similar to locating "boundary nodes" for the liquidus. Figure 41c shows a group of nodes in the vicinity of the solidus isotherm. The "boundary nodes" are selected by deciding if P_5' is closer to the isotherm than is P_5, P_3 closer than P_3', and P_2' closer than P_2. In this example, P_5', P_3, and P_2' are selected as "boundary nodes". Then the finite difference approximations for Equation (10) are applied to each

node directly above the "boundary nodes". Node P_0 is such a node. The derivatives appropriately take into account the components of pressure gradient at the solidus (Equations (37) and (38)). These derivatives, in finite difference form, the

$$\frac{\partial P}{\partial r} \simeq \frac{1}{2} \left(\frac{P_2 - P_0}{h} + \frac{P_0 - P_4}{h} \right) = \frac{P_2 - P_4}{2h} \quad , \qquad (39)$$

$$\frac{\partial}{\partial r} \left(\frac{\partial P}{\partial r} \right) \simeq \frac{P_2 + 2P_0 + P_4}{h^2} \quad , \qquad (40)$$

$$\frac{\partial P}{\partial z} \simeq \frac{1}{2} \left(\frac{P_1 - P_0}{k} + \frac{P_0 - P_3}{k} \right) \quad , \qquad (41)$$

and

$$\frac{\partial}{\partial z} \left(\frac{\partial P}{\partial z} \right) \simeq \frac{1}{k} \left(\frac{P_1 - P_0}{k} - \frac{P_0 - P_3}{k} \right) \quad . \qquad (42)$$

This is all done in the same manner as for an interior nodes, except now we use Equation (38) and write

$$\frac{P_0 - P_3}{k} \simeq \left(\frac{\mu g_{LE}}{K} \right) \left(\frac{\rho_{SE} - \rho_{LE}}{\rho_{LE}} \right) U_z + \rho_{LE} g \qquad (43)$$

Equation (43) is substituted into Equations (41) and (42) to obtain the z-derivates for node "0". In assembling the program, therefore, there is an equation for each of the nodes just above each "boundary nodes". There are no equations for the "boundary nodes", per se.

If the solidus isotherm is steep, then "boundary nodes" are selected by choosing the closer node to the left or right of the isotherm.

Then derivatives in the r-direction are modified and Equation (37) is invoked in a manner similar to that described above for Equation (38).

Boundary Nodes at the Centerline and Ingot Radius

By symmetry, $v_r = 0$ or $\partial P/\partial r = 0$ at the centerline. At ingot radius, $v_r = 0$ so along this boundary $\partial P/\partial r = 0$ also. These boundary conditions are incorporated into the computer program by merely setting pressure at the centerline nodes equal to the pressure of the nodes directly connected to the centerline nodes. Similarly, the pressure at a node along the ingot radius is set equal to its connecting node.

2. Computer Program

When approximating equations are written for all of the interior and boundary nodes, there results a set of n equations which must be solved for n unknown values of pressure. Since n is in the range of 500 - 1000, the set of equations are not solved directly, but rather an iteration scheme is used. Figure 15 is a flow chart of the computer code. First pressure at all nodes is approximated by merely calculating pressure due to metallostatic pressure. Then, node by node, the computer code is directed to solve for nodal pressures using the "first guess" pressures at connecting nodes; then "second guess" values of pressure are calculated and assigned to every node. Then the entire process is repeated 200 times (value of MAXIT).

For the first 200 iterations, the volume fraction liquid at each node is that calculated by the Scheil equation corresponding to the nodal temperature. In Figure 15 this brings us to step 7.

With pressure distribution in the mushy zone calculated, velocity components at all nodes can then be calculated by using D'Arcy's Law – Equation (1) – which relates velocity to pressure gradient. The "local solute redistribution equation" – Equation (9) – is then integrated, node by node, down a given column from the liquidus to the solidus in order to obtain updated values of g_L. Equation (15) is solved to obtain local average composition. With these updated values of g_L (step 8 in Figure 15), pressure is recalculated for 200 more iterations (MAXIT=400), bringing the total iterations up to 400 when a new set of g_L values are obtained. The process is repeated for another 200 iterations.

A total of 600 iterations was selected because a trial run showed that from 500 to 700 iterations only a negligible change in local average compositions was noted when the computer code was used to simulate macrosegregation in ingot 1.
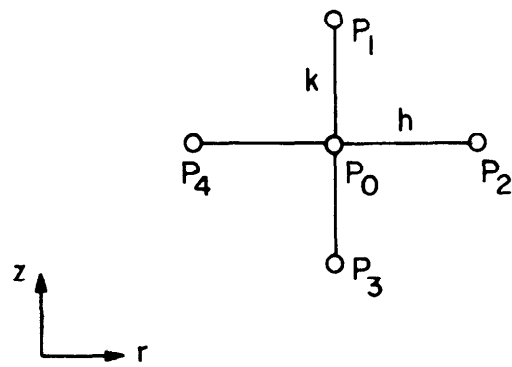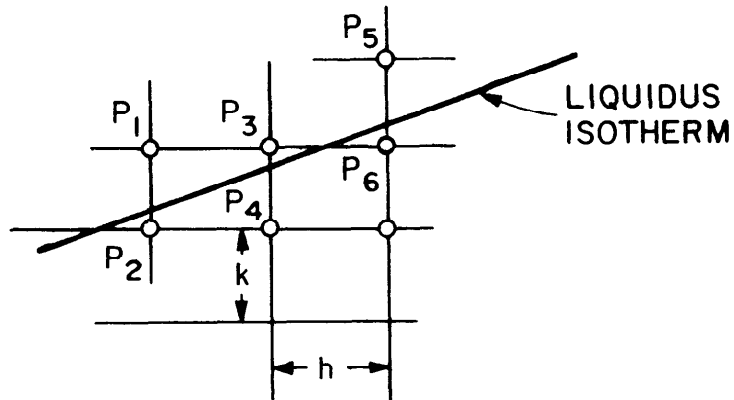
Figure 41: Nodes used in the finite difference approximations of pressure within the mushy zone: (a) interior nodes; (b) the nodes at the liquidus isotherm; (c) nodes at the solidus isotherm.
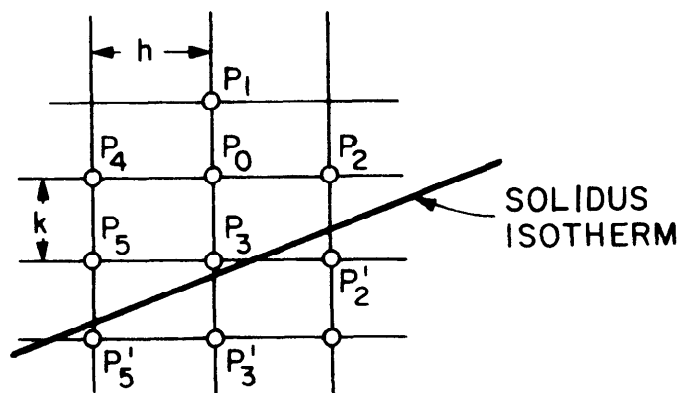
DISTRIBUTION LIST

No. of Copies	To

1   Office of the Director, Defense Research and Engineering, The Pentagon,
Washington, D. C. 20301

12 Commander, Defense Documentation Center, Cameron Station, Building 5,
5010 Duke Street, Alexandria, Virginia 22314

1   Metals and Ceramics Information Center, Battelle Columbus Laboratories,
505 King Avenue, Columbus, Ohio 43201

    Chief of Research and Development, Department of the Army,
Washington, D. C. 20310
2   ATTN: Physical and Engineering Sciences Division

    Commander, Army Research Office, P. O. Box 12211, Research
Triangle Park, North Carolina 27709
1   ATTN: Information Processing Office

    Commander, U. S. Army Materiel Development and Readiness Command,
5001 Eisenhower Avenue, Alexandria, Virginia 22333
1   ATTN: DRCDE-TC
1   DRCSA-S, Dr. R. B. Dillaway, Chief Scientist

    Commander, U. S. Army Electronics Command, Fort Monmouth, New Jersey 07703
1   ATTN: DRSEL-GG-DD
1   DRSEL-GG-DM
1   DRSEL-GG-E
1   DRSEL-GG-EA
1   DRSEL-GG-ES
1   DRSEL-GG-EG

    Commander, U. S. Army Missile Command, Redstone Arsenal, Alabama 35809
1   ATTN: Technical Library
1   DRSMI-RSM, Mr. E. J. Wheelahan

    Commander, U. S. Army Armament Command, Rock Island, Illinois 61201
2   ATTN: Technical Library

    Commander, U. S. Army Natick Research and Development Command,
Natick, Massachusetts 01760
1   ATTN: Technical Library
1   Dr. E. W. Ross
1   DRXNM-AAP, Mr. J. Falcone

    Commander, U. S. Army Satellite Communications Agency,
Fort Monmouth, New Jersey 07703
1   ATTN: Technical Document Center

Commander, U. S. Army Tank-Automotive Research and Development Command, Warren, Michigan 48090
1 ATTN: DRDTA-R
2   DRDTA, Research Library Branch

Commander, White Sands Missile Range, New Mexico 88002
1 ATTN: STEWS-WS-VT

Commander, Aberdeen Proving Ground, Maryland 21005
1 ATTN: STEAP-TL, Bldg. 305

Commander, Edgewood Arsenal, Aberdeen Proving Ground, Maryland 21010
1 ATTN: Mr. F. E. Thompson, Dir. of Eng. & Ind. Serv., Chem-Mun Br

Commander, Frankford Arsenal, Philadelphia, Pennsylvania 19137
1 ATTN: Library, H1300, Bl. 51-2
1   SARFA-L300, Mr. J. Corrie

Commander, U. S. Army Ballistic Research Laboratory, Aberdeen Proving Ground, Maryland 21005
1 ATTN: Dr. J. Frasier
1   Dr. R. Vitali
1   Dr. G. L. Filbey
1   Dr. R. Karpp
1   Dr. W. Gillich

Commander, Harry Diamond Laboratories, 2800 Powder Mill Road, Adelphi, Maryland 20783
1 ATTN: Technical Information Office

Commander, Picatinny Arsenal, Dover, New Jersey 07801
1 ATTN: SARPA-RT-S
1   Mr. A. Devine
1   SARPA-FR-M-D, PLASTEC, A. M. Anzalone

Commander, Redstone Scientific Information Center, U. S. Army Missile Command, Redstone Arsenal, Alabama 35809
4 ATTN: DRSMI-RBLD, Document Section

Commander, Watervliet Arsenal, Watervliet, New York 12189
1 ATTN: SARWV-RDT, Technical Information Services Office
1   Dr. T. Davidson
1   Mr. D. P. Kendall
1   Mr. J. F. Throop
1   SARWV-RDR, Dr. F. W. Schmiedeshoff

Commander, U. S. Army Foreign Science and Technology Center, 220 7th Street, N. E., Charlottesville, Virginia 22901
1 ATTN: DRXST-SD2

Commander, U. S. Army Aeromedical Research Unit, P. O. Box 577,
Fort Rucker, Alabama 36460
1 ATTN: Technical Library

Director, Eustis Directorate, U. S. Army Air Mobility Research and
Development Laboratory, Fort Eustis, Virginia 23604
1 ATTN: Mr. J. Robinson, SAVDL-EU-SS
1   Mr. R. Berresford

Librarian, U. S. Army Aviation School Library, Fort Rucker, Alabama 36360
1 ATTN: Building 5907

Commander, U. S. Army Board for Aviation Accident Research,
Fort Rucker, Alabama 36360
1 ATTN: Library, Building 5505

Commander, USACDC Air Defense Agency, Fort Bliss, Texas 79916
1 ATTN: Technical Library

Commander, U. S. Army Engineer School, Fort Belvoir, Virginia 22060
1 ATTN: Library

Commander, U. S. Army Engineer Waterways Experiment Station,
Vicksburg, Mississippi 39180
1 ATTN: Research Center Library

Aeronautic Structures Laboratories, Naval Air Engineering Center,
Philadelphia, Pennsylvania 19112
1 ATTN: Library

Naval Air Development Center, Aero Materials Department,
Warminster, Pennsylvania 18974
1 ATTN: J. Viglione

Naval Ship Research and Development Laboratory, Annapolis, Maryland 21402
1 ATTN: Dr. H. P. Chu

Naval Underwater Systems Center, New London, Connecticut 06320
1 ATTN: R. Kasper

Naval Research Laboratory, Washington, D. C. 20375
1 ATTN: C. D. Beachem
1   Dr. J. M. Krafft - Code 8430

Chief of Naval Research, Arlington, Virginia 22217
1 ATTN: Code 471

Naval Weapons Laboratory, Washington, D. C. 20390
1   ATTN: H. W. Romine

Director, Structural Mechanics Research, Office of Naval Research,
800 North Quincy Street, Arlington, Virginia 22203
1   ATTN: Dr. N. Perrone

1   Ship Structure Committee, Maritime Transportation Research Board,
    National Research Council, 2101 Constitution Avenue, N. W.,
    Washington, D. C. 20418

Air Force Materials Laboratory, Wright-Patterson Air Force Base, Ohio 45433
2   ATTN: AFML/MXE/E. Morrissey
1   AFML/LC
1   AFML/LLP/D. M. Forney, Jr.
1   AFML/MBC/Mr. Stanley Schulman
1   AFML/LNC/T. J. Reinhart
1   AFFDL (FB), Dr. J. C. Halpin
1   Dr. S. Tsai
1   Dr. N. Pagano

Air Force Flight Dynamics Laboratory, Wright-Patterson Air Force Base,
Ohio 45433
1   ATTN: AFFDL (FBC), C. Wallace
1   AFFDL (FBCB), G. D. Sendeckyj

National Aeronautics and Space Administration, Washington, D. C. 20546
1   ATTN: Mr. B. G. Achhammer
1   Mr. G. C. Deutsch - Code RR-1

National Aeronautics and Space Administration, Marshall Space Flight
Center, Huntsville, Alabama 35812
1   ATTN: R-P&VE-M, R. J. Schwinghamer
1   S&E-ME-MM, Mr. W. A. Wilson, Building 4720

National Aeronautics and Space Administration, Langley Research Center,
Hampton, Virginia 23365
1   ATTN: Mr. H. F. Hardrath, Mail Stop 129
1   Mr. R. Foye, Mail Stop 188A

National Aeronautics and Space Administration, Lewis Research Center,
21000 Brook Park Road, Cleveland, Ohio 44135
1   ATTN: Mr. S. S. Manson
1   Dr. J. E. Srawley, Mail Stop 105-1
1   Mr. W. F. Brown, Jr.

Panametrics, 221 Crescent Street, Waltham, Massachusetts 02154
1   ATTN: Mr. K. A. Fowler

4

Wyman-Gordon Company, Worcester, Massachusetts 01601
1 ATTN: Technical Library

Lockheed-Georgia Company, Marietta, Georgia 30063
1 ATTN: Advanced Composites Information Center, Dept. 72-34 - Zone 26

National Bureau of Standards, U. S. Department of Commerce,
Washington, D. C. 20234
1 ATTN: Mr. J. A. Bennett

1 Mr. W. F. Anderson, Atomics International, Canoga Park, California 91303

Midwest Research Institute, 425 Coker Boulevard, Kansas City, Missouri 64110
1 ATTN: Mr. C. Q. Bowles
1   Mr. J. C. Grosskreutz

1 Mr. A. Hurlich, General Dynamics Convair, Mail Zone 572-00,
   P. O. Box 1128, San Diego, California 92112

Virginia Polytechnic Institute and State University, Dept. of Engineering
Mechanics, 230 Norris Hall, Blacksburg, Virginia 24061
1 ATTN: Prof. R. M. Barker
1   Assoc. Prof. G. W. Swift

Southwest Research Institute, 8500 Culebra Road, San Antonio, Texas 78284
1 ATTN: Mr. G. C. Grimes

IIT Research Institute, Chicago, Illinois 60616
1 ATTN: Dr. I. M. Daniel

1 Dr. R. E. Johnson, Mgr., Mechanics of Materials-AEG, Mail Drop M88,
   General Electric Company, Cincinnati, Ohio 45215

1 Mr. J. G. Kaufman, Alcoa Research Laboratories, New Kensington,
   Pennsylvania 15068

1 Mr. G. M. Orner, MANLABS, 21 Erie Street, Cambridge, Massachusetts 02139

1 Mr. P. N. Randall, TRW Systems Group - 0-1/2210, One Space Park,
   Redondo Beach, California 90278

TRW Equipment, TRW Inc., 23555 Euclid Avenue, Cleveland, Ohio 44117
1 ATTN: Dr. E. A. Steigerwald, T/M-3296

1 Dr. I. S. Tuba, Basic Technology, Inc., 7125 Saltsburg Road,
   Pittsburgh, Pennsylvania 15235

1 Mr. B. M. Wundt, 2346 Shirl Lane, Schenectady, New York 12309

1   Mr. W. A. Van der Sluys, Research Center, Babcock and Wilcox, Alliance, Ohio   44601

Battelle Memorial Institute 505 King Avenue, Columbus, Ohio   43201
1   ATTN: Dr. E. Rybicki

1   Dr. K. R. Merckx, Battelle Northwest Institute, Richland, Washington   99352

General Electric Company, Schenectady, New York   12010
1   ATTN: Mr. A. J. Brothers, Materials and Processes Laboratory

General Electric Company, Knolls Atomic Power Laboratory, P. O. Box 1072, Schenectady, New York   12301
1   ATTN: Mr. F. J. Mehringer

1   Mr. L. F. Coffin, General Electric Research Laboratory, P. O. Box 1088, Schenectady, New York   12301

United States Steel Corporation, Monroeville, Pennsylvania   15146
1   ATTN: Dr. A. K. Shoemaker, Applied Research Laboratory

Westinghouse Electric Company, Pittsburgh, Pennsylvania   15235
1   ATTN: Mr. R. E. Peterson, Research Laboratories
1   Mr. E. T. Wessel, Research and Development Center

1   Mr. B. F. Langer, Westinghouse Nuclear Energy Systems, P. O. Box 355, Pittsburgh, Pennsylvania   15230

1   Mr. M. J. Manjoine, Westinghouse Research Laboratory, Churchill Boro, Pittsburgh, Pennsylvania   15235

Brown University, Providence, Rhode Island   02912
1   ATTN: Prof. J. R. Rice
1   Prof. W. N. Findley, Division of Engineering, Box D

Carnegie-Mellon University, Department of Mechanical Engineering, Schenley Park, Pittsburgh, Pennsylvania   15213
1   ATTN: Dr. J. L. Swedlow

1   Prof. J. Dvorak, Chemical Engineering Department, Duke University, Durham, North Carolina   27706

Westinghouse Electric Company, Bettis Atomic Power Laboratory, P. O. Box 109, West Mifflin, Pennsylvania   15122
1   ATTN: Mr. M. L. Parrish

George Washington University, School of Engineering and Applied Sciences, Washington, D. C.   20006
1   ATTN: Dr. H. Liebowitz

Lehigh University, Bethlehem, Pennsylvania 18015
1   ATTN: Prof. George R. Irwin
1   Prof. G. C. Sih
1   Prof. F. Erodgan

Massachusetts Institute of Technology, Cambridge, Massachusetts 02139
1   ATTN: Prof. T. H. H. Pian, Department of Aeronautics and Astronautics
1   Prof. F. J. McGarry
1   Prof. A. S. Argon, Room 1-312

1   Mr. William J. Walker, Air Force Office of Scientific Research,
    1400 Wilson Boulevard, Arlington, Virginia 22209

1   Prof. R. Greif, Dept. of Mech. Eng., Tufts University,
    Medford, Massachusetts 02155

1   Dr. D. E. Johnson, AVCO Systems Division, Wilmington, Massachusetts 01887

1   Prof. B. Pipes, Dept. of Mech. Eng., Drexel University, Philadelphia,
    Pennsylvania 19104

1   Prof. A. Tetelman, Dept. of Materials Science, University of California,
    Los Angeles, California 90024

1   Prof. W. Goldsmith, Dept. of Mech. Eng., University of California
    Berkeley, California 94700

1   Prof. A. J. McEvilly, University of Connecticut, Storrs, Connecticut 06268

1   Prof. D. Drucker, Dean of School of Engineering, University of Illinois,
    Champaign, Illinois 61820

University of Illinois, Urbana, Illinois 61820
1   ATTN: Prof. H. T. Corten, Dept. of Theoretical and Applied Mechanics,
            212 Talbot Laboratory

1   Dr. M. L. Williams, Dean of Engineering, 240 Benedum Hall,
    University of Pittsburgh, Pittsburgh, Pennsylvania 15261

1   Prof. A. Kobayashi, Dept. of Mechanical Engineering, University of
    Washington, Seattle, Washington 98105

1   Mr. W. A. Wood, Baillieu Laboratory, University of Melbourne,
    Melbourne, Australia

1   Mr. Elmer Wheeler, Airesearch Manufacturing Company, 402 S. 36th Street,
    Phoenix, Arizona 85034

No. of Copies	To

1   Mr. Charles D. Roach, U. S. Army Scientific and Technical Information Team,
    6000 Frankfurt/Main, I.G. Hochhaus, Room 750, West Germany (APO 09710, NY)

1   Prof. R. Jones, Dept. of Civil Eng., Ohio State University,
    206 W 18th Avenue, Columbus, Ohio 43210

    State University of New York at Stony Brook, Stony Brook, New York 11790
1   ATTN: Prof. Fu-Pen Chiang, Dept. of Mechanics

    E. I. Du Pont de Nemours and Company, Wilmington, Delaware 19898
1   ATTN: Dr. Carl Zweren, Industrial Fibers Div., Textile Fibers Dept.

    Washington University, St. Louis, Missouri 63130
1   ATTN: Prof. E. M. Wu

    Director, Army Materials and Mechanics Research Center,
    Watertown, Massachusetts 02172
2   ATTN: DRXMR-PL
1   DRXMR-PR
1   DRXMR-X
1   DRXMR-CT
1   DRXMR-AP

REPORT DOCUMENTATION PAGE		READ INSTRUCTIONS BEFORE COMPLETING FORM
1. REPORT NUMBER AMMRC CTR 76-41	2. GOVT ACCESSION NO.	3. RECIPIENT'S CATALOG NUMBER
4. TITLE *(and Subtitle)* Electroslag Remelting		5. TYPE OF REPORT & PERIOD COVERED Interim Report
		6. PERFORMING ORG. REPORT NUMBER
7. AUTHOR*(s)* D. R. Poirier, S. Kou, R. Furlong, and M. C. Flemings		8. CONTRACT OR GRANT NUMBER*(s)* DAAG46-74-C-0120
9. PERFORMING ORGANIZATION NAME AND ADDRESS		10. PROGRAM ELEMENT, PROJECT, TASK AREA & WORK UNIT NUMBERS D/A Project: IT062105A328 AMCMS Code: 612105.11.H8400 Agency Accession:
11. CONTROLLING OFFICE NAME AND ADDRESS Army Materials and Mechanics Research Center Watertown, Massachusetts 02172		12. REPORT DATE December 1976
		13. NUMBER OF PAGES 97
14. MONITORING AGENCY NAME & ADDRESS*(if different from Controlling Office)*		15. SECURITY CLASS. *(of this report)* Unclassified
		15a. DECLASSIFICATION/DOWNGRADING SCHEDULE

16. DISTRIBUTION STATEMENT *(of this Report)*

Approved for public release; distribution unlimited.

17. DISTRIBUTION STATEMENT *(of the abstract entered in Block 20, if different from Report)*

18. SUPPLEMENTARY NOTES

19. KEY WORDS *(Continue on reverse side if necessary and identify by block number)*

Low alloy steels	Macrosegregation
Solidification	Fluid flow
Microstructure	Heat flow
Electroslag remelting (ESR)	Refining

20. ABSTRACT *(Continue on reverse side if necessary and identify by block number)*

This interim report describes research conducted at the Massachusetts Institute of Technology on macrosegregation in ingots produced by the electroslag remelting (ESR) process. The work has been on producing small experimental ingots in the laboratory, determining the severity of segregation in those ingots, and comparing the segregation with calculations using macrosegregation theory.

Two different types of experimental apparatus are described herein. The

DD ₁ FORM JAN 73 1473   EDITION OF 1 NOV 65 IS OBSOLETE

first, employed for Al-4%Cu, is a small scale ESR unit which consists of a DC power source, a water cooled mold, consumable electrodes, and slag layer as in conventional ESR processing. The second type of apparatus is one which simulates the solidification of an ESR ingot but does not employ slag. The unit, used for Sn-15%Pb, comprises a source of melt droplets, a cooled mold, and a heat source to simulate the heat input of the ESR process.

Results of macrosegregation in a series of five Al-4%Cu experimental ingots show that severe-localized segregates, as sometimes found in large commercial ingots, cannot be produced using this alloy cast in the small-scale ESR molds (7.6 cm in diameter). Surface to center compositional variations are produced enabling a comparison with calculations using macrosegregation theory.

In order to study a wider range of segregation problems encountered in ESR ingots, recent efforts are directed toward solidifying Pb-15%Sn alloy in the simulated ESR apparatus. Initial results obtained are very encouraging. Severe macrosegregation is produced in this apparatus. In an ingot (8.2 cm diameter), the composition varies from about 26% Pb in the center to a minimum of 6%Pb slightly beyond midradius. Additionally, there are "freckles" at approximately midradius and an abnormally high fraction of eutectic constituent (similar to "V-segregates") in the center.

The analytical work is based upon an analysis of the slow creeping flow of liquid between dendrite arms. The flow is driven by (1) gravity induced convection, and (2) solidification shrinkage. Agreement between calculations of macrosegregation and the macrosegregation in the experimental ingots is excellent considering the large number of variables involved. The theory correctly predicts the presence of "freckles" found in the Sn-15%Pb ingot.